Towards nanoscale magnetic memory elements : fabrication and properties of sub - 100 nm magnetic tunnel junctions

Citation for published version (APA):
Fabrie, C. G. C. H. M. (2008). *Towards nanoscale magnetic memory elements : fabrication and properties of sub - 100 nm magnetic tunnel junctions*. [Phd Thesis 1 (Research TU/e / Graduation TU/e), Applied Physics and Science Education]. Technische Universiteit Eindhoven. https://doi.org/10.6100/IR633018

DOI:
10.6100/IR633018

Document status and date:
Published: 01/01/2008

Document Version:
Publisher’s PDF, also known as Version of Record (includes final page, issue and volume numbers)

Please check the document version of this publication:

• A submitted manuscript is the version of the article upon submission and before peer-review. There can be important differences between the submitted version and the official published version of record. People interested in the research are advised to contact the author for the final version of the publication, or visit the DOI to the publisher's website.
• The final author version and the galley proof are versions of the publication after peer review.
• The final published version features the final layout of the paper including the volume, issue and page numbers.

Link to publication

General rights
Copyright and moral rights for the publications made accessible in the public portal are retained by the authors and/or other copyright owners and it is a condition of accessing publications that users recognise and abide by the legal requirements associated with these rights.

- Users may download and print one copy of any publication from the public portal for the purpose of private study or research.
- You may not further distribute the material or use it for any profit-making activity or commercial gain
- You may freely distribute the URL identifying the publication in the public portal.

If the publication is distributed under the terms of Article 25fa of the Dutch Copyright Act, indicated by the “Taverne” license above, please follow below link for the End User Agreement:

www.tue.nl/taverne

Take down policy
If you believe that this document breaches copyright please contact us at:

openaccess@tue.nl

providing details and we will investigate your claim.

Download date: 17. Nov. 2023

Towards Nanoscale Magnetic Memory Elements

Fabrication and Properties of sub - 100 nm Magnetic Tunnel Junctions

PROEFSCHRIFT

ter verkrijging van de graad van doctor
aan de Technische Universiteit Eindhoven
op gezag van de Rector Magnificus, prof.dr.ir. C.J. van Duin,
voor een commissie aangewezen door het College
voor Promoties in het openbaar te verdedigen op
dinsdag 26 februari 2008 om 16.00 uur

door

Corine Geertruida Christina Hermienne Maria Fabrie

geboren te Eindhoven

Dit proefschrift is goedgekeurd door de promotoren:

prof.dr. B. Koopmans
en
prof.dr.ir. H.J.M. Swagten

Copromotor:
dr. E.W.J.M. van der Drift

CIP-DATA LIBRARY EINDHOVEN UNIVERSITY OF TECHNOLOGY

Fabrie, Corine Geertruida Christina Hermienne Maria

Towards Nanoscale Magnetic Memory Elements :
Fabrication and Properties of sub - 100 nm Magnetic Tunnel Junctions /
by Corine Geertruida Christina Hermienne Maria Fabrie.
- Eindhoven : Eindhoven University of Technology, 2008. -
Proefschrift Technische Universiteit Eindhoven
ISBN 978-90-386-1214-0
NUR 926

Trefwoorden: magnetische dunne lagen / magnetoweerstand / magnetische geheugens / spintronica / nanofabricage / lithografie
Index Terms: magnetic tunnel junctions / magnetoresistance / magnetic random access storage / spin-dependent transport / nanofabrication / lithography / patterning

Printed By: Universiteitsdrukkerij Technische Universiteit Eindhoven.

The work described in this thesis has been carried out in the group Physics of Nanostructures at the Eindhoven University of Technology, Department of Applied Physics. This research project was supported by NanoNed, a nanotechnology programme of the Dutch Ministry of Economic Affairs

Copyright © 2008 by Corine G.C.H.M. Fabrie.

Realism is the denial of reality

and

Imagination the means to explore reality

Corneille

Contents

1 General Introduction 1

1.1 History of Magnetic Data Storage . . . 1
1.2 Magnetic Tunnel Junctions as Memory Elements . . . 4
1.3 Outline of the Thesis . . . 9

2 Nanoscale Magnetic Tunnel Junctions 13

2.1 Spin Dependent Tunneling . . . 13
2.2 Nanoscale Magnetic Elements . . . 15
2.3 Coupling Phenomena in Nanoscale MTJs . . . 21
  2.3.1 Interlayer Coupling Mechanisms . . . 21
  2.3.2 Magnetostatic Interdot Coupling . . . 23

3 Multilayer Stack Preparation 29

3.1 Sputter Deposition of the Multilayer Stack . . . 29
  3.1.1 Sample Description . . . 31
3.2 *In situ* Characterization Techniques . . . 32
  3.2.1 Differential Ellipsometer . . . 32
  3.2.2 X-ray Photoelectron Spectroscopy . . . 34

4 Plasma Oxidation of Sub-nm Al_2O_3 Barriers 37

4.1 Ellipsometry Measurements . . . 37
4.2 XPS Measurements . . . 40
4.3 Discussion and Conclusion . . . 42

5 Nanofabrication of Magnetic Tunnel Junctions 45

5.1 Outline of the Fabrication Process . . . 45
5.2 High-Speed Electron Beam Lithography . . . 48
5.3 Mask Fabrication . . . 50
  5.3.1 Ta Etching in a Low Temperature SF_6/O_2 Plasma . . . 50
  5.3.2 PMMA Etching in an O_2 Reactive Ion Plasma . . . 53
5.4 Pattern Transfer Techniques . . . 54
  5.4.1 Ar^+ Ion Milling . . . 54
  5.4.2 Inductively Coupled Cl_2-based Plasma . . . 56
  5.4.3 Noncorrosive CO/NH_3 Plasma . . . 57

6 Magnetic Properties of Nanometer Scale Elements 59

6.1 Magnetic Characterization Techniques . . . 59
  6.1.1 SQUID Magnetometer . . . 60
  6.1.2 MOKE Magnetometer . . . 61

6.2 Sample Description and Experimental Procedure . . . 62
    6.2.1 Composition and Layout of the Samples . . . 62
    6.2.2 Application of Magnetometry Measurements . . . 64
6.3 Magnetization Reversal of Arrays of Co Dots . . . 67
    6.3.1 Overview of the SQUID Measurements . . . 67
    6.3.2 Shape of the Hysteresis Loops . . . 68
    6.3.3 Contributions to the Magnetization Reversal Process . . . 71
    6.3.4 Geometry Effect on the Switching Behavior . . . 74
6.4 Free Layer Switching of Sub-μm MTJs . . . 75
6.5 Conclusion . . . 79

7 Magnetization Losses in Sub-μm CoFeB Dots 81
7.1 Dry Etching of CoFeB Dots . . . 81
7.2 Faceting of the Mask . . . 84
7.3 Corrosion by Chlorinated Etch Residues . . . 86
7.4 Conclusion . . . 86

8 Electrical Characterization of Sub-μm MTJs 89
8.1 I-V Characteristics of Ultra Thin AlO_x Barriers . . . 89
8.2 Scanning Force Microscopy . . . 92
    8.2.1 Conductive Atomic Force Microscopy . . . 94
8.3 Conclusions and Outlook . . . 96

References 98

Summary 107

Samenvatting 111

Nomenclature 115

List of Publications & Presentations 119

Dankwoord 121

Curriculum Vitae 123

List of Figures

1.1 Photograph of a magnetic core memory plane 2
1.2 Illustration of the TMR effect in MTJs 3
1.3 Photograph of Freescale's MR2A16A 4 Mbit MRAM device 4
1.4 Schematic of the Jullière model to explain the TMR effect 5
1.5 TMR measurement at 300 K of a Co/Al_2O_3/CoFe MTJ 6
1.6 Write operation of an MTJ in a cross-point MRAM architecture 7
1.7 Energy profiles for different applied magnetic fields 7
1.8 Evolution of magnetically engineered MTJs for MRAM application 8

2.1 Schematic illustration of MIM tunneling 15
2.2 Ferromagnetic body of length l, width w and thickness d, with $l > w \gg d$. 16
2.3 Graphs of the demagnetizing factors of the general ellipsoid 17
2.4 Magnetization reversal modes for a prolate spheroid 18
2.5 Parameter ξ of equation as function of the aspect ratio b : a 19
2.6 Magnetization reversal in Buckling mode 20
2.7 Schematic of the Néel coupling 22
2.8 Representation of a $n \times n$ array of elliptical dots 23
2.9 Interdot field as a function of array size 24
2.10 Magnetization configuration of a 3×3 array of elliptical shapes 25
2.11 OOMMF hysteresis loops of $n \times n$ arrays of ellipses 26

3.1 Photograph of the *EUFORAC* 30
3.2 Principle of the sputter deposition 31
3.3 Schematic of the *in situ* differential ellipsometer 33
3.4 Reflections and transmissions in an Al_2O_3 - Al sample 33
3.5 Illustration of the XPS principle 35

4.1 Ellipsometry measurements of the plasma oxidation 38
4.2 Oxidation rate as function of the oxidation time 38
4.3 Onset of the CoFe oxidation 39
4.4 O-1s and Al-2p XPS spectra 40
4.5 Co-$2p_{3/2}$ XPS spectra 41
4.6 Percentage oxidized Al 42
4.7 Comparison of the amount of CoO 43

5.1 Fabrication of the magnetometry samples 46
5.2 Fabrication of the c-AFM samples 47
5.3 Schematic of the Leica (Vistec) 5000^+ EBPG machine 48
5.4 Illustration of EB writing methods 49

5.5 Illustration of the ICP etching system 51
5.6 Arrhenius plot of the Ta etch rate 52
5.7 Ta etch depth as function of the time 53
5.8 Schematic of the RIE system 53
5.9 Ar^+ ion beam milling machine 55
5.10 Ar^+ ion mill rate dependency on beam incidence angle 55
5.11 Resulting magnetometry sample with dense array of 50×65 nm^2 MTJs . . 56
5.12 Etch depth as function of time in a $\mathrm{CO/NH_3}$ plasma 58

6.1 Schematic of the SQUID 60
6.2 Home-built MOKE magnetometer 61
6.3 Composition and layout of the samples 63
6.4 SEM images of rectangular and elliptical MTJs 63
6.5 SQUID measurement of an unstructured MTJ sample 64
6.6 SQUID measurements to determine milling depth 65
6.7 MOKE measurements for nanoscale MTJ characterization 66
6.8 Overview of the SQUID measurements 67
6.9 Hysteresis loops of arrays of 50×65 nm^2 Co dots 68
6.10 Hysteresis loops of arrays of 120×160 nm^2 and 160×320 nm^2 Co dots . . . 69
6.11 Schematic of the magnetization reversal 70
6.12 Stoner-Wohlfarth switching fields in comparison with experimental data . . 71
6.13 Major and minor axis hysteresis loops 73
6.14 Investigation of the geometry effect on the switching behavior 74
6.15 Coercive field of rectangular MTJs 76
6.16 Coercive field of elliptical MTJs 76
6.17 Coercive field as function of the aspect ratio 77
6.18 Measured and calculated loop shifts 78

7.1 Hysteresis loops of unetched and etched samples 82
7.2 SEM pictures of CoFeB dots 83
7.3 Schematic drawing of a CoFeB dot 84
7.4 Magnetization as a function of the width of the dots 85

8.1 Process flow of 4-point electrical samples 90
8.2 Different type of I-V characteristics 91
8.3 I-V characteristics of a 1 μm^2 MTJs 92
8.4 Schematic of the setup for SFM 93
8.5 Tip-sample interaction potential diagram 94
8.6 Home-built c-AFM upgrade application module 94
8.7 Image and zoom-in image of a 3-point nanoscale MTJ 96

Chapter 1

General Introduction

The topic of this Thesis is the fabrication and properties of nanoscale magnetic tunnel junctions (MTJs). MTJs can be used as bits for digital information storage and serve as the basic elements for magnetic random access memories (MRAMs). MRAMs have the advantage that information remains on the memory elements even without a power supply and that data are faster accessible. To replace the current RAM technologies by MRAMs, the dimensions of the bits for data storage has to decrease to sub-100 nm in order to achieve a sufficiently high areal density [1]. Ever since the introduction of magnetic data storage, the number of magnetic bits per unit area, the areal density, is continuously increasing.

The aim of this general introduction is to give a historical overview of magnetic data storage, and to explain how MTJs can be used as memory elements for data storage on MRAMs. Furthermore, the relevance of scaling down MTJs to sub-100 nm lateral dimensions will be discussed. Finally, the addressed issues and the work described in this Thesis will be outlined.

1.1 History of Magnetic Data Storage

Magnets have been known to mankind for ages. The notion that magnets can be used for data storage is a relatively new discovery and was put into practice well over a century ago. The first practical apparatus for storing magnetic information was the telegraphone, which was demonstrated by Poulsen in 1898. The telegraphone recorded varying magnetic fields produced by sound on a steel wire, which in turn could be used to play back the sound [2]. Poulsen's invention served as the foundation for the discovery of magnetic tape, in 1928 by Pfleumer. It took four years for AEG and BASF to commercialize this idea and launch the magnetophon. The technology evolved slowly during the first part of the twentieth century and was mainly used in dictaphones, for telephone message recording and for delayed radio broadcasting. Over two decades passed before magnet tapes were used to store digital information instead of sound. In 1951 the first recording medium for data storage on a nickel plated bronze tape was available. IBM computers developed this technology further and used iron oxide coated tape, similar to that used in audio recording.

In 1932 Taushek was inspired by the discovery of Pfleumer and coated the outside surface of a metal drum with a thin ferromagnetic recording layer. A row of recording heads were mounted at a distance of a few micrometers from the drum. Binary values of

'0' or '1' were recorded by generating electric pulses while the drum rotated. The magnetic drum memory was an early high-speed, direct access storage device that was widely used as a computer memory in the 1950s and 1960s. With media such as paper tapes or punch cards the data and programs were loaded on to the drum, which formed the main working memory of a computer.

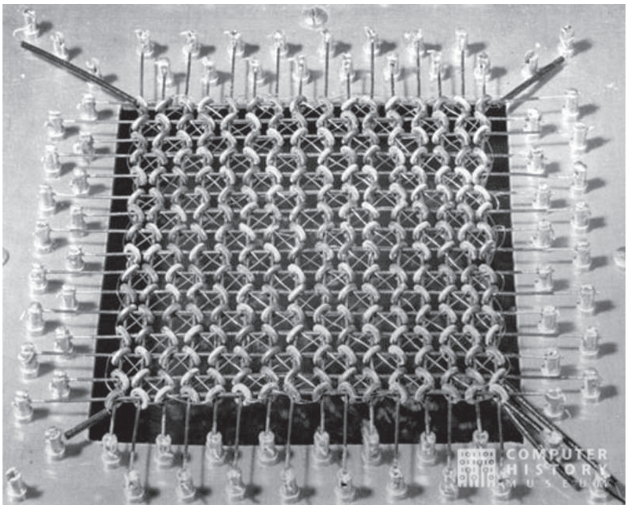

Figure 1.1: Photograph of a magnetic core memory plane [3].

In 1949 Wang started the earliest work on core memories [4], which were faster than drum memories and had no moving parts. The drum memories were replaced by core memories in the 1960s. This technology makes use of a 3-dimensional array of tiny ferromagnetic cores to store information via the polarity of the magnetic field the cores contain. The cores are magnetized by a magnetic field, generated by a current flowing in wires through the core. A core is needed for each bit of memory and is magnetized in either a clockwise or counterclockwise direction, representing a '0' or a '1', respectively. Providing the means to select and detect the contents of each bit, three wires are threaded through a core, as can be seen in figure 1.1.

By the early 1970s, core memories were history and semiconductor memories entered the scene. As of then the actual computing took place in the semiconductor memory, known as random access memory (RAM). Besides that, computers also used a magnetic hard disk as a static memory for non-volatile massive data storage. On hard disks information was stored by magnetizing regions within a thin magnetic film. The magnetic stray field from each bit region was measured with a recording head, which was floating on an air bearing above the recording hard disk at a height of a few nanometers [5]. The ever increasing areal density on magnetic hard disk storage devices also required the technological development of the recording heads.

Initially, yoke-type heads that utilized magnetic induction to read and write magnetic bits were used. The first successful application to replace the induction yoke-type heads was proposed in 1971 by Hunt. Hunt's recording head is based on the anisotropic magnetoresistance (AMR) effect in a thin magnetic film [6]. The AMR effect is in principle a bulk scattering effect found in ferromagnets and depends on the orientation of the magnetization with respect to direction of the current in the material [7]. The AMR effect is approximately 6 % at room temperature for ferromagnetic $3d$ alloys. However, for thin films this percentage decreases with decreasing film thickness, due to the scattering from the interfaces [8].

In 1988 the giant magnetoresistance (GMR) effect was discovered independently in epitaxial (001) oriented Fe/Cr superlattices [9] and Fe/Cr/Fe sandwiches [10]. The origin of the GMR effect is a result of spin scattering in alternating magnetic and non-magnetic metallic multilayers, dependent on the relative magnetization in the magnetic layers. Although at first the measured GMR effects in epitaxial Fe/Cr layers at room temperature were modest ($\approx$ 13 %), within three years after the discovery GMR effects values of more than 65 % were found in sputter deposited Co/Cu multilayers [11]. The GMR research area developed very fast and in 1997 already, IBM introduced a GMR recording head commercially.

The areal density of magnetic hard disks continued to increase to such an extent that alternatives to GMR recording heads could be requested. In magnetic tunnel junctions (MTJs) much larger effects were found at room temperature. An MTJ consists of two magnetic layers separated by a thin insulating barrier instead of a metallic spacer layer. The current that flows through the barrier depends on the relative alignment of the magnetization in the magnetic layers, which is known as the tunnel magnetoresistance (TMR) effect. The resistance is low when the magnetization is parallel and high in an anti-parallel configuration, as can be seen in figure 1.2.

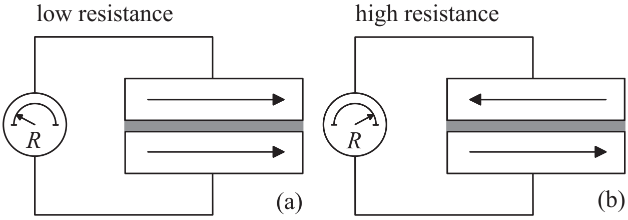

Figure 1.2: Illustration of the tunnel magnetoresistance (TMR) effect in magnetic tunnel junctions (MTJs). The resistance is low when the magnetization is parallel (a) and high if the magnetization is anti-parallel (b).

MTJs are particularly attractive for ultra high density magnetic recording, because of the perpendicular current flow through the TMR device. The high TMR signal from a single MTJ allows for the utilization of MTJs for a cross-point magnetic random access memories (MRAMs) architecture [12]. Furthermore, the perpendicularly flowing current through the MTJ memory element and the adjustable resistance, facilitates the integration with complementary metal-oxide-semiconductor (CMOS) circuits. In 2006 the first commercial 4 Mbit MRAM device, the MR2A16A, was taken into volume production by Freescale semiconductor. A photograph of the MR2A16A is shown in figure 1.3. In the next section, we will elaborate on the functioning of MTJs as memory elements for MRAMs.

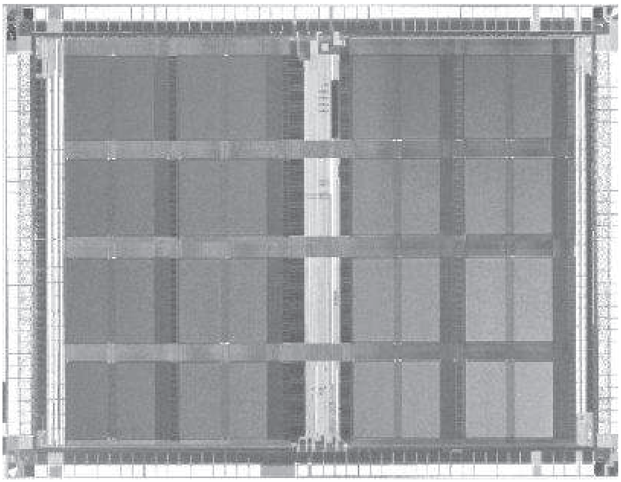

Figure 1.3: Photograph of Freescale's MR2A16A, which was the first commercial 4 Mbit MRAM device that was taken into production [13].

1.2 Magnetic Tunnel Junctions as Memory Elements

A magnetic tunnel junction (MTJ) is a spintronic device that is based on quantum mechanical tunneling of spin-polarized electrons through a thin insulating barrier. In 1960, Giaever established electron tunneling between Al and superconducting Pb electrodes through an Al_2O_3 barrier [14]. The tunnel conductance curve resembled the Bardeen-Cooper-Schrieffer quasi-particle density of states (DOS). This is originating from the dependency of the tunnel probability on the product of the DOS at the Fermi level in both electrodes [15].

At the Fermi level the $3d$-band of ferromagnetic metals is split in a spin-up ↑ and a spin-down ↓ band with different DOS. If the spin is conserved in the tunneling process, an electron can only be transferred between bands with equal spin. Tedrow and Meservey utilized the spin-polarized tunneling technique to demonstrate spin-dependent tunneling from superconducting Al through Al_2O_3 into Ni. Spin-dependent tunneling depends on the degree of the spin polarization in the magnetic electrode. This polarization is defined as [16]:

$$P = \frac{N_{\text{maj}} - N_{\text{min}}}{N_{\text{maj}} + N_{\text{min}}} \quad , \tag{1.1}$$

where N_{maj} and N_{min} are the number of majority and minority spin states at the Fermi level.

In 1975, Jullière performed the first pioneering experiments on a $Fe/GeO_x/Co$ magnetic tunnel junction (MTJ). The tunnel current between the Fe and Co layers was dependent on the relative orientation of the magnetization of the two electrodes. At 4.2 K, a difference in resistance of 14 % was observed between the parallel and anti-parallel state of the magnetization [17]. The analysis of Tedrow and Meservey inspired Jullière to explain this phenomenon with a simple model based upon spin-dependent tunneling.

This model is schematically presented in figure 1.4 to explain the tunnel magnetoresistance effect (TMR), where a voltage V is applied across a barrier that is separating two magnetic electrodes FM1 and FM2. Figure 1.4(a) depicts the situation with a parallel magnetization of the electrodes. In the parallel state, the tunneling current of spin-up electrons $I_{\mathrm{P},\uparrow}$ is proportional to the available majority spin states $N_{\mathrm{maj},1}$ in electrode FM1 and the free majority spin states $N_{\mathrm{maj},2}$ in electrode FM2. Whereas the spin-down current $I_{\mathrm{P},\downarrow}$ is proportional to the available minority spin states $N_{\mathrm{min},1}$ and the free minority spin states $N_{\mathrm{min},2}$. In the anti-parallel state of magnetization the spin-up current $I_{\mathrm{AP},\uparrow}$ and the spin-down electron current $I_{\mathrm{AP},\downarrow}$ have equivalent proportionalities, which are shown in figure 1.4(b).

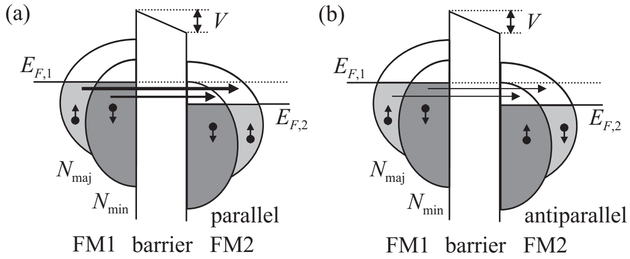

Figure 1.4: Schematic presentation of Jullière model to explain the tunnel magnetoresistance (TMR) effect. In case the electrodes FM1 and FM2 have a parallel magnetization, the resistance is low and $I_P \propto N_{maj,1}N_{maj,2} + N_{min,1}N_{min,2}$ *(a). In the anti-parallel state of magnetization the resistance is high and* $I_{AP} \propto N_{maj,1}N_{min,2} + N_{min,1}N_{maj,2}$ *(b).*

Assuming the spin is conserved during the tunnel process for both magnetization states, the total tunnel current is the sum of the independent spin-up and spin-down current contributions, $I = I_{\uparrow} + I_{\downarrow}$. The TMR effect is defined as the difference in resistance ($\Delta R = R_{\mathrm{AP}} - R_{\mathrm{P}}$), normalized by the resistance in the anti-parallel magnetization state. Using equation 1.1 for the spin polarizations P_1 and P_2 of the magnetic electrodes FM1 and FM2, respectively, Jullière expressed the TMR as:

$$\mathrm{TMR} \equiv \frac{\Delta R}{R_{\mathrm{AP}}} = \frac{I_{\mathrm{P}} - I_{\mathrm{AP}}}{I_{\mathrm{P}}} = \frac{2P_1P_2}{1+P_1P_2} \quad . \tag{1.2}$$

The research field of spin-dependent tunneling in MTJs developed slowly and measurable TMR values were only observed at low temperatures. However, the breakthrough was achieved in 1995, when Miyazaki and Tezuka obtained an 18 % effect at room temperature in a Fe/$\mathrm{Al_2O_3}$/Fe MTJ, which was defined as the ratio of the resistance change from the anti-parallel to parallel magnetization and the resistance at saturated magnetization [18]. Moodera *et al.* independently produced Co/$\mathrm{Al_2O_3}$/CoFe MTJs with a TMR effect over 10 % at room temperature, according to the definition in equation 1.2 [19].

Figure 1.5 shows a TMR measurement of a Co/$\mathrm{Al_2O_3}$/CoFe MTJ performed at 300 K [20]. The resistance change is plotted as a function of the applied magnetic field in the plane of the film. At high fields, the magnetization in both layers is parallel. Upon reversing the field the resistance starts to change sharply. This marks the switching of the magnetization of the free Co layer, which has a lower coercive field than the CoFe layer. At about ± 8.5 kA/m the resistance change drops distinctly, indicating that the magnetization of the CoFe layer is reversing. The change in resistance between parallel and anti-parallel alignment of the Co/Al_2O_3/CoFe MTJ yields a TMR effect of almost 20 %.

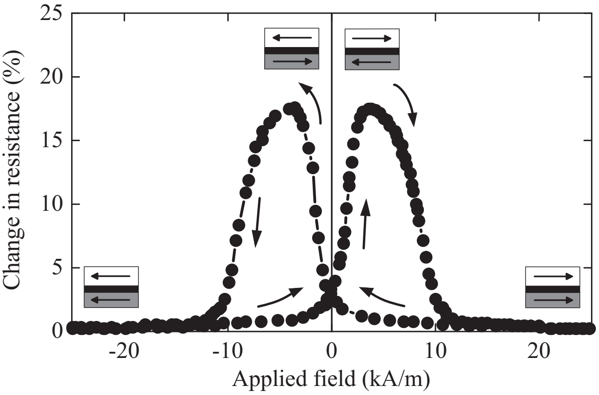

Figure 1.5: A typical TMR measurement of a Co/Al_2O_3/CoFe MTJ performed at 300 K [20].

The breakthrough of the high TMR effect values cleared the way for MTJs to be used as bits for information storage and serve as the basic cells for magnetic random access memories (MRAMs). A schematic illustration of an MRAMs architecture is shown in figure 1.6(a). Consider an array of nanoscale MTJs at the cross-points of orthogonal conductors placed below (word lines) and above (bit lines) each MTJ. To prevent sneak current paths in the matrix arrangement, each MTJ is connected with an isolation transistor in the underlying CMOS circuits [21], as is shown in figure 1.6(b).

To read-out the magnetization state of an MTJ, the isolation transistor is grounded while the bit line along the MTJ is forward biased. The tunnel current that flows through the barrier depends on the relative alignment of the magnetization in the magnetic layers. As indicated before, the resistance is low when the magnetization is parallel and high if the magnetization is antiparallel, generating a logical '0' or '1' as output, respectively.

The write operation of an MTJ is done by switching off the transistor and sending a current through the intersecting word and bit lines. All MTJs on the word and bit line are half-selected, except the selected MTJ on the cross-point of the intersecting lines, as is indicated in figure 1.6(c). The magnetic field $\vec{H}_{\mathrm{hard}}$ resulting from the word line current is too small to switch the free layer of the MTJs along the word line. Also the field $\vec{H}_{\mathrm{easy}}$ produced by the bit line current is too small for switching the free layer of the MTJs along the bit line.

In order to switch the free layer, the applied magnetic field $\vec{H}_{\mathrm{appl}}$ has to overcome an energy barrier E_{b} resulting from a magnetic shape anisotropy. Figure 1.7 shows a sequence of energy profiles for different applied magnetic fields. At zero magnetic field the energy profile has two minima corresponding to the magnetization pointing in the up or down direction along the easy-axis, as can be seen in figure 1.7(a). For small fields around zero one direction is stable and one is metastable. Applying a magnetic field along either

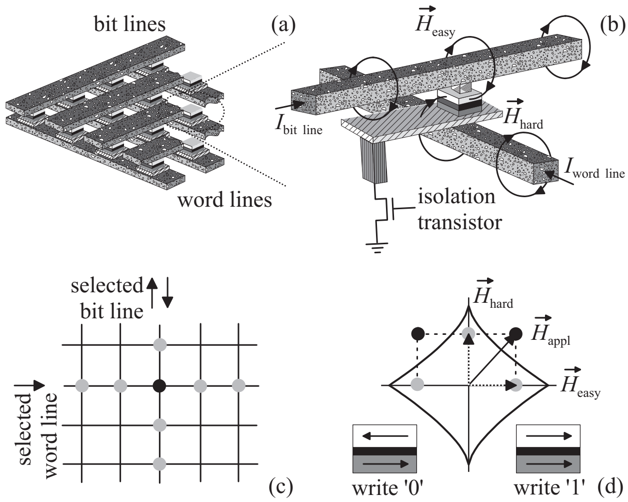
bit lines
(a)
word lines
$\vec{H}_{\text{easy}}$
(b)
$I_{\text{bit line}}$
$\vec{H}_{\text{hard}}$
$I_{\text{word line}}$
isolation
transistor
selected
bit line
selected
word line
(c)
$\vec{H}_{\text{hard}}$
$\vec{H}_{\text{appl}}$
$\vec{H}_{\text{easy}}$
write '0'
write '1'
(d)

Figure 1.6: An illustration of a cross-point magnetic random access memories (MRAMs) architecture (a). Zoom in on a single cross-point of the MRAM with an MTJ in write mode [21] (b). A schematic of an MTJ array with the selected (black) and half-selected (gray) MTJs (c). The threshold Stoner-Wohlfarth astroid curve to indicate the switching boundary [22] (d).

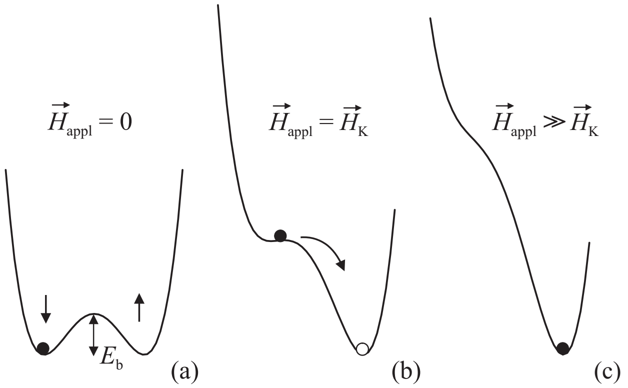
$\vec{H}_{\text{appl}} = 0$
E_{b}
(a)
$\vec{H}_{\text{appl}} = \vec{H}_{\text{K}}$
(b)
$\vec{H}_{\text{appl}} \gg \vec{H}_{\text{K}}$
(c)

Figure 1.7: Energy profiles in zero magnetic field (a), for $\vec{H}_{appl} = \vec{H}_{K}$ (b), and $\vec{H}_{appl} \gg \vec{H}_{K}$ (c). The horizontal axes correspond to the direction cosines of the magnetization.

the hard-axis or easy-axis reduces the energy barrier. The barrier reduces to zero, if the applied field is equal to the anisotropy field $\vec{H}_{\text{K}}$ and the free layer can be switched, as is indicated in figure 1.7(b). There is only one stable direction available if the applied field is very large, namely when the magnetization is aligned with the applied field. Figure 1.7(c) shows this condition that is evolved from the merging and disappearing of one minimum and one maximum of figure 1.7(a). Therefore, a closed curve around the origin must exist that separates the two-energy-minima low-field region from the one-energy-minimum high-field region [23].

For an elliptical particle, this switching boundary curve is illustrated in figure 1.6(d), and is known as the threshold Stoner-Wohlfarth astroid curve for orthogonal word and bit lines [22]:

$$H_{\mathrm{K}}^{2/3} = H_{\mathrm{hard}}^{2/3} + H_{\mathrm{easy}}^{2/3} \quad . \tag{1.3}$$

When the sum of the two magnetic fields $\vec{H}_{\mathrm{appl}}$ points outside the Stoner-Wohlfarth astroid curve, the field is high enough to switch the magnetization of the free layer, and the MTJ on the intersection of the word and bit lines will be written in a definite state.

As mentioned before, an MTJ must exhibit two different resistance values to distinguish a logical '0' and a logical '1', corresponding to anti-parallel and parallel magnetization at small magnetic fields. For an useful application of MTJs as memory elements, the MTJ is incorporated in an engineered multilayer stack to promote stability and reproducibility of the magnetic and electric response of the MTJ. In the following, we describe the evolution of the engineered MTJ multilayer stack.

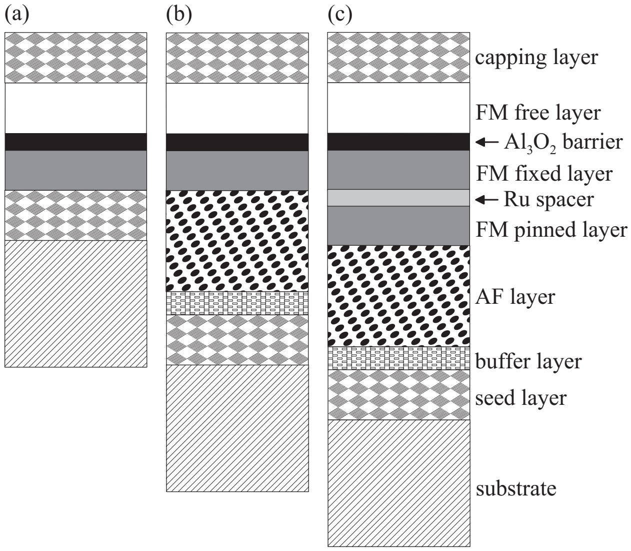

Figure 1.8: Evolution of the magnetically engineered MTJs for MRAM application.

A stable anti-parallel and parallel magnetic state in the interests of a significant TMR effect, can be realized by exploiting two ferromagnets with different coercive fields. The magnitude of the TMR effect is extremely sensitive to the interfaces' roughness. Therefore, the quality of an MTJ is mainly determined by the interface smoothness. To promote reasonably smooth layer growth, first a thin seed layer is grown on the SiO_2 substrate. Generally, refractory metals such as Ta, Ru, and W are used as buffer layer because of their relatively smooth growth on SiO_2 [24]. Furthermore, a capping layer is used to protect the MTJ stack from oxidation. The resulting basic MTJ-MRAM stack is depicted in 1.8(a).

The write operation of an MTJ involves an independent switch of the two magnetic layers. However, repeated switching of the free layer by magnetic field sweeping can demagnetize the other layer due to roughness-induced magnetostatic coupling, known as Néel coupling. To prevent this stability decay, one of the ferromagnetic (FM) layers can be pinned to an adjacent layer of antiferromagnetic (AF) material such as FeMn, IrMn or PtMn, through an exchange bias interaction [25]. Generally, the AF layer is grown on a magnetic buffer layer, as can be seen in figure 1.8(b).

In order to achieve a sufficiently high areal density, the dimensions of the MTJ-MRAM cell have to decrease to sub - 100 nm. For sub - 100 nm MTJs, the independent switching of the free- and pinned layer is obstructed by stray field coupling in addition to the Néel coupling. The stray field fringing from the pinned layer can be eliminated by employing an artificial antiferromagnet (AAF). An AAF comprises a sandwich of two identical FM layers separated by a 7 to 8 Å thick Ru spacer layer. The moments of the two FM layers are antiferromagnetically coupled in opposite directions through the Ru spacer and due to the flux closure the coupling to the free layer is reduced [26]. To enhance the magnetic stability, the lower FM layer is also pinned via exchange bias to an AF. The configuration of the magnetically engineered MTJ multilayer stack for MRAM application that we have studied in this Thesis is depicted in figure 1.8(c). However, nowadays more complex toggle MTJ multilayer stacks are used in industry that consist of two AAFs, which are separated by the insulating barrier [27].

1.3 Outline of the Thesis

The work in this Thesis focuses on the scaling properties of magnetic devices based on MTJs for future spintronics devices, such as magnetic random access memories (MRAMs). Scaling down to sub - 100 nm lateral dimensions is required to achieve a sufficiently high areal density and to match the semiconductor technology. Accordingly, a considerable part of the Thesis is devoted to the nanofabrication of sub - 100 nm MTJs.

Regarding the nanofabrication, we have concentrated on the oxidation of sub - nm thin Al layers to produce Al_2O_3 barriers, because for MTJs with a surface area of less than 0.01 μm^2, the Al_2O_3 barrier has an approximate thickness of a nanometer to ensure an appropriate tunnel current.

In addition, we have developed a fabrication technology including electron beam (EB) lithography for patterning, while Ar^+ ion beam milling, reactive ion etching and inductively coupled high ion density etching are all used for the structuring the magnetically engineered MTJ multilayer stacks. From a commercial perspective EB lithography is not the most obvious choice for patterning large-area samples with ultra-dense arrays of sub - 100 nm MTJs. Nevertheless, EB lithography yields great opportunities for science to create features of only a few nanometer in size, hence enables the exploration of the fundamental boundaries of magnetic and electric scaling properties. Therefore, the research within this Thesis also aims at investigating the influence of the reduced dimensions of an MRAM-like structure on the modification of magnetic and electronic properties.

In order to address the mentioned issues, the consequences of the reduced dimensions on spin dependent tunneling and the switching behavior of nanoscale MTJs will be discussed in chapter 2. Besides that, particular attention is given to the influence of the interdot coupling on the switching behavior.

The preparation of the multilayer stacks for the top-down nanostructuring of MTJs is discussed in chapter 3. These multilayer stacks are prepared using the Eindhoven University nano-Film depOsition Research and Analysis Center (EUFORAC). Additionally, the differential ellipsometer and the X-ray photoelectron spectroscopy (XPS) apparatus for the *in situ* characterization of samples will be discussed.

In chapter 4 we present *in situ* differential ellipsometry and X-ray photoelectron spectroscopy (XPS) measurements to study the plasma oxidation of an Al layer to create the Al_2O_3 tunnel barrier. For nanometer thin Al_2O_3 barriers, excellent control over the oxidation of sub - nm thin Al layers is of utmost importance. The ellipsometry and XPS characterization techniques are used to monitor the conversion from Al to Al_2O_3 and to determine the onset of the over-oxidation of sub - nanometer thin barriers for magnetic tunnel junctions. By analyzing the oxidation rate in real-time, we are able to mark the moment at which the over-oxidation of the Al_2O_3 barrier starts with great precision.

Chapter 5 describes the principle of electron beam lithography, which is used to define the pattern of the nanoscale MTJs in a resist layer. We present a special high-speed EB writing strategy that we developed to pattern a sample area of 16 mm^2 with ultra-dense arrays of sub - 100 nm elliptical features in 10 minutes. Large-area samples with ultra-dense arrays of sub - 100 nm elliptical features can be written about 16 times faster using the high-speed EB writing strategy.

Furthermore, we report about etching Ta in a low temperature inductively coupled high density SF_6/O_2 plasma and polymethylmethacrylate (PMMA) etching in an O_2 reactive ion plasma, to define the masks for the samples to characterize the magnetic and electrical properties, respectively. Additionally, we discuss several pattern transfer techniques that we used to structure the magnetic and electrical samples.

Magnetometry measurements are used to investigate, the magnetic switching behavior for arrays of nanoscale Co dots and arrays of sub - μm MTJ without electrical contacts. Deviations of the Stoner-Wohlfarth behavior are observed and will be discussed in term of interdot coupling and edge roughness in chapter 6. We suggest that the interdot coupling facilitates the magnetization reversal and thereby influences the switching field. By comparing the experimental data with the outcome of micromagnetic simulations of the switching of a single dot, we unambiguously demonstrate that the interdot coupling has a major influence and account for the early switching of part of the elements of the array.

Faceting of the etch masks and chlorinated etch residues can reduce the magnetization of patterning magnetic materials substantially, and therefore constitutes a considerable concern. We have studied the relation between process induced damage and the magnetic properties of sub-μm CoFeB dots that are etched in a high ion density Cl_2-based plasma. The investigations on the reduced magnetization of patterned CoFeB dots are presented in chapter 7. Magnetometry measurements and scanning electron microscopy (SEM) studies were performed to distinguish between the reduction of the magnetization due to faceting of the etch masks and due to chlorinated etch residues on the sidewalls of the etched features.

In chapter 8 the I-V characteristics of sub - μm MTJs with a nanometer thin AlO_x barrier are specified. The I-V characteristics are measured by applying a voltage over a 1×1 μm^2 square MTJ pillar located at the cross-point of the bottom and top electrode. Three different characteristics of the I-V response are observed. Namely, an ohmic like response, a response resembling breakdown, and a tunneling response. The measured MTJs that showed a tunneling response had a resistance-area product between approximately 20 and 50 k$\Omega\mu m^2$. Furthermore, the conductance showed roughly a parabolic behavior implying an asymmetrical barrier. The Brinkman formula is used to fit the experimental data, the fits yielded average barrier heights between 1.2 and 2.3 eV, and an asymmetry parameter ranging from 0.3 to 0.8 eV, which are close to reported observations in literature. Due to a strong Néel coupling, the resistance measurements yielded no significant magnetoresistance for the 1 μm^2 MTJs, because of the stability decay of the magnetization.

As an alternative, the scanning force microscopy (SFM) technique that is used in the conductive mode is discussed in chapter 8. This technique is explored to measure the electrical properties of the nanoscale MTJs. However, no significant bias voltage dependency was observed, due to resist remains.

Chapter 2

Nanoscale Magnetic Tunnel Junctions

Nanoscale magnetic tunnel junctions (MTJs) can be used as bits for information storage. As stated before, MTJs consist of two ferromagnetic electrodes, which are separated by a thin insulating barrier, usually Al_2O_3. The dimensions of the bits for information storage have to decrease to sub - 100 nm in order to achieve a sufficiently high areal density to match the semiconductor technology. In this chapter, the consequences of reduced dimensions on the properties of nanoscale MTJs will be discussed, and some numerical simulations will be presented. First, the basic concepts of spin dependent electron tunneling will be explained. After that, the effect on the magnetic switching behavior of the reduced MTJ will be described. Finally, we will discuss the interlayer and interdot coupling.

2.1 Spin Dependent Tunneling

Electron tunneling is a quantum mechanical process in which electrons have a finite probability P_{12} to flow from electrode 1 into electrode 2, through an insulating barrier. Figure 2.1 schematically illustrates tunneling in metal-insulator-metal structures. An incoming electron wave function $\Psi(x)$ is partially reflected and partially transmitted into the barrier with thickness d. When electrode 2 is positively biased with a voltage V, a net current will flow through the barrier due to the energy difference eV. In the barrier of height ϕ_0 above the Fermi level of electrode 1 $E_{F,1}$, the wave function decays exponentially.

According to Bardeen, the probability per unit time of an electron in a state with wave vector $\vec{k}$ and energy E to tunnel through the barrier depends on the product of density of states (DOS) in both electrodes $\rho_1(E)$ and $\rho_2(E+eV)$, respectively, multiplied by the square of the matrix element $|M_{12}|^2$ for the transition. Besides that, the probability is proportional to the available states corresponding to the Fermi-Dirac distribution function $f_1(E)$ in electrode 1 and the free states $1 - f_2(E+eV)$ in electrode 2 [15]. The tunnel current J_{12} from electrode 1 to 2, is obtained by the summation over all states for a fixed transverse wave number k_t, sum over k_t, multiplied by the electronic charge e and by 2 to account for the spin-up $\uparrow$ and spin-down $\downarrow$. Subtracting the tunnel current J_{21} gives the total tunnel current density [28]:

$$J(V) = \frac{4\pi e}{\hbar} \sum_{k_t} \int_{-\infty}^{\infty} |M_{12}|^2 \rho_1(E) \rho_2(E + eV)[f_1(E) - f_2(E + eV)]\mathrm{d}E \quad . \tag{2.1}$$

Suppose that the potential energy in the barrier is slowly varying compared to the electron wave function $\Psi(x)$. Then the Wentzel, Kramers, Brillouin (WKB) approximation can be applied to obtain solutions to the time independent Schrödinger equation in one dimension [29]. The WKB approximation was used by Simmons to acquire the matrix elements $|M_{12}|^2$ for a rectangular barrier with an average height $\overline{\phi} = \frac{1}{d}\int_0^d [V(x) - E_F]dx$ above the Fermi level. Simmons inserted the result in equation 2.1 to develop a simplified model to fit experimental current-voltage characteristics [30]:

$$\begin{aligned} J(V) \quad &= \quad \frac{e}{4d^2\pi^2\hbar}\left(\overline{\phi} - \frac{eV}{2}\right)\exp\left[-\frac{2d}{\hbar}\sqrt{2m\left(\overline{\phi} - \frac{eV}{2}\right)}\right] \\ &- \quad \frac{e}{4d^2\pi^2\hbar}\left(\overline{\phi} + \frac{eV}{2}\right)\exp\left[-\frac{2d}{\hbar}\sqrt{2m\left(\overline{\phi} + \frac{eV}{2}\right)}\right] \quad , \end{aligned} \tag{2.2}$$

where m is the electron mass. In the Simmons model all information about barrier asymmetry is lost. In order to calculate the current-voltage characteristics for two different electrodes, Brinkman introduced an asymmetry parameter $\Delta\phi = \phi_2 - \phi_1$ to account for a trapezoidal barrier shape, where ϕ_1 and ϕ_2 are the barrier heights on either side of the barier with zero applied voltage. The Brinkman formula is derived by a Taylor expansion of the tunnel current density expression in the voltage to the third power [31]:

$$J(V) = \frac{e^2\sqrt{2m\overline{\phi}}}{4d\pi^2\hbar^2}\exp\left(-\frac{2d}{\hbar}\sqrt{2m\overline{\phi}}\right)\left[V + \frac{de\sqrt{2m}\Delta\phi}{24\hbar\overline{\phi}^{\;2/3}}V^2 + \frac{de^2m}{12\hbar\overline{\phi}}V^3\right] \quad . \tag{2.3}$$

By using the WKB approximation, the tunnel current is derived from a constant spin independent DOS. Therefore, both the models of Simmons and Brinkman cannot explain spin dependent tunneling. Slonczewski used a free electron approximation of the spin polarized conduction electrons to describe tunneling in ferromagnet-insulator-ferromagnet structures [32]. The free electron approximation considers the longitudinal part of an effective one electron Hamiltonian. A free electron can be in a spin-up $\uparrow$ or spin-down $\downarrow$ state. The spin-up $\uparrow$ and spin-down $\downarrow$ channels have different wave vectors $\vec{k}_\uparrow$ and $\vec{k}_\downarrow$, respectively. At $\vec{k}_\parallel = 0$ the effective one electron Hamiltonian is solved for both the electron wave functions, in case of parallel and anti-parallel state.

Apart from an effective polarization defined as:

$$P_{\text{eff}} = \left(\frac{k_\uparrow - k_\downarrow}{k_\uparrow + k_\downarrow}\right)\left(\frac{\kappa^2 - k_\uparrow k_\downarrow}{\kappa^2 + k_\uparrow k_\downarrow}\right) \quad , \tag{2.4}$$

where κ is the imaginary part of the electron wave vector in the barrier, the analysis of Slonczewski resulted in a similar expression for the tunnel magnetoresistance effect (TMR) as was proposed by the Jullière model, which is defined by equation 1.2, and is repeated here for clarity:

$$\text{TMR} = \frac{2P_1P_2}{1 + P_1P_2} \quad , \tag{2.5}$$

with P_1 and P_2 the spin polarizations of the magnetic electrodes 1 and 2, respectively. In contrast to the original model of Jullière, in the model of Slonczewski the TMR is dependent on the geometry and electronic structure of the barrier, via employing the effective one electron Hamiltonian.

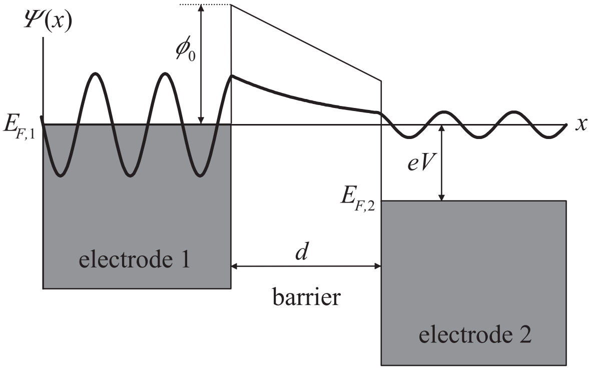

Figure 2.1: Energy potential diagram for a metal-insulator-metal structure, in case electrode 2 is positively biased with a voltage V. The transmitted electron wave function $\Psi(x)$ decays exponentially in the barrier.

As indicated before, the tunnel current that flows through the barrier depends on the relative alignment of the magnetization in the magnetic layers. The parallel and antiparallel state of magnetization generates a logical '0' or '1' as output, respectively. A write operation of an MTJ in a cross-points MRAM architecture is done by sending a current through the intersecting word and bit lines. If the sum of the magnetic fields induced by the two currents is high enough, the magnetization of the MTJ on the intersection can be written. Accordingly, insight in the switching behavior of magnetic elements as a function of the size, shape and thickness is necessary. Besides understanding of the switching of individual elements, also notion of the effect of stray field induced magnetostatic interdot coupling in high areal density arrays of nanoscale MTJs is of significance for technological applications. Therefore, the switching behavior of nanoscale magnetic elements arranged in high areal density arrays and the coupling between neighboring elements is studied in the next section.

2.2 Nanoscale Magnetic Elements

Ferromagnetic materials are characterized by a spontaneous ordering phenomenon below the Curie temperature T_C. This ordering is caused by the exchange interaction, which is based on the Pauli-principle and the Coulomb-interaction. Interesting magnetic properties are expected if the dimensions of a ferromagnetic body are of the same order as the characteristic nanoscopic length scales, like the exchange length.

Consider figure 2.2 that depicts a body of length l, width w and thickness d, with $l > w \gg d$. The body has the easy-axis of magnetization along the y-axis and consists of volume elements $\delta x \delta y \delta z$ of magnetization $\vec{M}_{\mathrm{i}} = M_{\mathrm{s}} \vec{m}$, where $\vec{m}$ is a vector of unit length. An effective field $\vec{H}_{\mathrm{eff}}$ exerts a torque on the magnetization that induces a motion of the magnetization. The direction of $\vec{m}$ varies as a function of the coordinates x, y, z and the saturation magnetization M_{s} has a constant value determined by the temperature.

The magnetization suddenly drops to zero at the surface of the ferromagnetic body. Making use of the Maxwell equation $\vec{\nabla} \cdot \vec{B} = \mu_0 \vec{\nabla} \cdot (\vec{H} + \vec{M}) = 0$, with $\vec{B}$ being the magnetic induction and μ_0 the permeability, we can introduce an anisotropic demagnetizing field $\vec{H}_{\mathrm{D}}$ given by:

$$\vec{\nabla} \cdot \vec{H}_{\mathrm{D}} = -\vec{\nabla} \cdot \vec{M} \quad . \tag{2.6}$$

Applying the divergence theorem [33], we can define an effective magnetic volume charge density $\rho_{\mathrm{V}} = -\vec{\nabla} \cdot \vec{M}$ and an effective magnetic surface charge density $\sigma_{\mathrm{S}} = \vec{n} \cdot \vec{M}$, where $\vec{n}$ is the outward directed surface normal . Using these magnetic charge densities, the scalar potential of the demagnetizing field Φ_{D} at position $\vec{x}$ can be obtained by:

$$\Phi_{\mathrm{D}} = \frac{M_{\mathrm{s}}}{4\pi\mu_0} \left[\int \frac{\rho_{\mathrm{V}}(\vec{x}\,')}{|\vec{x} - \vec{x}\,'|} \mathrm{d}V' + \int \frac{\sigma_{\mathrm{S}}(\vec{x}\,')}{|\vec{x} - \vec{x}\,'|} \mathrm{d}S' \right] \quad , \tag{2.7}$$

and the demagnetizing field can be derived by $\vec{H}_{\mathrm{D}} = -\vec{\nabla}\Phi_{\mathrm{D}} = -\vec{\vec{\mathcal{N}}} \cdot \vec{M}$, where $\vec{\vec{\mathcal{N}}}$ is the demagnetizing tensor. The minus sign points out that the demagnetizing field has an opposite direction to the magnetization. The demagnetizing factors are solely determined by the geometry of the ferromagnetic body and can only be calculated exactly for an ellipsoid, for which the magnetization is uniform throughout the body. Therefore, the demagnetizing factors for arbitrary bodies are usually approximated by the factors of an ellipsoid.

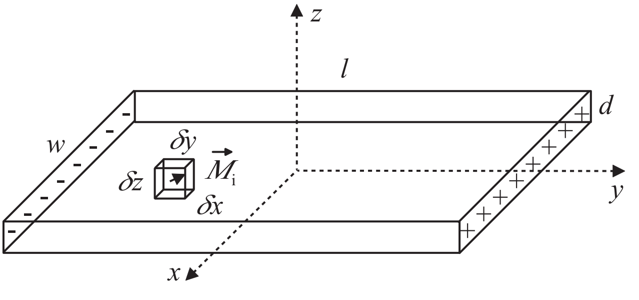

Figure 2.2: A picture of a ferromagnetic body of length l, width w and thickness d, with $l > w \gg d$. The body has the easy-axis along the y-axis and consists of volume elements $\delta x \delta y \delta z$ of magnetization $\vec{M} = M_{\mathrm{s}} \vec{m}$.

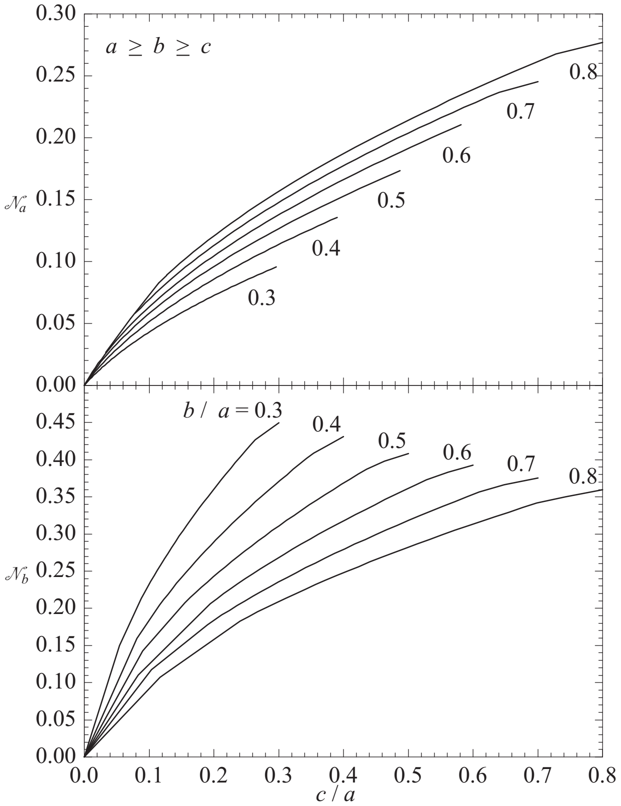

Figure 2.3: Graphs of demagnetizing factors of the general ellipsoid along the a semi-axis (a), and along the b semi-axis (b). The semi-axes of the ellipsoid are $a \geq b \geq c$ [34].

Osborn presented demagnetizing factors of a general ellipsoid for any principal axis of the ellipsoid of any shape [34]. The demagnetizing factors along the a semi-axis $\mathcal{N}_\mathrm{a}$ and along the b semi-axis $\mathcal{N}_\mathrm{b}$ are plotted in figure 2.3 for a general ellipsoid with $a \geq b \geq c$, where a, b, and c are the ellipsoid semi-axes. The corresponding demagnetizing factors along the c semi-axis $\mathcal{N}_\mathrm{c}$ can be determined with the relationship $\mathcal{N}_\mathrm{a} + \mathcal{N}_\mathrm{b} + \mathcal{N}_\mathrm{c} = 1$ that exists between the demagnetizing factors of an ellipsoid.

Due to the demagnetizing effect of the surface, a ferromagnetic body is normally not uniformly magnetized but consists of domains magnetized in opposite directions at the expense of introducing exchange energy. The transitional layer between adjacent domains is called the domain wall and is formed to avoid stray fields and to minimize the total energy [35]. However, in nanoscale magnetic elements the formation of domains is suppressed, because the energy associated with the formation of a domain wall exceeds that of the stray field energy of a uniform magnetized body [36].

The single domain size depends on the shape and the material parameters of the element [37]. Although, a true single domain state only exists for ellipsoids, the magnetization configuration of sub - 100 nm magnetic elements approaches a single domain state, such as a flower state, a c-state and a s-state, depending on anisotropy [38]. The ground state of the magnetization configuration of a nanoscale magnetic element with uniaxial anisotropy can be determined by evaluating the total energy of the element:

$$E_{\text{tot}} = \int (A|\nabla\vec{M}|^2 + K(\alpha_x\alpha_y\ +\ \alpha_y\alpha_z\ +\ \alpha_z\alpha_x) - \frac{\mu_0}{2}\vec{M}\cdot\vec{H}_{\text{D}} - \mu_0\vec{M}\cdot\vec{H}_{\text{Appl}})\mathrm{d}V \quad , \tag{2.8}$$

exchange- **anisotropy-** **magnetostatic-** **Zeeman energy**

with A being the exchange stiffness constant, K the anisotropy constant, $(\alpha_x,\ \alpha_y,\ \alpha_z)$ the direction cosines of the magnetization, and $\vec{H}_{\text{Appl}}$ an applied magnetic field. The complicated nonlinear energy equations can be linearized when the magnetization direction is nearly uniform. Brown used the variational principle to determine the linearized micromagnetic equations for an element of suitable geometry in a large uniform magnetic field [39]. Two relevant modes of coherent magnetization reversal that are analytic solutions of Brown's equations exist in an ellipsoid. One mode corresponds to the Stoner-Wohlfarth model and the other is described by the Curling model.

The Stoner-Wohlfarth model is characterized by a constant exchange energy which implies that the magnetic moments remain parallel during the magnetization reversal, as is illustrated in figure 2.4(a). When a magnetic field $\vec{H}_{\text{Appl}}$ is applied parallel to the easy-axis of a prolate spheroid with semi-axes $a > b$, the switching field for this mode is given by [40]:

$$H_{\text{SW}} = \frac{2K}{\mu_0 M_{\text{s}}} + (\mathcal{N}_{\text{b}} - \mathcal{N}_{\text{a}})M_{\text{s}} \quad . \tag{2.9}$$

In addition to the Stoner-Wohlfarth model, Frei *et al.* proposed the Curling model in which the magnetic moments are not constrained to be parallel in order to reduce the

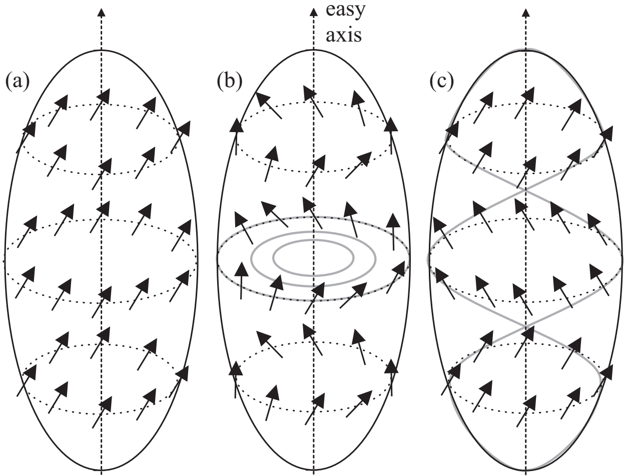

Figure 2.4: Illustration of the coherent magnetization reversal modes in a single-domain prolate spheroid corresponding to the Stoner-Wohlfarth model (a) and the Curling model (b), and a representation of quasi-coherent magnetization reversal described by the Buckling mode (c).

magnetostatic energy. Figure 2.4(b) shows the configuration of the magnetic moments described by the Curling model. In the Curling case, the magnetization reverses by rotating the magnetic moments from the a semi-axis in a plane perpendicular to the radius of the ellipsoid. The competition between the exchange energy and the demagnetization energy determines the switching field. The nucleation field for switching in the Curling mode is derived from Bessel functions of the first kind of order 1, and is given by [41]:

$$H_\mathrm{C} = \frac{2K}{\mu_0 M_\mathrm{s}} - \mathcal{N}_\mathrm{a} M_\mathrm{s} + \frac{8\pi A\xi}{\mu_0 M_\mathrm{s} b^2} \quad , \tag{2.10}$$

where ξ is a monotonically increasing function of the aspect ratio $b : a$ that is plotted in figure 2.5 [42]. The plot shows that the nucleation field is virtually independent of the b semi-axis, because $1.07 < \xi < 1.38$ and large b the last term of equation 2.10 approaches zero.

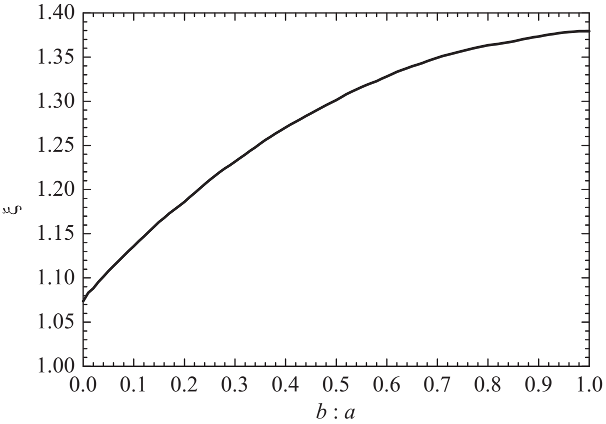

Figure 2.5: Graph of the parameter ξ of equation 2.10 as function of the aspect ratio $b : a$ of a prolate spheroid [42].

As mentioned before, the nanoscale element under consideration that is pictured in figure 2.2 has a thickness $d \ll w < l$ of the order of the exchange length, and where l is the length and w the width of the element. For such a flat element the Curling mode is energetically not favorable on account of the induced exchange energy.

However, if the magnetic moments are assumed to only rotate in the b semi-axis direction with a sinusoidal variation of the amplitude along the a semi-axis, the increase in exchange energy can be compensated by an decrease in magnetostatic energy [43]. This magnetization reversal mode is known as the Buckling mode and the magnetization reversal occurs by quasi-coherent rotation, which is sketched in figure 2.4(c).

In order to get a flavor of this quasi-coherent Buckling mode, we have computed the spin configuration states in an elliptical element during magnetization reversal using the Object-Oriented MicroMagnetic Framework (OOMMF) [44]. The elliptical element has a major axis of 720 nm, a minor axis of 300 nm and a thickness of 5 nm, and the element is divided into a two-dimensional grid of 5×5 nm^2 cells. Co is used as material for the input parameters for the computations, with saturation magnetization $M_s = 1400$ kA/m,

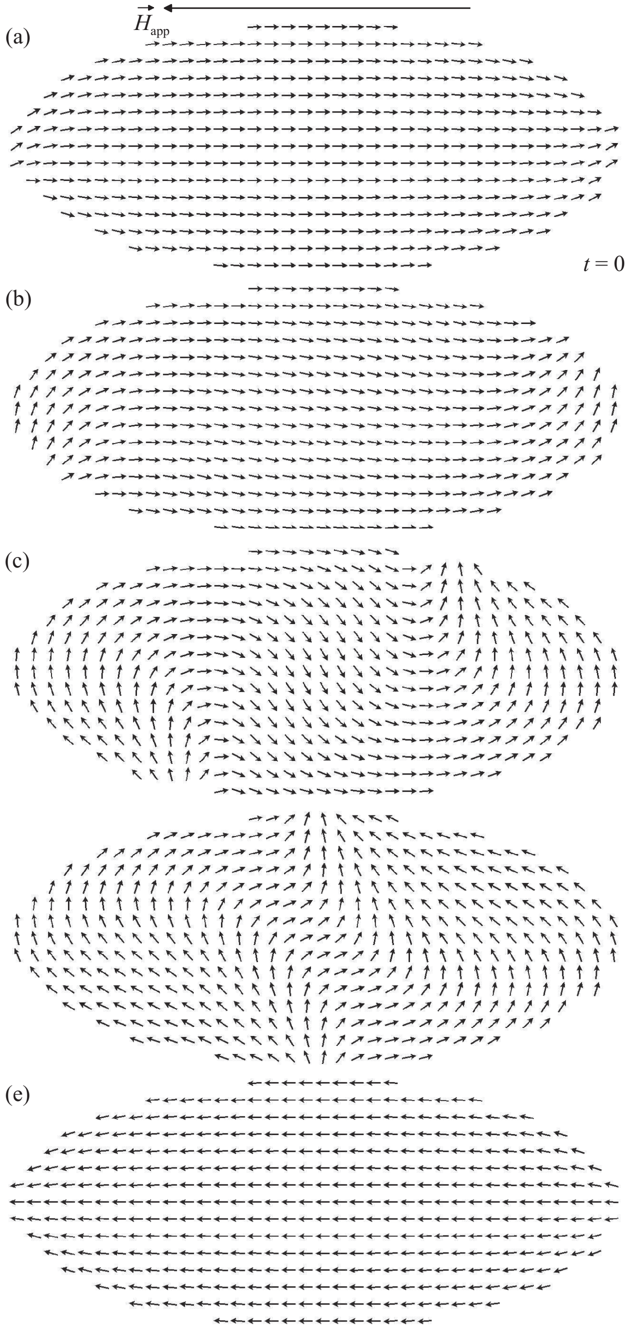

Figure 2.6: Spin configuration in an elliptical element during magnetization reversal in Buckling mode at -17.5 kA/m. The dimensions of the element are 720 nm along the major axis, 300 nm along the minor axis, and a thickness of 5 nm.

exchange stiffness $A = 30$ pJ/m. Figure 2.6 shows the different spin configuration states in the elliptical element during magnetization reversal in the Buckling mode, where a reduced spin configuration is used for clarity.

Starting from a uniform magnetized state, the magnetic moments are permitted to relax at zero field. The resulting spin configuration resembles the s-state and is shown in figure 2.6(a). Under a reversed magnetic field of-17.5 kA/m, switched on at $t = 0$ s, the Buckling instability occurs that starts with the nucleation of a planar Buckling wave shown 2.6(b). The magnetization configuration shows an upward rotation of the moments at the left and right end, and a downward rotation in the center. Figure 2.6(c) shows the nucleation of vortices arising from a constantly increasing amplitude of the Buckling wave. Figure 2.6(d) shows the annihilation of the vortices. Finally, the element approaches the single domain configuration again, which is shown in figure 2.6(e). For thin soft elliptical elements with a moderate aspect ratio, the Buckling instability mode is proved to be the easiest nucleation mode [45]. However, for thin enough elements with a homogeneous magnetization throughout the thickness direction, the Stoner-Wohlfarth model gives an upper bound for the switching field and can serve as an approximation [46].

2.3 Coupling Phenomena in Nanoscale MTJs

Understanding of the individual switching behavior of nanoscale magnetic elements as a function of the size, shape and thickness is important for technological applications. Besides that, the collective properties of high areal density arrays of magnetic elements are of interest. High areal density arrays with sub-100 nm magnetic elements in a single domain magnetization configuration induce stray fields that can lead to magnetostatic interdot coupling. Interdot coupling can induce an alternation of the switching field and can effect the nucleation cascade [47].

Besides interdot coupling, the roughness-induced Néel coupling can disrupt the switching of the magnetic layers of the nanoscale magnetic tunnel junctions (MTJs). To stabilize the switching behavior of the two magnetic layers, one of the ferromagnetic (FM) layers can be pinned by exchange bias coupling to an adjacent layer of antiferromagnetic (AF) material. In this section, we investigate the effect of the mentioned coupling phenomena. First the interlayer coupling is discussed, after that the interdot coupling is described.

2.3.1 Interlayer Coupling Mechanisms

In section 1.2 the engineered MTJ multilayer stack is described to promote stability and reproducibility of the MTJ response. The magnetic switching of the complex MTJ stack is significantly affected by several interlayer coupling phenomena.

An example is the Néel coupling between two adjacent ferromagnetic films FM1 and FM2, with thicknesses d_{FM1} and d_{FM2}, respectively, which are separated by a barrier with thickness d_{bar}. The Néel coupling is due to magnetic dipoles at the interfaces induced by a corrrelated roughness with wavelength λ and amplitude h, as is indicated in figure 2.7.

The arrows in figure 2.7 indicate the direction of the magnetization in the ferromagnetic layers. Assume a uniform magnetization in the two layers and let M_{FM1} be the magnetization of layer FM1 and M_{FM2} the magnetization of layer FM2. Kools *et al.* derived an equation for the Néel coupling field of the ferromagnetic film FM1 with thickness d_{FM1} given by [48]:

$$H_{\mathrm{N}} = \frac{\pi h^2 M_{\mathrm{FM2}}\zeta}{4d_{\mathrm{FM1}}} \exp(-\zeta d_{\mathrm{bar}})[1-\exp(-\zeta d_{\mathrm{FM1}})][1-\exp(-\zeta d_{\mathrm{FM2}})] \quad , \tag{2.11}$$

with ζ defined as $\zeta = \frac{2\pi\sqrt{2}}{\lambda}$. From equation 2.11 we can see that the Néel coupling field is extremely sensitive to the roughness of the interfaces. In addition, the barrier thickness has an important influence on the coupling, the thinner the barrier the higher the Néel field.

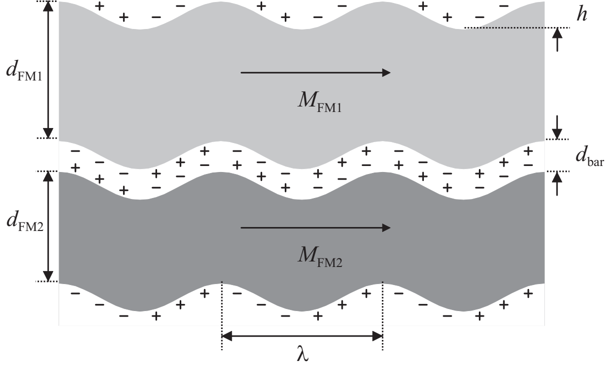

Figure 2.7: Schematic of the Néel coupling between two adjacent ferromagnetic films FM1 and FM2, due to magnetic dipoles at the interfaces induced by surface roughness.

In order to enable an independent switch of the two magnetic layers separated by an ultra thin barrier, one of the ferromagnetic (FM) layers can be pinned to an adjacent layer of antiferromagnetic (AF) material. The pinning between a FM and an AF layer is caused by exchange bias (EB) coupling that was discovered by Meiklejohn and Bean [49]. The exchange bias coupling produces an easy-axis in the direction of the magnetic field that was applied during cooling of the FM/AF system from above the blocking temperature. Investigations of the spin structure at a FM/AF interface revealed that uncompensated magnetic moments of the AF layer couple ferromagnetically with the moments of the FM [50]. A manifestation of the EB coupling is a field shift of the center of the hysteresis loop, which is inversely proportional to the magnetization and the thickness of the FM layer.

Both the Néel coupling and the EB coupling are only dependent on the layer thicknesses and are independent of the size and shape of a MTJ. However, the magnetostatic interlayer coupling favors an antiparallel alignment of the magnetic layers and scales with the inverse of the length and width of the MTJ. Therefore, a significant magnetostatic interlayer coupling can obstruct independent switching of the magnetic layers of a nanoscale MTJs.

Heim *et al.* solved the problem of magnetostatic interlayer coupling by replacing the pinned FM by an artificial antiferromagnet (AAF), which comprises a sandwich of two FM layers that are antiferromagnetically coupled via a less than 10 Å thin Ru layer [51]. Since the two FM layers are aligned antiparallel, the magnetic moments of the layers can essentially cancel out one another by selecting FM layers of equal thickness. Consequently, there is virtually no stray field to adversely affect the free FM layer. The strength of the antiferromagnetic coupling oscillates in magnitude with the Ru spacer layer thickness and has a period of about 5 to 10 monolayers [52]. The oscillatory coupling between FM layers separated by a Ru spacer layer relies on an indirect exchange coupling mechanism. Experimental observations were explained in terms of the topological properties of the Ru Fermi surface using an extended Ruderman-Kittel-Kasuya-Yosida (RKKY) exchange theory [53].

2.3.2 Magnetostatic Interdot Coupling

Besides the influence of interlayer coupling on the switching behavior nanoscale MTJs, also the interdot coupling can have a significant effect on the magnetic switching behavior of high areal density arrays with sub - 100 nm elements. As is known, the effect is strongly dependent on the size of the dots and their arrangement in the lattice array. However, the actual effect of interdot coupling on the switching behavior is hard to comprehend. In order to estimate the magnitude of the interdot coupling effect and to get a sense of the influence on the switching behavior, we discuss some simplified examples that have the same dot geometry and array arrangement as the fabricated arrays of nanoscale MTJs investigated within this Thesis.

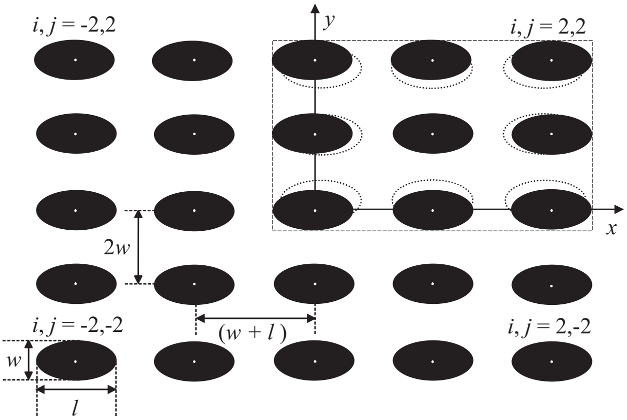

Figure 2.8: Representation of a $n \times n$ array, with $n = 5$, of elliptical Co dots of length l, width w, and thickness d, arranged on a rectangular lattice with a dot spacing of $2w$ along the minor axis and $(w+l)$ along the major axis. The dotted ellipses in the dashed frame illustrate a 25 % decrease of the distance between the dots.

Consider $n \times n$ arrays, with n odd, of polycrystalline elliptical Co dots with length l, width w, and thickness d, as is represented in figure 2.8. The dots are arranged on a rectangular lattice with a dot spacing of $2w$ along the minor axis and $(w + l)$ along the major axis. The spacings are defined as the distance between the center of the dots. The dots are located at the positions $(w + l)i\vec{e}_x + 2wj\vec{e}_y$, where i and j are integers, and $\vec{e}_x$ and $\vec{e}_y$ are unit vectors along the axes.

Assume a uniform single domain magnetization distribution in the dots, which lies in the plane of the film along the major axis of the dots. Furthermore, we approximate the macrospins dots by point dipoles. We can determine the magnetic interdot field at the dot located at the center of the rectangular lattice, generated by all other dots by:

$$\vec{H}_{\text{I}} = \frac{M_{\text{s}}\vec{m}lwd}{8} \sum_{\substack{i,j = -\infty \\ i,j \neq 0}}^{\infty} \frac{1}{[(w+l)^2 i^2 + 4w^2 j^2]^{3/2}} \quad . \tag{2.12}$$

In case of a square lattice and circular dots, the obtained result converts to the result reported by Min [54]. Equation 2.12 can serve to estimate the magnitude of the interdot field and to reveal the dependency on dot geometry and array arrangement. For several situations the strength of the interdot field at the central Co dot is calculated as a function of the number n of $n \times n$ arrays and is plotted in figure 2.9.

Notice, that after an initial sharp increase, for all the calculated situations the interdot field converges to a considerable value. For example, in case of a $10^4 \times 10^4$ array of ellipses, with major axis $l = 100$ nm and the minor axis $w = 50$ nm, the interdot field in the direction of the applied field is approximately 110 kA/m. The interdot field for Co dots of width $w = 50$ nm and length to width aspect ratios 1.5, 2, and 2.5, respectively increases with increasing ratio of the dots due to the increase of magnetic moment, because the distance between the Co dots is kept constant.

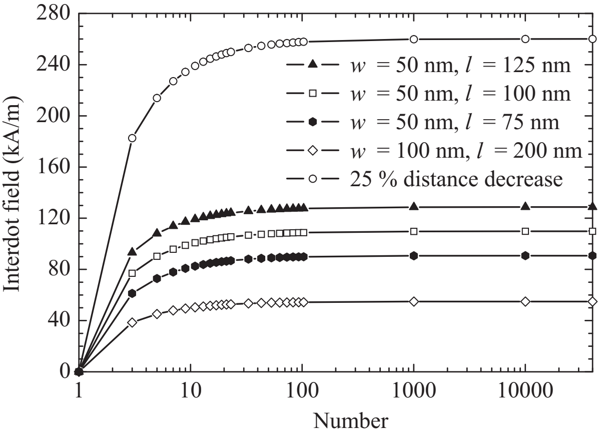

Figure 2.9: Graph of the interdot field at the central Co dot as a function of the number n of $n \times n$ arrays.

Furthermore, for the defined lattice configuration and under the restriction that the aspect ratio is constant, the interdot field increases with decreasing distance between the dots. The distance between the dots has a tremendous influence on the interdot field. As an illustration of this influence, the interdot field is calculated for a $10^4 \times 10^4$ array of the ellipses with $l = 100$ nm and $w = 50$ nm with a 25 % decrease of the distance between the dots. The decrease in distance is depicted by the dotted 3×3 top right ellipses within the dashed frame in figure 2.8. The calculated interdot field is almost 260 kA/m, which is an increase of 2.4 in comparison to the defined lattice configuration.

Although the calculation clearly demonstrates the evident influence of the interdot field, a quantitative estimate of the effect on the switching field is non-trivial, since a uniform magnetization distribution in the plane of the film along the major axis in all the dots is not plausible. Besides that, the dots have different orientations of the magnetization. In order to minimize the magnetostatic energy that arises from the uncompensated magnetic poles at the array edges, the magnetization of the edge dots of the array will rearrange. The rearrangement processes of the magnetization generate an orientation dependency, which is called configurational array anisotropy [55]. Via the dipolar stray fields, this configurational array anisotropy produces interactions between neighboring Co dots and forms clusters of approximate flux closure.

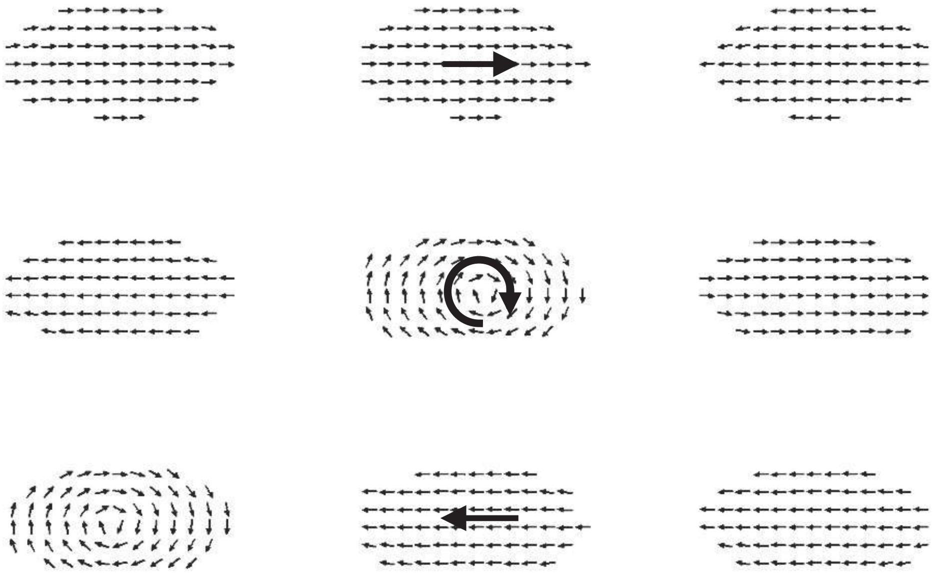

Figure 2.10: Resulting magnetization configuration of OOMMF *simulations of a* 3×3 *array of ellipses with a major axis of* $l =$ *200 nm and a minor axis of* $w =$ *100 nm.*

OOMMF micromagnetic simulations are performed to visualize this approximate flux closure. Figure 2.10 shows a typical magnetization configuration resulting from simulations of a 3×3 array of ellipses with a major axis of $l = 200$ nm and a minor axis of $w = 100$ nm. The ellipses are divided into two-dimensional grids of 5×5 nm^2 cells. As input parameters for the computations, we used Co as material with saturation magnetization $M_s = 1400$ kA/m, exchange stiffness $A = 30$ pJ/m. For clarity, a reduced spin configuration is used.

The conducted simulation showed that a uniform magnetization in the plane of the film along the major axis of the ellipses is not the ground state of the array. However, the simulations revealed a vortex state for the ellipse located at the center of the array, as is indicated with the arrow in figure 2.10. The magnetization configuration of the ellipses above and below the central ellipse persecutes the circulation sense of the vortex of the central ellipse. The ellipses at the corners of the array had a magnetization configuration that varied for different simulations, and occasionally one of the corner ellipses was in a vortex state, like is shown in the bottom left ellipse of figure 2.10. The configuration of the left and right ellipses also varied and was dependent on the configuration of the corner ellipses. Concisely, due to interactions between neighboring ellipses there is a tendency to rearrange the magnetization configuration of the array approximating a flux closure.

The OOMMF micromagnetic simulations did not yield an unambiguous ground state of the magnetization configuration of the array. Therefore, an assessment of the approximate flux closure effect on the switching behavior is difficult. Nevertheless, in order to provide insight into the consequences of the approximate flux closure on the switching behavior, we simulated the magnetic switching in an $n \times n$ array of ellipses, with n being 1, 3 and 7. The major axis of the ellipses has a length of $l = 100$ nm and the minor axis a width of $w = 50$ nm, the distance between the ellipses is 50 nm. Again, a two-dimensional grid of 5×5 nm^2 cells and the Co properties are chosen as input parameters for the computations. The magnetic field is applied along the major axis of the ellipses. The resulting hysteresis loops are plotted in figure 2.11.

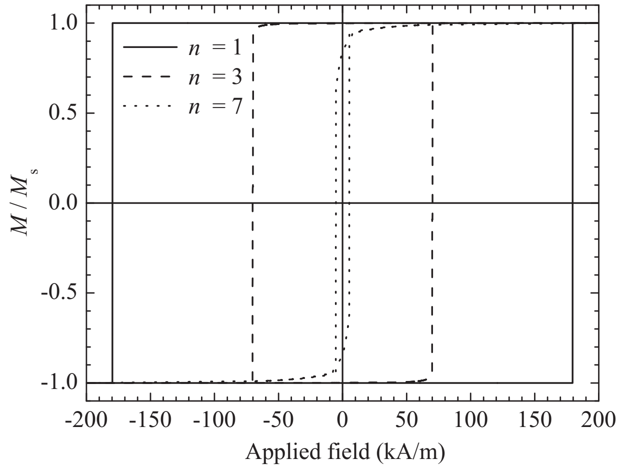

Figure 2.11: OOMMF hysteresis loop computations of three $n \times n$ arrays of ellipses , with n being 1, 3 and 7. The ellipses have a major axis of $l = 100$ nm and a minor axis of $w = 50$ nm, the distance between the ellipses is 50 nm.

The hysteresis loop of the individual ellipse shows a sharp switch at approximately 180 kA/m. The magnetic moments of the ellipses in the 3×3 array first gradually start to rotate before the magnetization reversal at about 70 kA/m. The calculated interdot field at the center of the 3×3 array is 77 kA/m, which can be derived from figure 2.9. For the specific array arrangement that we used, the calculated interdot field gives a lower bound for the influence of interdot coupling on the switching field. Furthermore, figure 2.11 shows a collapse of the coercive field to roughly 5 kA/m for the 7×7 array of ellipses.

The calculated values of interdot fields of arrays of closely spaced Co dots and the coercive field collapse has to be taken into account when the experimental data are analyzed. Furthermore, the influence of interdot coupling implies that for the feasibility of ultra-high areal density arrays of nanoscale MTJs for information storage new strategies are needed.

Chapter 3

Multilayer Stack Preparation

In section 1.2, we described the multilayer engineering of nanoscale magnetic tunnel junctions (MTJs) for magnetic random access memories (MRAMs) applications. Top-down nanostructuring techniques are used for the fabrication of the nanoscale MTJs, which are used in this Thesis to characterize the magnetic and electrical properties. Therefore, substrates with a multilayer stack have to be prepared. The preparation process consists of cleaning the substrate, sputter depositing the multilayer stack, and creating a tunnel barrier by plasma oxidation. These topics and *in situ* characterization techniques will be discussed successively in this chapter.

3.1 Sputter Deposition of the Multilayer Stack

For the preparation of the multilayer stacks described in this Thesis, we used the Eindhoven University nano-Film depOsition Research and Analysis Center (EUFORAC). Figure 3.1 shows a photograph of the *EUFORAC*, which is an ultrahigh vacuum system for deposition, oxidation, and in situ characterization of samples. AlO_x based MTJ multilayer stacks on Si(001) substrates without metal-oxide-semiconductor (CMOS) circuits are produced, to shorten the sample fabrication time for rapidly characterizing the magnetic and electrical properties of the nanoscale MTJs.

Before sputter deposition of the multilayer stacks the substrates have to be cleaned. The cleaning procedure of the substrates contains several steps, partly *ex situ* and partly *in situ*. First, a substrate is cleaned *ex situ* by an ultrasonic ammonia bath and an ultrasonic acetone bath for 15 minutes. Afterwards, the substrate is rinsed with isopropanol and kept in an isopropanol vapor bath until the substrate can be mounted on a holder and loaded into the load-lock of the *EUFORAC*. Next, the holder is transported to the oxidation chamber connected to the sputtering system. In the chamber, the hydrocarbon residues from the *ex situ* cleaning procedure are removed *in situ* from the surface by exposing the substrate to an oxygen plasma for 5 minutes. Finally, after pumping down the oxidation chamber to a base pressure of $< 10^{-9}$ mbar, the holder is transported to the sputtering system to deposit the multilayer stack.

The deposition of the multilayers is performed in the *Kurt J. Lesker, Ltd.* magnetron sputtering system with a base pressure of $< 10^{-8}$ mbar, shown in figure 3.1. This system has six magnetron sputter sources operable in *dc* or rf mode. The substrates can be

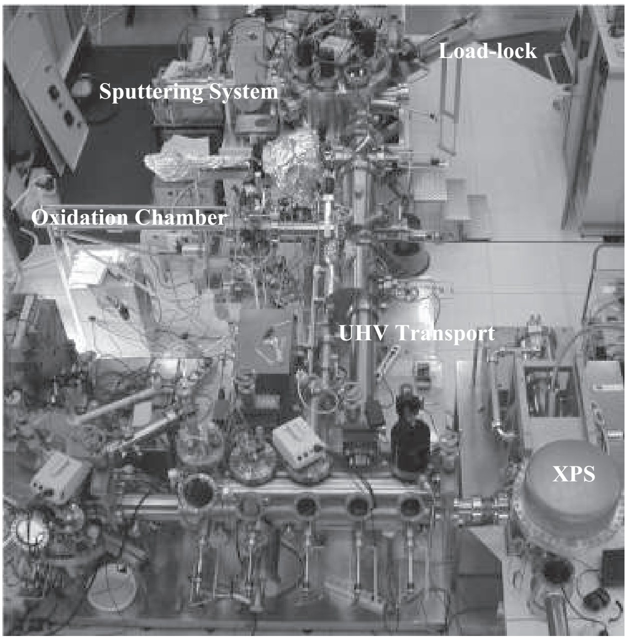

Figure 3.1: Photograph of an ultrahigh vacuum system for deposition, oxidation, and in situ characterization of samples, called the EUFORAC. The EUFORAC is used for the preparation of the multilayer stacks described in this Thesis.

positioned under the individual sources with the movable sample holder stage. The layers were deposited at a rate of approximately 0.5 Å/s at a power of 20 W in an Ar pressure of $\approx 10^{-2}$ mbar. The deposition is started and ended by opening and closing a shutter between the target and substrate.

In figure 3.2, the basic physical principles behind sputter deposition are explained, an elaborate overview is given elsewhere [56]. The sputter target of deposition material is placed at a potential of the order of -100 to -1000 V in an Ar gas environment. A ring-shaped anode generates a voltage difference that ignites a plasma in which Ar^+ ions are accelerated towards the sputter target. When the incident Ar^+ ions collide with the target surface atoms, kinetic energy is transferred displacing the surface atoms, thereby ejecting atoms from the surface. The target atoms ballistically disperse outwards and coat the substrate, which is positioned below the target. The probability of ion collisions is enhanced by placing a magnet above the sputter target. Due to the magnet, the charged particles in the plasma experience a magnetic field in addition to the electric field. The magnetic field forces the charged particles to move in helical orbits, essentially confining the electrons close to the target and thereby increase the efficiency of sputtering process [57]. Sputter deposition in the presence of a magnetic field is referred to as magnetron sputter deposition.

After depositing the Al layer, the sample holder is transported to the oxidation chamber with a base pressure of $< 10^{-9}$ mbar, to fabricate the Al_2O_3 barrier. The holder is positioned below a pure Al ring electrode that is at a potential of approximately -700 V with respect to a grounded top electrode. A ring-shaped ground plate is placed approximately 2 cm below the Al electrode, to shield the sample from ion bombardment and additional Al deposition on the sample. In order to create a non-flowing plasma, first a small pre-volume is filled with O_2 gas to a pressure of 26.5 mbar, which is let into the chamber by pneumatically opening a valve. The O_2 gas expands to a pressure of 0.1 mbar and ionizes instantaneously creating a stable oxygen plasma in less than about 1.5 s. Plasma oxidation of Al is governed by O-atoms as well as O-ions via two independent mechanisms. These mechanisms are described in a novel model [58].

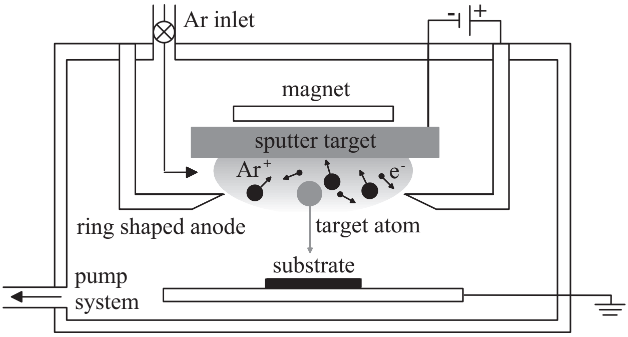

Figure 3.2: The principle of the sputter deposition technique, using a ring-shaped anode to generate a voltage difference for the ignition of an Ar plasma.

The first mechanism concerns the O-atoms, which have a lower energy surface then the Fermi level of the Al. Therefore, more electrons tunnel from the metal towards the surface than from the surface towards de metal. These tunneling electrons set up an electric field in the oxide, and thereby lowering the activation barrier for Al-ion hopping. After hopping into the AlO_x, an Al-ion diffuses rapidly to the surface due to this electric field.

The second mechanism involves the O-ions that very locally deliver a large amount of energy when hitting the surface of the sample. Due to this so called thermal spike, the temperature increases in the impact area. As a consequence the probability of an Al-ion hopping into the AlOx will increase. This increase in temperature due to this thermal spike is lower for thicker Al layers, since the energy is divided over much more atoms.

3.1.1 Sample Description

The configuration of a magnetically engineered MTJ multilayer stack for MRAM application is discussed in section 1.2. Here, the composition is described of the different types of multilayer stacks that we produced to study the magnetic and electric properties. We have chosen not too much to vary the sequence of the multilayer stack, because the various nanofabrication processes strongly depend on the used materials and layer thicknesses. Apart from the reference samples that are used for detail studies, we produced two different types of multilayer stacks. One type of stack will be structured to produce samples that are labeled magnetometry samples and will be used for the characterization of the magnetic properties. We used another type of stack to produce samples entitled c-AFM samples for the electrical characterization.

- The composition of the multilayer stacks of the magnetometry samples for the magnetic characterization is:
  Si(001)/ SiO_x// 50 Å Ta/ 25 Å Co/ 100 Å IrMn/ 40 Å Co/ 8 Å Ru/ 40 Å Co/ 11 Å AlO_x/ 50 Å $Co_{60}Fe_{20}B_{20}$/ 150 Å Ta.
- The multilayer stacks of the c-AFM sample to characterize the electrical properties consist of:
  Si(001)/ SiO_x// 50 Å Ta/ 25 Å $Co_{90}Fe_{10}$/ 100 Å IrMn/ 40 Å $Co_{90}Fe_{10}$/ 8 Å Ru/ 40 Å $Co_{90}Fe_{10}$/ 11 Å AlO_x/ 50 Å $Co_{90}Fe_{10}$/ 50 Å Ta.

In the stack sequences only the ferromagnetic material is varied, on account of the arbitrariness of availability. Furthermore, also the layers have equal thicknesses, except for the thickness of the Ta capping layer. The magnetometry samples have an extra thick capping layer in order to fabricate a hard Ta mask, which is used to prevent mask erosion during the deep Ar^+ ion beam milling of the nanoscale MTJs.

3.2 *In situ* Characterization Techniques

The *EUFORAC* is equipped with a differential ellipsometer and an X-ray photoelectron spectroscopy (XPS) apparatus for *in situ* characterization of samples. The *in situ* differential ellipsometer is used to monitor the plasma oxidation dynamics of Al layers in real-time. XPS measurements are performed to investigate the oxidation condition of sub-nm AlO_x barriers and the underlying electrodes. In this section, we describe the characterization techniques that are used to control the plasma oxidation of sub-nm thin Al layers.

3.2.1 Differential Ellipsometer

A schematic picture of the *in situ* differential ellipsometer is shown in figure 3.3. Details of the implementation have been reported before [59]. Here we give the principles of ellipsometry to characterize the Al_2O_3 growth during plasma oxidation of an Al layer. Ellipsometry is a technique that utilizes the phenomenon that the polarization state of a light beam changes when reflecting from and passing through an interface between two media with a different complex index of refraction [60]:

$$\tilde{n} = n + i\kappa \quad , \tag{3.1}$$

with n the index of refraction and κ the extinction coefficient.

Suppose that light from a 3 mW HeNe laser with a wavelength of $\lambda = 632.8$ nm passes through a polarizer, which polarizes the laser light perpendicular (s-polarized). In a vacuum chamber, the light is incident at an angle of $\phi_\mathrm{i} = 45°$ to the surface of a sample, which is composed of a bilayer of Al_2O_3 and Al. For dielectric materials such as Al_2O_3, $\kappa = 0$ in the visible regime. As a consequence Al_2O_3 is transparent at $\lambda = 632.8$ nm. This in contrast to Al with complex index of refraction $\tilde{n}_\mathrm{Al} = 1.377 + 7.614i$ [61]. Due to this difference, the increase of the Al_2O_3 thickness Δd during growth can be determined by monitoring the optical response of the s-polarized light as a function of the decrease of the initial Al thickness d.

When s-polarized light is incident on the sample surface, part of the light is reflected and some is transmitted, as is shown in figure 3.4. With $\tilde{n}_\mathrm{vac} = 1$, and $\cos(\phi_\mathrm{i}) = \frac{1}{2}\sqrt{2}$, the

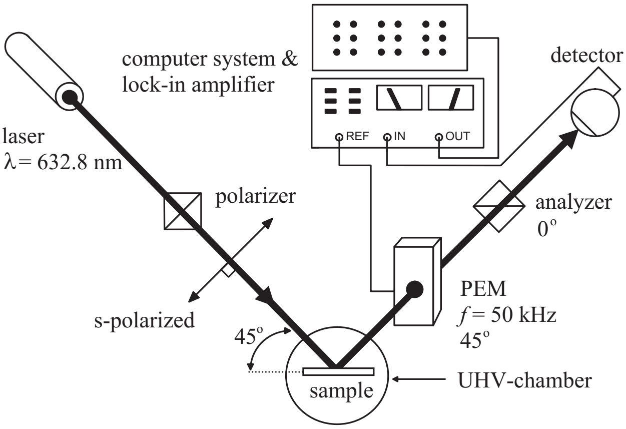
computer system &
lock-in amplifier
detector
REF
IN
OUT
laser
λ= 632.8 nm
polarizer
analyzer
0°
s-polarized
PEM
f= 50 kHz
45°
45°
sample
UHV-chamber

Figure 3.3: Schematic picture of the in situ differential ellipsometer for monitoring the plasma oxidation dynamics of Al layers in real-time.

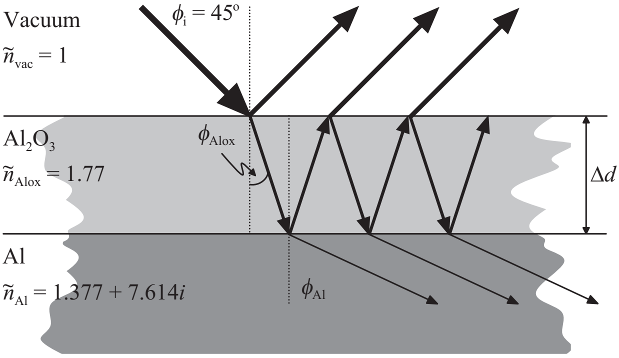
Vacuum
$\tilde{n}_{\text{vac}} = 1$
$\phi_{\text{i}} = 45°$
Al_2O_3
$\tilde{n}_{\text{Alox}} = 1.77$
ϕ_{Alox}
Δd
Al
$\tilde{n}_{\text{Al}} = 1.377 + 7.614i$
ϕ_{Al}

Figure 3.4: Reflections and transmissions in a sample composed of a bilayer of Al_2O_3 - Al, situated in a vacuum chamber.

Fresnel reflection- and transmission coefficients for the vacuum - Al_2O_3 interface are given by [62]:

$$r_{\text{vac,Alox}} = \frac{\tilde{n}_{\text{vac}} \cos(\phi_{\text{i}}) - \tilde{n}_{\text{Alox}} \cos(\phi_{\text{Alox}})}{\tilde{n}_{\text{vac}} \cos(\phi_{\text{i}}) + \tilde{n}_{\text{Alox}} \cos(\phi_{\text{Alox}})} = \frac{\sqrt{2} - 2n_{\text{Alox}} \cos(\phi_{\text{Alox}})}{\sqrt{2} + 2n_{\text{Alox}} \cos(\phi_{\text{Alox}})} \quad , \tag{3.2}$$

and

$$t_{\text{vac,Alox}} = \frac{2\tilde{n}_{\text{vac}} \cos(\phi_{\text{i}})}{\tilde{n}_{\text{vac}} \cos(\phi_{\text{i}}) + \tilde{n}_{\text{Alox}} \cos(\phi_{\text{Alox}})} = \frac{2\sqrt{2}}{\sqrt{2} + 2n_{\text{Alox}} \cos(\phi_{\text{Alox}})} \quad , \tag{3.3}$$

where ϕ_{Alox} is the refraction angle in the Al_2O_3 layer, determined by Snell's law [63]:

$$\tilde{n}_{\text{vac}} \sin(\phi_{\text{i}}) = \sin(45°) = \tfrac{1}{2}\sqrt{2} = \tilde{n}_{\text{Alox}} \sin(\phi_{\text{Alox}}) \quad . \tag{3.4}$$

The transmitted light hits the interface between Al_2O_3 and Al, again some light is reflected and some is transmitted. The light that ultimately is returning to the vacuum after multiple internal reflections is represented schematically in figure 3.4. The resulting reflection to the vacuum can be calculated using the total reflection coefficient for s-polarized light in a vacuum - Al_2O_3 - Al system [64]:

$$R^{\mathrm{s}} = \frac{r_{\mathrm{vac,Alox}} + r_{\mathrm{Alox,Al}} \exp(-i2\beta)}{1 + r_{\mathrm{vac,Alox}} r_{\mathrm{Alox,Al}} \exp(-i2\beta)} \quad . \tag{3.5}$$

Here, $r_{\mathrm{Alox,Al}}$ is the Fresnel reflection coefficient for the Al_2O_3 - Al interface. The film phase thickness β is given by:

$$\beta = 2\pi \left(\frac{\Delta d}{\lambda}\right) n_{\mathrm{Alox}} \cos(\phi_{\mathrm{Alox}}) \quad . \tag{3.6}$$

The resulting reflected laser light passes through a photo-elastic modulator (PEM), operating at frequency $f = 50$ kHz and the modulation axis set at 45° relative to the s-polarized laser light. After that, the light passes an analyzer, before the intensity of the reflected light is measured by a detector. The modulation frequency of the PEM is used as the reference signal for the lock-in amplifier to detect the signal. An increases of the Al_2O_3 thickness Δd due to oxidation will be reflected by changes in the lock-in signal. Explicit modeling of the optical response of the bilayered system revealed that the signal at $2f$ is approximately linearly proportional to the amount of oxidized metallic material [65]. More specifically, the proportionality factor deviates by no more than ± 5 % for the sub - nm AlO_x films.

3.2.2 X-ray Photoelectron Spectroscopy

XPS measurements are performed to investigate the stoichiometry of sub - nm AlO_x barriers after plasma oxidation. XPS is a surface-sensitive analysis method with an information depth of a few nanometers, and has been applied to study thin AlO_x based tunnel barriers before [66]. In this thesis, *in situ* XPS measurements are used to investigate the oxidation condition of sub - nm AlO_x barriers and the underlying $Co_{90}Fe_{10}$ electrodes. Here, the basic principles of the XPS technique will be discussed, a more elaborate overview can be found elsewhere [67].

The XPS principle is depicted in figure 3.5(a). An Mg source produces K_α X-ray radiation with an energy of $\hbar\omega = 1253.6$ eV. The X-rays impinge on the sample and ionize atoms ejecting core electrons. Figure 3.5(b) illustrate the ejection of a photoelectron, from the 1s level into the vacuum, by incident X-rays. The electronic configuration of every element is unique. Therefore, the binding energy E_{B} of the photoelectron ejected from the core orbit is characteristic for an element. This binding energy can be determined by measuring the intensity of the photoelectrons as a function of the kinetic energy E_{K}, since the total energy must be conserved. Normally, the binding energy is measured relative to the Fermi level E_F. Hence, a correction for the work function ϕ is required when the total energy of the photoelectron is considered:

$$\hbar\omega = E_{\mathrm{B}} + \phi + E_{\mathrm{K}} \quad . \tag{3.7}$$

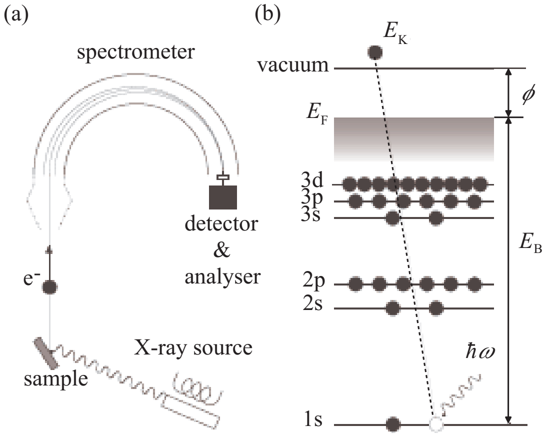

Figure 3.5: Illustration of the apparatus used in X-ray photoelectron spectroscopy (XPS) (a), and a schematic of the energy transition for XPS (b). The stoichiometry of sub - nm AlO_x *barriers is investigated using XPS measurements.*

The exact binding energy of a core electron depends on the chemical surrounding of the atom. If an atom forms chemical bonds with other atoms, a spacial redistribution of the valence electrons affects the potential of the core electrons resulting in a shift of the binding energy. Only photoelectrons that are ejected within the escape depth, a few nanometers below the surface, are able to escape from the sample in the direction of the spectrometer. The kinetic energy of the photoelectrons that arrive at the spectrometer varies due to the probability of scattering and energy loss. This introduces an energy dependent background on the intensity, referred to as Shirley background. The stoichiometry of a sample can be obtained by analyzing the kinetic energy spectrum. Therefore, the Shirley background is subtracted and, while taking the escape depth of the electrons into account, a standard Gauss+Lorentz curve fitting of the peaks is used to determine the peak positions and areas [68]. The peak positions give information about the chemical surrounding of atoms, and comparison of the area under the peaks reveals the concentration within the sample.

Chapter 4

Plasma Oxidation of Sub - nm Al_2O_3 Barriers

For Magnetic tunnel junctions (MTJs) with a surface area of less then 0.01 μm^2, the thickness of the Al_2O_3 barrier has to be typically thinner than a nanometer to ensure an appropriate tunnel current. If metallic Al is still present in the barrier, the spin-polarization of the current will be reduced [69]. On the other hand, if the bottom electrode is oxidized, the spins will be scattered by the ferromagnetic oxide that is formed. In both cases, the magnetoresistance of the MTJ decreases. Therefore, excellent control over the oxidation of sub - nm thin Al layers is of utmost importance.

In the previous chapter we described the *in situ* differential ellipsometer to study the plasma oxidation dynamics of an Al layer and the X-ray Photoelectron Spectroscopy (XPS) technique to determine the stoichiometry of a sample. In this chapter[1], we present *in situ* differential ellipsometry measurements, for studying the plasma oxidation dynamics of sub - nm Al layers. By analyzing the oxidation rate, we are able to mark the moment at which the over-oxidation of the Al_2O_3 barrier starts. To verify our conjecture, we have performed *in situ* X-ray Photoelectron Spectroscopy (XPS) measurements of identical samples. The results of these *in situ* ellipsometry and XPS measurements are subsequently discussed in the next sections.

4.1 Ellipsometry Measurements

To study the dynamics of sub - nm Al_2O_3 barriers with the the *in situ* differential ellipsometer, we used samples of the following composition: Si(001)/ SiO_x// 50 Å Ta/ 50 Å $Co_{90}Fe_{10}$/ d Al (with d ranging from 4 to 9 Å). Figure 4.1 shows the ellipsometry signal (ES) as a function of oxidation time for samples with Al layers ranging from 4 to 9 Å. At time $t = 0$ s the oxygen gas is let into the chamber. Within a few tenths of a second the ES rises distinctly, indicating a high initial oxidation rate. After a few seconds, the ES for the samples with Al layers ≤ 6 Å clearly show a point of inflection, indicating a change in the oxidation rate. This can be interpreted as the start of the CoFe oxidation, because the oxidation rate of a single layer decreases monotonously [70].

---

[1] Part of this chapter is published in Appl. Phys. Lett., **88**, 031909, (2006) and in J. Appl. Phys., **99**, 08T303, (2006)

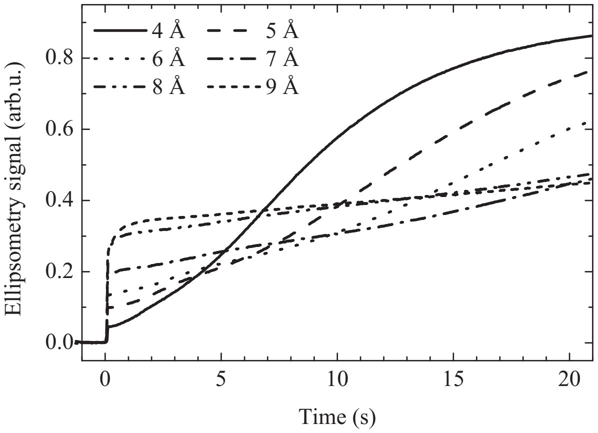

Figure 4.1: Ellipsometry measurements of the plasma oxidation for samples with 4 to 9 Å Al grown on 50 Å Ta/ 50 Å CoFe.

The changes in the oxidation rate can be studied in more detail by analyzing the derivative of the ES, because the ES is linearly proportional to the amount of oxidized metallic material. For the samples with Al layers ≤ 7 Å, the oxidation rate as monitored by the ellipsometry measurements, is shown in figure 4.2. The start-up phase, in which the gas is let into the chamber and the plasma is ignited, is not included in figure 4.2. In this phase, which lasts about 1.5 s, an instantaneous thermal oxidation of the Al surface and plasma stabilization takes place [71].

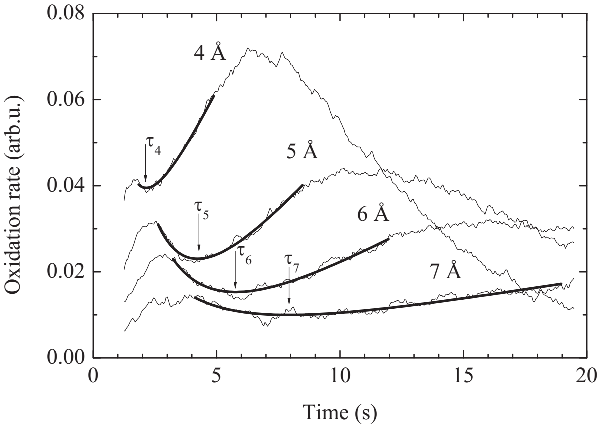

Figure 4.2: Oxidation rate of the samples with Al layers ≤ 7 Å on 50 Å Ta/ 50 Å $Co_{90}Fe_{10}$. The curves are polynomial fits used to determine the start of the CoFe oxidation $t = \tau_i$, with i an index number indicating the Al thickness in Å.

Kuiper *et al.* developed a model that distinguishes separate steps in the plasma oxidation of a thin Al layer. After instantaneous oxidation of the surface, oxygen diffuses through the Al grain boundaries to the CoFe/Al interface. When the oxygen has reached the interface, a conversion from substoichiometric AlO_x to stoichiometric Al_2O_3 takes place due to Al diffusion to the oxygen at the grain boundaries. After stoichiometric Al_2O_3 is formed, oxygen accumulates at the CoFe/Al interface and when there is an excess of oxygen, the CoFe starts to oxidize [72]. The features of the oxidation rate in figure 4.2 are analyzed in terms of this stepwise oxidation model.

Figure 4.2 shows that the overall oxidation rate is higher with decreasing Al thickness. This is likely due to variations in the morphology of such thin Al layers. As has been reported, the initial grain size depends on the deposited layer thickness [73]. Thinner layers have a higher density of grain boundaries due the the reduced grain size. Besides that, figure 4.2 shows that the oxidation rate of all samples initially increases. We tentatively explain this by heating of the top layers by the oxygen plasma, causing an increase of oxidation rate. Furthermore, the oxidation rate of all samples displays a maximum after a few seconds. We believe that, in accordance with the results by Kuiper *et al.*, the oxidation front has reached the CoFe/Al interface at that time.

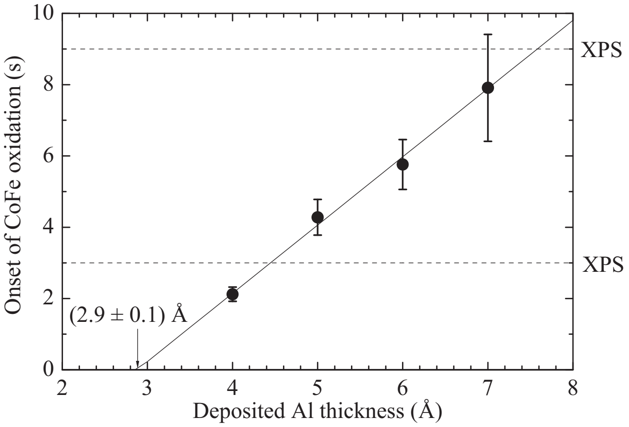

Figure 4.3: Onset of the CoFe oxidation as a function of the deposited Al thickness. The dashed lines indicate the times at which XPS measurements are performed.

Thereafter, the oxidation rate slows down until a minimum is reached at time $t = \tau_i$, with i an index number indicating the Al thickness in Å. During this phase, the AlO_x is supposed to convert to Al_2O_3. The oxidation rate increases again after time τ_i, as a signature of the CoFe oxidation. As a surprising feature, the apparent oxidation rate of the CoFe is found to be higher than that of Al for layers thinner than 6 Å. In contrast, our explicit modeling shows that the change in ES for Al oxidation is larger than that for Co oxidation, unless strong deviations of the refractive indices of the ultrathin films with respect to bulk values is assumed. Such deviations could indeed be expected for the sub-nm film, and non-continuous films [74]. Therefore, from the apparent higher oxidation rate we can deduce that depositing 4 or 5 Å Al is not sufficient to obtain a closed layer.

In figure 4.3 we plotted the onset of the CoFe oxidation, τ_i, as a function of the Al thickness. We concluded that the onset of CoFe oxidation is linearly proportional to the Al thickness and moreover that initially (2.9 ± 0.1) Å of the Al is already oxidized. Due to the oxygen background gas, this initial oxide is formed during the transportation to the oxidation chamber and the filling of the pre-volume with O_2 gas prior to the start of the measurement.

4.2 XPS Measurements

To investigate the conversion from substoichiometric AlO_x to stoichiometric Al_2O_3 barriers, and specifically examine the CoFe oxidation, we used *in situ* X-ray photoelectron spectroscopy (XPS) measurements. For the XPS measurements we used identical samples that were plasma oxidized for either 3 or 9 s. Within 10 minutes after the plasma oxidation, the chamber was pumped down to a base pressure of $< 10^{-9}$ mbar. Subsequently, the samples were transported to the connected XPS chamber.

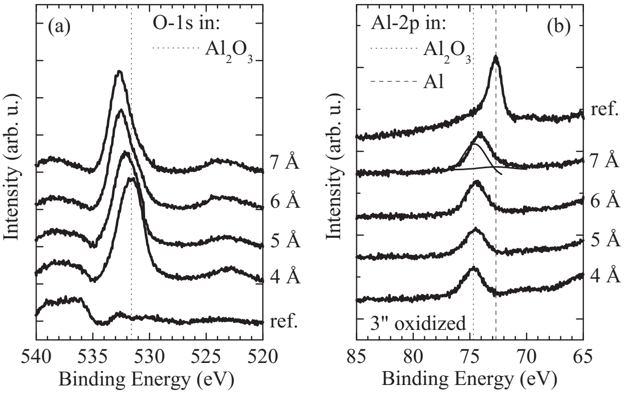

Figure 4.4: The O-1s (a) and Al-2p (b) XPS spectra for samples with 4 to 7 Å deposited Al after 3 s plasma oxidation. As a reference also the spectra of the unoxidized sample are plotted. The lines in the 7 Å Al spectrum are the fitting curves of the oxidic and metallic peaks, respectively.

Figure 4.4(a) shows the O-1s XPS spectra of the samples of 4 to 7 Å Al that were oxidized for 3 s. As a reference, the spectrum of a sample that was transported to the XPS chamber directly after growing the Al layer is also shown. This spectrum of the unoxidized sample shows virtually no trace of oxygen in the Al environment. In comparison to the unoxidized sample, the samples that were oxidized do show a peak indicating that the Al layer is oxidized. With decreasing thickness of the Al layer, the position of these peaks show a clear shift from higher to lower energy. The peak position of the sample with 4 Å Al is at the binding energy of the O-1s electron in stoichiometric Al_2O_3 (531.6 eV), indicated with the dotted line.

The Al-2p spectra of the samples of 4 to 7 Å Al are shown in figure 4.4(b). The reference spectrum of the unoxidized sample is also shown, the dashed line at the peak position indicates the binding energy of metallic Al (72.7 eV). Furthermore, a dotted line is drawn at the binding energy of the Al-2p electron in stoichiometric Al_2O_3 at 74.7 eV. The lines in the 7 Å Al spectrum are the fitting curves of the oxidic and metallic peaks, respectively. In comparison to the peak of the reference spectrum, all the Al-2p peaks in figure 4.4 are broadened. Furthermore, the peaks also show a clear shift towards the dotted line analogous to the O-1s peaks. For 4 Å Al the peak position coincides with the dotted line pointing out that stoichiometric Al_2O_3 is formed. We explain the gradual shift of the peak positions by the changing of the Al layer from AlO_x into stoichiometric Al_2O_3.

Figure 4.5 shows the spectra around the Co-$2p_{3/2}$ peak after 3 and 9 s plasma oxidation, as well as the reference spectrum of an unoxidized sample. The XPS spectra in figure 4.5(a) of the samples that were oxidized for 3 s show no clear shift of the Co-$2p_{3/2}$ peak in comparison to the reference spectrum. However, in the spectrum of the sample with 4 Å Al, the peak is asymmetrically broadened towards a higher binding energy [75], indicating that the CoFe oxidation has indeed started, in accordance with the ellipsometry data. Figure 4.5(b) shows the spectra of samples that were oxidized for 9 s. The spectrum of the 7 Å Al shows an asymmetrically broadened peak towards a higher binding energy. Furthermore, the spectra of the 4, 5 and 6 Å Al show a distinct double peak, indicating the progressive oxidation of the CoFe. This is confirmed by the appearance of a shake-up peak around 787 eV for the sample with 4 Å Al, and, although to a lesser degree, for the 5 Å Al. The shake-up peak, marked with an arrow, is attributed to the CoO. The fitting curves of the oxidic, metallic, and shake-up peaks are represented in the 4 Å Al spectrum.

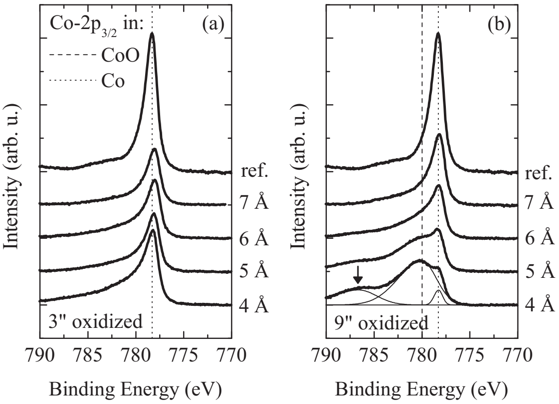

Figure 4.5: Co-$2p_{3/2}$ XPS spectra for samples with 4 to 7 Å deposited Al after 3 s (a) and 9 s (b) oxidation. As a reference also the spectrum of an unoxidized sample is plotted. The arrow indicates the position of the shake-up peak. The lines in the 4 Å Al spectrum are the fitting curves of the oxidic, metallic, and shake-up peaks, respectively.

To what extent this conversion to Al_2O_3 is completed can be determined from the ratio of the oxidic and metallic Al-2p peak areas in the spectra. Analogously, the amount of CoO can be determined from the ratio of the oxidic and metallic Co-$2p_{3/2}$ peak areas in the spectra. To obtain the peak areas, we subtracted a Shirley background, and, while taking the escape depth of the electrons into account, used a standard Gauss+Lorentz curve fitting of the peaks. Once we determined from the XPS data to which extent the Al is converted to Al_2O_3 and appointed the amount of CoO, the assumption that we are able to mark the moment at which the CoFe oxidation starts can be verified.

4.3 Discussion and Conclusion

In order to verify our assumption, we had to determine from the ellipsometry data the amount of Al, $\Delta_{\mathrm{Al},i}$, that was oxidized at $t = 3$ s, and compare that with the amount Δ_{τ_i} at τ_i. The amounts of oxidized Al, $\Delta_{\mathrm{Al},i}$ and Δ_{τ_i}, respectively, are determined by the change in the ES, I_i, between time $t = 3$ s and 0 s, and τ_i and $t = 0$ s, as shown in the inset of figure 4.6 for the 5 Å Al sample. The percentage of oxidized Al is defined as:

$$\frac{\Delta_{\mathrm{Al},i}}{\Delta_{\tau_i}} 100\% = \frac{I_i(t = 3\ s) - I_i(0\ s)}{I(\tau_i) - I_i(t = 0\ s)} 100\% \quad . \tag{4.1}$$

For the samples with 4 to 7 Å Al, the XPS data of 3 s oxidation and the ellipsometry data are shown in figure 4.6. A linear relationship through zero with slope 1 is expected between the amount of Al_2O_3 determined from the XPS data and the amount of Al that was oxidized from the ellipsometry data, and is indicated in figure 4.6. For the sample with 4 Å Al, XPS as well as the ellipsometry measurements showed complete oxidation of the barrier. The ellipsometry measurements underestimated the value of the 5 and 6 Å Al

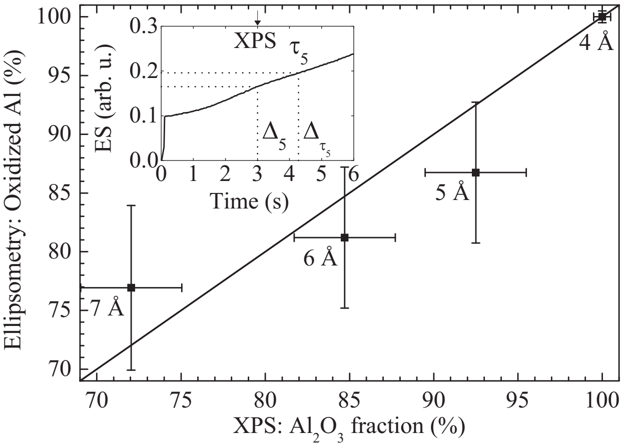

Figure 4.6: Percentage oxidized Al after 3 s of plasma oxidation, determined from the ellipsometry measurements, versus the percentage Al_2O_3 that was determined from the XPS data. The inset shows how the amounts oxidized Al, Δ_5 and Δ_{τ_5}, respectively, are determined from the ellipsometry measurements of the 5 Å Al sample.

data points. This deviation can be explained by an initial oxide, because an ellipsometry measurement only monitors the change in the amount of Al, whereas with XPS the total amount of Al that is still left is measured. This should also apply for the 7 Å Al sample, however, for this sample the value of the ellipsometry measurements is higher than that of the XPS. A reason for this can be the rather large uncertainty in the determination of the exact onset time τ_7. In addition, given the small slope of the ES for the 7 Å Al sample in figure 4.1, a slight inaccuracy in determining Δ_7 and Δ_{τ_7} can give a substantial error in the estimation of percentage oxidized Al.

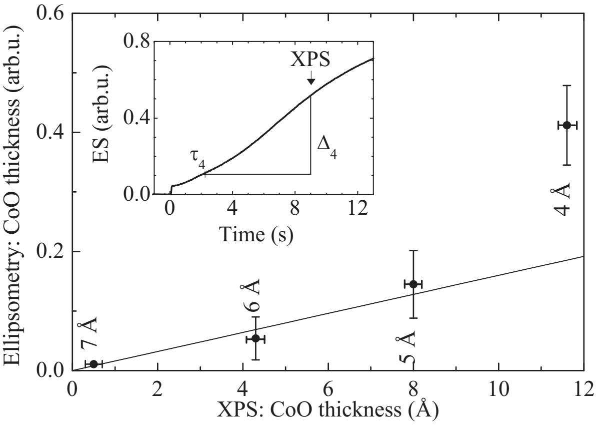

Figure 4.7: CoO thickness after 9 s oxidation, determined from the ellipsometry measurements, versus the amount of CoO that was determined from the XPS data of 9 s oxidation. The inset shows how the amount of CoO, Δ_4, is determined from the ellipsometry measurements of the 4 Å Al sample.

The amount of CoO from the ellipsometry data, $\Delta_{\mathrm{CoO},i}$, is determined by the difference in the ES at time $t = 9$ s and τ_i, as shown in the inset of figure 4.7 as shown for the 4 Å Al sample. For the samples with 4 to 7 Å Al, the XPS data of 9 s oxidation and the ellipsometry data are shown in figure 4.7. A linear relationship through zero is expected between the amount of CoO determined from the XPS data and the ellipsometry data. Except for the data point of 4 Å Al, the fit through zero displays a good linear relationship.

The deviation of the 4 Å Al data point from the fit cannot be explained by the initially oxidized Al of about 3 Å because it only generates an offset in the ES. The uncertainty in the thickness and morphology of the extremely thin Al layer is a more plausible reason, as separate samples had to be used for the ellipsometry and XPS measurements. Taking into account that the CoFe oxidation rate is strongly dependent on wether or not the Al_2O_3 layer forms a closed film, then even the slightest deviation in original Al thickness or morphology has a significant influence on the amount of CoO formed after 9 s. In addition, given the slope of the oxidation rate curve around 9 s for the 4 Å Al sample in figure 4.2, a slight inaccuracy in the onset time τ_4 can cause a substantial error in the estimation of the amount of CoO. This adds to the unreliability of the 4 Å data point.

Taking this into account, we conclude that the XPS and the ellipsometry data are in good agreement. Therefore, the conversion to stoichiometric Al_2O_3 and the over-oxidation of the sub - nm thin barriers for MTJs can be observed by recording the derivative of the ES. Furthermore, specific features in our ellipsometry traces confirmed the oxidation model proposed by Kuiper *et al.*. Accordingly, *in situ* real-time differential ellipsometry can be applied for monitoring the plasma oxidation dynamics in sub - nm Al layers and is potentially applicable as industrial process control.

Chapter 5

Nanofabrication of Magnetic Tunnel Junctions

The nanofabrication of magnetic tunnel junctions (MTJs) is a matter of designing the nanostructure and the production process. Furthermore, the nanofabrication concerns realizing the MTJ device in a sequence of alternating pattern definition and pattern transfer steps. As for the device design, the multilayer samples have no underlying complementary metal-oxide-semiconductor (CMOS) structure. Therefore, MTJs in a cross-point array architecture cannot be addressed individually when an electrical measurement is performed. To overcome this we have designed and fabricated two kinds of MTJ samples. Large arrays of nanoscale MTJs are used to characterize the magnetic properties by magnetometry. A stripeline of MTJ devices on a common bottom electrode is used for the individual electrical characterization by conductive atomic force microscopy (c-AFM). Regarding the realization of the MTJ devices, we use electron beam (EB) lithography to define the pattern in mask material and dry etching to transfer the pattern into the magnetic multilayers. A special high-speed EB writing strategy is developed to improve the throughput of patterning large area samples with ultra-dense arrays of sub - 100 nm features. With the EB writing strategy we are able to pattern a sample area of 16 mm^2 in 10 minutes with about 10^8 sub - 100 nm features.

5.1 Outline of the Fabrication Process

Section 3.1.1 describes the multilayer compositions of the magnetometry samples and the c-AFM samples to investigate the magnetic and electric properties, respectively. To prevent mask erosion during the deep Ar$^+$ ion beam milling of the arrays of nanoscale MTJs, we have used a hard Ta mask to fabricate the magnetometry samples. For the relative large bottom electrode of the c-AFM sample a fast etch process is used by applying a Cl$_2$-based plasma. Besides that, for the shallow etching of the free layer of the nanoscale MTJs, a non-corrosive CO/NH$_3$ plasma is applied. In this section the nanofabrication process of the samples is outlined.

The fabrication process of the magnetometry samples is schematically represented in figure 5.1. To define the mask pattern, a layer of negative tone hydrogen silsesquioxane (HSQ) resist is spin coated at 4000 rpm on the sample, baked at 120 °C for 4 minutes, and patterned by EB lithography. Next, the nanoscale pattern is transferred to the Ta capping layer using a low temperature SF_6/O_2 plasma. The etch depth has to be precise and reproducible to ensure that a thin Ta layer remains in the open areas to protect the MTJ material from oxidation. Finally, the large-area Ta nanoscale pattern is used to Ar^+ ion mill the nanoscale MTJs.

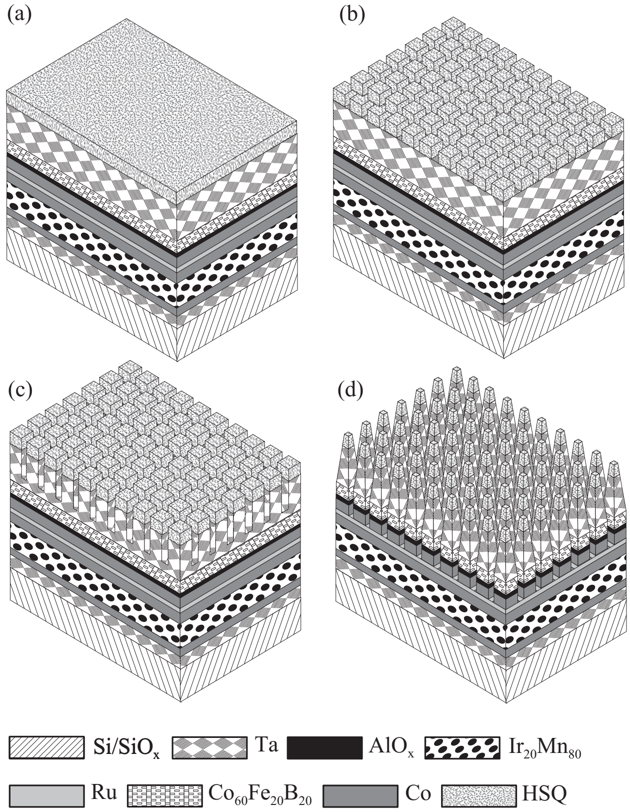

Figure 5.1: Schematic of the fabrication process of the magnetometry samples. After layer growth, a hydrogen silsesquioxane (HSQ) negative-tone resist layer that is spin coated on the sample is patterned by electron beam lithography (a). The HSQ is developed to define the mask with sub - 100 nm features (b). The Ta mask is etched at low temperature in a SF_6/O_2 plasma (c). The MTJ multilayer stack is structured by means of Ar^+ ion milling (d).

Figure 5.2 depicts the fabrication process of the c-AFM samples. A bilayer resist of polymethylmethacrylate (PMMA) with HSQ on top is patterned by EB lithography. After development of the HSQ, the PMMA layer is etched in a low pressure O_2 plasma. Next, the layout of the bottom electrode is etched in a high-ion density Cl_2-based plasma. Subsequently, the residual bilayer resist is dissolved in acetone due to PMMA underlayer and a new bilayer resist of PMMA and HSQ is spun on the sample. After patterning and developing the HSQ, the PMMA and Ta layers are etched to define the mask pattern.

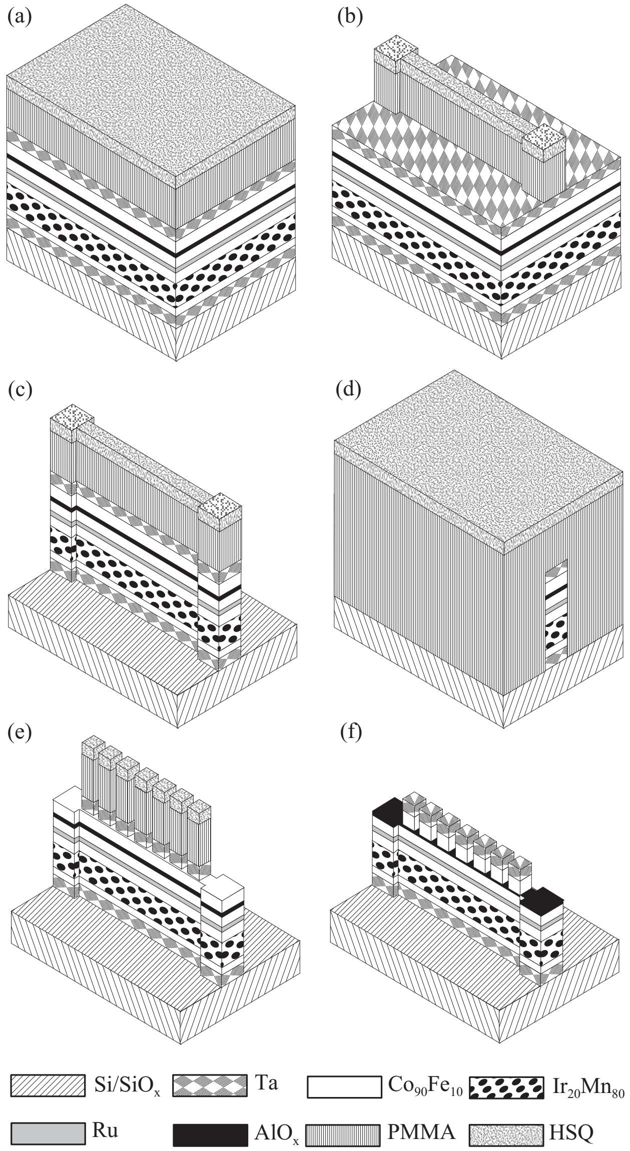

Figure 5.2: Schematic of the fabrication process of the conducting atomic force microscopy (c-AFM) samples. After layer growth, a bilayer resist of polymethylmethacrylate (PMMA) and hydrogen silsesquioxane (HSQ) that is spin coated on the sample is patterned by electron beam lithography (a). The HSQ is developed and the PMMA layer is etched in a low pressure O_2 *plasma (b). The MTJ multilayer stack is etched in a high-ion density* Cl_2*-based plasma (c). The old bilayer resist is dissolved in acetone and a new bilayer resist of PMMA and HSQ is spun on the sample (d). After patterning the HSQ, the PMMA and Ta layers are etched to define the mask (e). The free layer of the MTJ is etched in a* CO/NH_3 *plasma (f).*

Finally, the free layer of the MTJ stack is etched in a CO/NH_3 plasma, and the bilayer resist is dissolved in methylisobutylketon (MIBK).

In the next sections, we describe the EB lithography process to pattern the HSQ in more detail and the etch processes to define the Ta and bilayer resist mask structures. Furthermore, the different pattern transfer techniques for the multilayers are discussed.

5.2 High-Speed Electron Beam Lithography

The principle of EB lithography is the direct writing of a desired pattern in a thin resist layer with a focussed EB. We have used a Leica (Vistec) 5000^+ electron beam pattern generator (EBPG) system, equipped with a 100 kV field emission gun, to pattern an approximately 90 nm thick HSQ layer.

The conventional manner to write a pattern is by filling a feature with spot exposures in a pointillist style. The position of the EB is controlled by electromagnetic deflection coils that are shown in figure 5.3. A beam blanker is used for the on-off control of the EB during exposure. During the writing process intermediate calibrations are used to compensate for EB drift. After exposure of all the elements in one main field, the stage is moved to the next main field and all the elements of that field are successively exposed [76]. A typical spot diameter is 1.5 times the beam step size (BSS) and about $\frac{1}{4}$ of the minimum feature width, as can be seen in figure 5.4(a). Dense arrays are created by copying the feature in the x and y-direction.

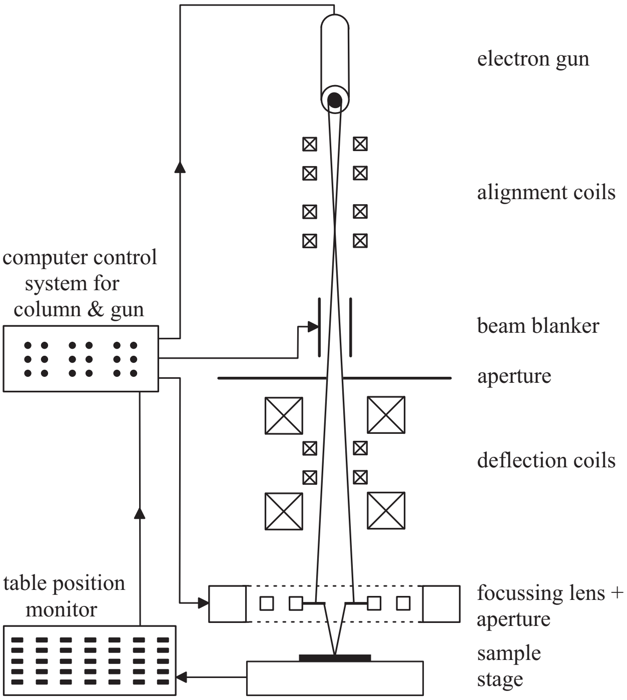

Figure 5.3: Schematic of the Leica (Vistec) 5000^+ electron beam pattern generator (EBPG) machine.

However, the EB needs a settling time of about 50 μs for every single feature. In this serial way of writing, the patterning of dense arrays of about 1.6 Gbits of sub-100 nm elliptical features will lead to an immense overhead time, resulting in a total writing time of approximately 1.5 hour. Consequently, the throughput is limited in comparison to other methods, such as interference lithography, in which exposure is a parallel writing process [77].

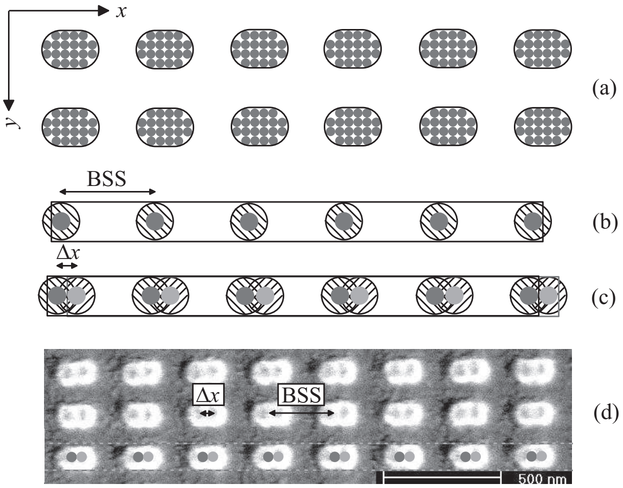

Figure 5.4: Conventional patterning occurs by filling the elliptical features in a pointillist style, using a spot diameter equal to 1.5 times the beam step size (BSS) and about $\frac{1}{4}$ of the feature width (a). With the high-speed EB writing strategy, a horizontal line is patterned with a spot diameter half the size of the desired width of the feature and a BSS equal to the pitch distance in the x-direction (b). After copying the line in the y-direction, a second line is patterned shifted a distance Δx from the origin (c). A scanning electron microscopy picture of an exposure dose test of 160 $\times$ 100 nm^2 elliptical features, defined with a spot of 41 nm, a BSS of 260 nm, and the shift Δx is 60 nm (d).

For large areas with ultra-dense arrays of sub-100 nm elliptical features, we developed a special high-speed EB writing strategy to improve the throughput. The strategy is depicted in figure 5.4(b) and 5.4(c). First, a horizontal line is patterned with a spot diameter half the size of the desired width of the feature, and a BSS equal to the pitch distance in the x-direction, as indicated in figure 5.4(b). This line is copied roughly 40,000 times in the y-direction. Accordingly, the EB needs only settling time between writing consecutive lines in the pattern. This leads to a relatively lower overall writing time, compared to the conventional manner to write a pattern.

Elliptical features are preferred regarding magnetic switching behavior [78]. To create elliptical features a second line is defined, which is shifted a distance Δx from the origin and patterned again, as is shown in figure 5.4(c). The shift Δx depends on the desired ratio of the feature. The accuracy in Δx is about 6 Å and corresponds to the laser interferometer control of the stage.

An exposed pattern element receives exposure not only from the incident beam but also from back scattered electrons, this is called proximity effect. Among other things, the effect is dependent on the EB accelerating voltage, resist material and thickness, substrate composition, and pattern packing density [79]. The conventional exposure dose is 400 to 500 μC/cm^2. However, as a result of the ultra-high pattern density and to correct for the proximity effect a reduced dose ranging from 60 to 100 μC/cm^2 is used in case of the high-speed EB writing strategy.

Following the electron-beam exposure, the HSQ is developed for 60 s in Shipley Microposit MF-322 developer. After that, the sample is rinsed for 15 s in a $1:9 =$ MF-322 : H_2O solution to prevent staining and for 15 s in H_2O to stop the developing process. Figure 5.4(d) shows a scanning electron microscopy (SEM) picture of an exposure dose test of 90 μC/cm^2 to pattern a sample with 160×100 nm^2 ellipses.

The sample surface is dark in the picture. The ellipses in the figure are the HSQ remains after development. The bright spots mainly at the edges of the features are due to charging of the HSQ resist under SEM inspection. The dark and light gray circles in the lowest line indicate the patterning spots that correspond to the spots in figure 5.4(c). The exposed regions shifted by Δx have merged and ellipses result, because of partial exposure overlap and proximity effects. Even though the elliptical features are nominally all identical, some structural variations occur, as shown in figure 5.4(d). The variations are due to the statistical characteristics of the lithography and development processes.

The elliptical features are defined with a spot of 41 nm, the BSS is 260 nm, and the shift Δx is 60 nm. A sample area of 16 mm^2 is patterned in 10 minutes with the high-speed EB writing strategy. With this patterning strategy, sub - 100 nm features can be defined at a pattern rate of approximately 1 cm^2/hour, as opposed to 0.6 mm^2/hour for the conventional patterning method. Therefore, large-area samples with ultra-dense arrays of sub - 100 nm elliptical features, can be written about 16 times faster using the high-speed EB writing strategy.

5.3 Mask Fabrication

After EB exposure and development of the hydrogen silsesquioxane (HSQ), the Ta and bilayer resist masks have to be structured. For the hard mask fabrication of the magnetometry samples the Ta layer must be etched to a precise and reproducible depth, to ensure that a thin Ta layer remains to protect the MTJ from oxidation. Therefore, we used a low temperature SF_6/O_2 plasma to etch the Ta. For the c-AFM samples, a bilayer resist of polymethylmethacrylate (PMMA) and HSQ is used, in order to be able to remove the resist after etching. To fabricate the bilayer resist, the sacrificial PMMA layer has to be etched in a low pressure O_2 plasma. Hereafter, we describe the mask fabrication processes in more detail.

5.3.1 Ta Etching in a Low Temperature SF_6/O_2 Plasma

A mask must be hard and the sidewalls have to be sufficiently steep, in order to transfer a pattern of nanoscale features. Matsui *et al.* used a 20 nm thick Ta etch mask to fabricate Magnetic Random Access Memories (MRAMs) elements [80]. Besides Ta, other materials like W or Ti are also suitable. However, Ta is normally used as capping layer to protect the MTJ multilayer stack from oxidation, and is therefore readily available. Moreover, the nanostructuring of Ta (and W) can be achieved in F-based plasma, while

Ti is more preferably etched with a Cl-based process with inherently more risk of corrosion.

Ta forms the volatile fluoride TaF_5 in a high density SF_6/O_2 plasma. Dry etching of Ta at ambient temperature in an inductively coupled (ICP) high density SF_6/O_2 plasma is studied as a function of SF_6/O_2 mixture, power and pressure by Hsiao *et al* [81]. To enable a more precise and reproducible etch depth control in the Ta mask structuring, we developed a low temperature process in an SF_6/O_2 plasma. All experiments are done in an Alcatel AMS 100 system, which is equipped with an ICP source. The chuck bias of the system can be controlled independently and the temperature can be varied from −150 °C to +20°. Figure 5.5 depicts a schematic of an ICP etching system.

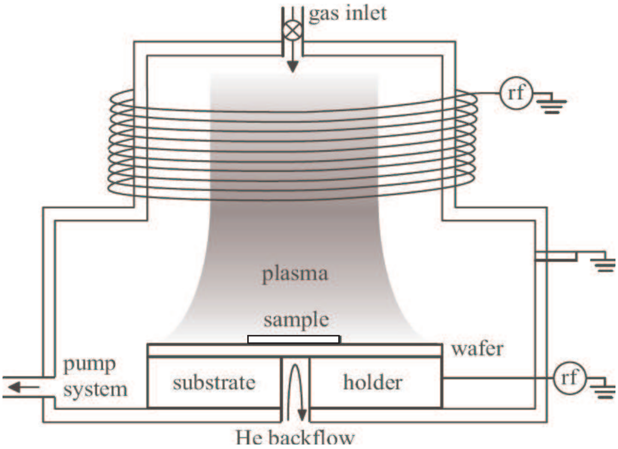

Figure 5.5: Illustration of the inductively coupled plasma (ICP) etching system.

The ICP 13.56 MHz *rf* power source is set at 1100 W and is applied to the antenna that is coiled around the cylindrical chamber with a pressure of 10 μbar. An oscillating electromagnetic field along the axis of the cylindrical chamber is generated by the *rf* current through the antenna. The magnetic field induces an azimuthal electric field that ionizes the SF_6/O_2 gas that is let into the chamber at flow rates of 300 sccm for SF_6, and 15 sccm for O_2. The charged particles revolve around due to the *dc* component of the magnetic field, confining the plasma and enhancing the probability of collisions. The energy transfer into the SF_6/O_2 ICP plasma is dominated by electrons, because electrons have a far smaller mass and are therefore accelerated to much higher velocities [82].

The plasma expands to the lower part of the vacuum chamber. A sample glued on a 4 inch wafer with thermal paste is located on a plate electrode. The chuck of the electrode is *dc* biased at −136 V by a separate *rf* source. The temperature of the carrier wafer is controlled by a combination of contant liquid nitrogen cooling and regulated resistive heating. He at the backside provides the thermal contact between the wafer and the substrate holder.

To obtain the precise and reproducible etch depth required, the etch rate must be as slow as possible, while still benefitting the synergy of a chemical component and ion bombardment. For the present work, we focussed therefore on finding the transient regime between ion-enhanced dry etching and physical sputtering by studying the temperature dependence of the dry etching process. In general, chemically excited processes are temperature dependent and can be described by the Arrhenius equation:

$$R(T) = A \exp\left(-\frac{E_a}{k_B T}\right) \quad , \tag{5.1}$$

with A the collisions frequency factor, E_a the activation energy of the process, and k_B the Boltzmann constant. To study the Ta etch rate as function of temperature we have used samples that consist of: Si(001)/ SiO$_x$// 900 Å Ta. Samples are marked with a resist pen and etched for increasing time intervals, from 10 s at −10 °C to 90 s at −80 °C. After rinsing off the resist marker with acetone and dipping the sample in isopropyl alcohol (IPA) to prevent staining, the etched depth is measured with an AFM.

The plot of the Ta etch rate as a function of the reciprocal temperature in figure 5.6, shows that the etch rate is following equation 5.1 down to a temperature of about −60 °C. The fit revealed an activation energy of (0.14 ± 0.02) eV. Below that temperature, the etch rate is no longer temperature dependent. Accordingly, the etch process only occurs by physical sputtering at a rate of approximately 5 Å/s. We selected a temperature of −50 °C for the Ta mask fabrication, in order to add a slight chemical component and diminish the redeposition while keeping nanometer control in the etch depth.

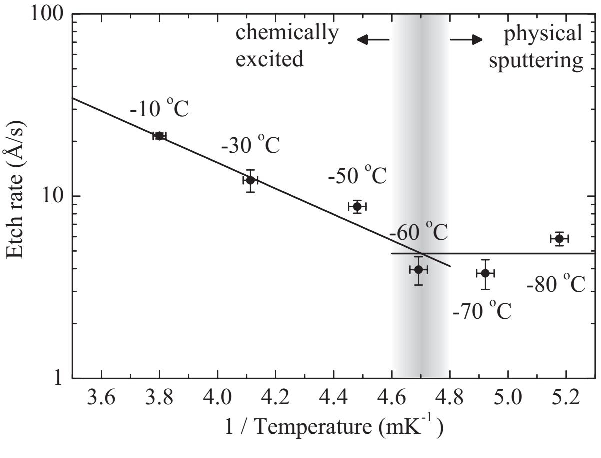

Figure 5.6: An Arrhenius plot of the Ta etch rate in a SF$_6$/O$_2$ plasma as function of the reciprocal temperature.

Subsequently using similar approach, with a resist pen marked 900 Å Ta samples are etched at −50 °C for various periods of time. In figure 5.7, the with an AFM measured etch depth is plotted as a function of time. The linear fit of the data yielded an etch rate of (8.2 ± 0.8) Å/s, with which the required precision is achieved.

Finally, the magnetometry samples with 150 Å Ta layer that are patterned with EB lithography, are etched in 16 s at −50 °C to create the mask of sub-100 nm features, as is shown in figure 5.1(c). AFM measurements showed repeatedly that the etch depth is (130 ± 8) Å, so that a protection layer of 2 Å Ta remained. Hence, the etch depth of a Ta mask can be controlled with nanometer precision.

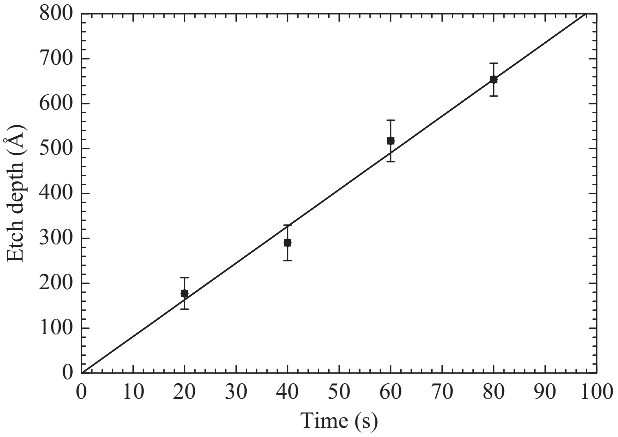

Figure 5.7: Graph of the Ta etch depth as function of the time at −50 °C.

5.3.2 PMMA Etching in an O_2 Reactive Ion Plasma

In order to be able to remove the resist after etching, we have used a bilayer resist mask of PMMA and HSQ for the c-AFM samples. Therefore, a layer of 2 % PMMA with a molecular weight of 950 k solved in traditional anisole is spin coated at 4000 rmp on the multilayer and baked at 175 °C for a hour. On top of the PMMA a HSQ resist layer is spin coated at 4000 rpm and baked at 120 °C for 4 minutes. After patterning and developing the HSQ layer, the about 200 nm thick sacrificial PMMA layer is etched in a low pressure O_2 reactive ion plasma at 4 μbar. In figure 5.8 a reactor is depicted which is suitable for reactive ion etching (RIE).

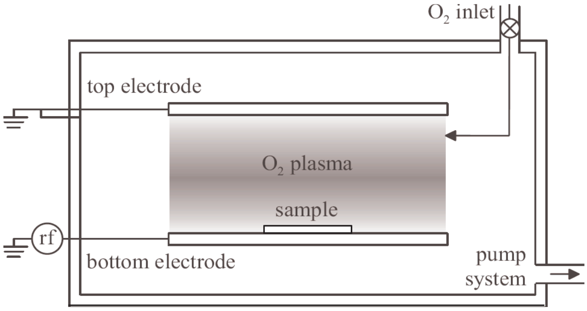

Figure 5.8: Schematic representation of the reactive ion etching (RIE) system.

An oscillating electric field is induced in the chamber by applying a 13.56 MHz *rf* power of 50 W to the electrically isolated bottom electrode, on which a sample is centrally placed. The electric field ionizes and dissociates the O_2 gas that flows into the chamber. Besides the O-radicals, the produced reactive O_2^+ ions play an important role in the etch process, because PMMA does not etch spontaneously. The O_2^+ ions are distributed from the bulk of the O_2 plasma to the sample. The ions are adsorbed on the surface and react chemically with the PMMA. The volatile chemical etch products are desorbed from the etching surface and are pumped out.

The bottom electrode acquires a *dc* bias voltage of about -180 V that accelerates the positive ions towards the sample and enhances the anisotropic etching process [83]. PMMA has an etch rate of approximately 92 nm/minute. The etch process is monitored with an interferometer, the process is finished when the derivative of the interferometer signal approaches zero.

5.4 Pattern Transfer Techniques

Nowadays, Ar^+ ion milling is a widely used pattern transfer technique for magnetic materials. However, the redeposition of backsputtered material on the sidewalls and a low etch rate are major drawbacks in patterning with this technique dense arrays of MTJs with a high throughput [84]. Jung *et al.* reported much higher etch rates of ≥ 50 Å/s for magnetic multilayer structures using high ion density Cl_2/Ar plasmas [85]. However, the chlorinated etch residues on the sidewalls of the etched features tend to severely corrode the magnetic material. In the following, we discuss several pattern transfer techniques that we used to fabricate the magnetometry and c-AFM samples.

5.4.1 Ar^+ Ion Milling

Ar^+ ion milling involves shadow masking to induce surface modification by sputtering away surface material. An Ar^+ ion beam can mill any combination of materials in a MTJ multilayer stack. The Ta capping material is quite useful also as mask material for ion milling, because of the relatively low sputter yield in comparison to the sputter yield of the MTJ materials. Therefore, Ar^+ ion milling is suitable for transferring the Ta masks pattern with the sub-100 nm elliptical features. A schematic representation of the milling machine that we used for milling the magnetometry samples, is shown in figure 5.9.

A hot-filament cathode located near the axis and a surrounding cylindrical anode provide an electric field to accelerate the electrons [87]. Ions are produced by the direct-current electron bombardment of the 0.35 μbar Ar gas in a discharge chamber. The Ar^+ ion are extracted through a screen grid and an acceleration grid to create a well-collimated Ar^+ ion beam.

The magnetometry sample is rotated for uniformity, during the Ar^+ ion milling at a voltage of 0.5 kV and an ion current of 0.19 mA/cm^2. When the beam of energetic Ar^+ ions collides with the surface, energy and momentum are transferred. To eject atoms from the surface the transferred energy has to exceed the chemical binding energy of the atom. Furthermore, the momentum conveyed to the sputtered atom has to be directed away from the sample surface [88].

The mill rate is strongly dependent on the angle α between the direction of the incoming Ar^+ ion beam and the normal to the surface. In figure 5.10 the mill rate of different materials is plotted as function of the beam incidence angle with respect to the surface normal, for Ar^+ ion milling at an acceleration voltage of 0.3 kV and a beam current

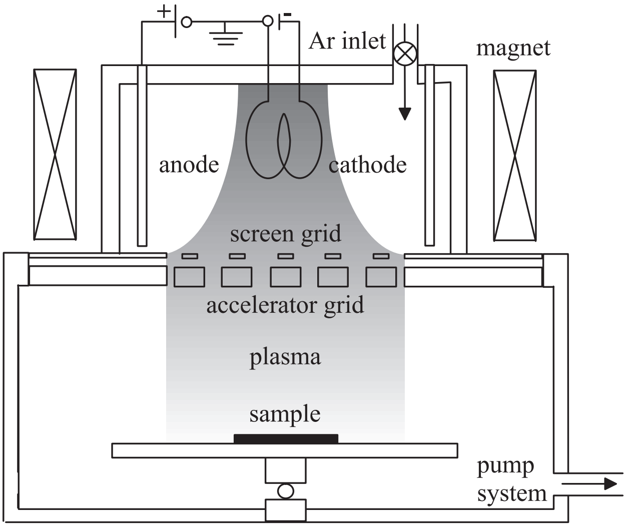
Ar inlet
magnet
anode
cathode
screen grid
accelerator grid
plasma
sample
pump
system

Figure 5.9: Representation of an Ar^+ ion beam milling machine.

of 0.32 mA/cm^2 [86]. Starting from normal incidence, the mill rate of most materials first increases, then reaches a maximum, and finally decreases as glancing angles are approached.

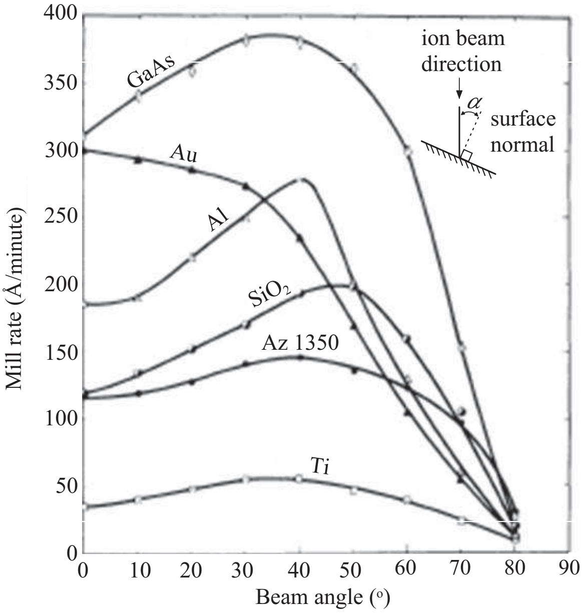

Figure 5.10: Ar^+ ion mill rates of different materials as function of the beam incidence angle with respect to the surface normal [86].

The angle dependency of Ar^+ ion milling can be used to reduce the redeposition of sputtered material around the edges of the structured MTJs. Therefore, after the regular 13 minutes of milling at 20°, the structuring process is concluded with 2 minutes milling at an angle of 75°. The schematic of the resulting magnetometry sample is depicted in figure 5.1(d), and figure 5.11 shows a scanning electron microscopy (SEM) image of an example of a dense array of Ar^+ ion milled 50×65 nm^2 MTJs that were patterned using the developed high-speed EB writing strategy.

The magnetometry samples are annealed at 300°C in a magnetic field for 5 minutes, the field is applied along the major axis of the MTJs and is also switched on during cooling to room temperature. After annealing the samples, the Magneto-Optical Kerr Effect (MOKE) technique is used to characterize the magnetic properties as function of the size and length to width aspect ratio.

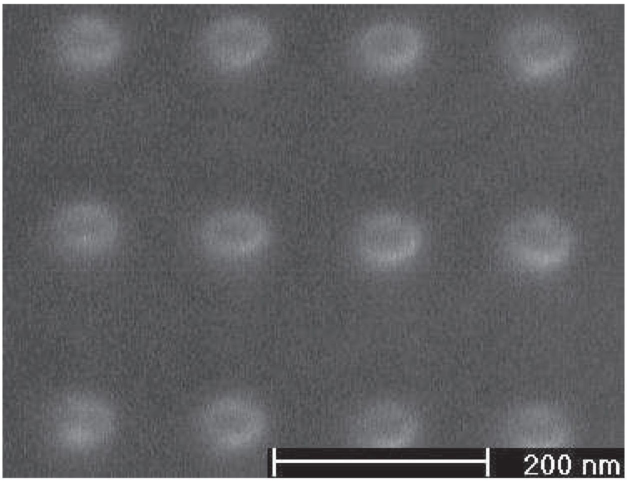

Figure 5.11: SEM images of a resulting magnetometry sample that was patterned with the high-speed EB writing strategy. After etching the hard Ta mask in a low temperature SF_6/O_2 plasma, the defined dense array of 50×65 nm^2 features is transferred using Ar^+ ion beam milling.

5.4.2 Inductively Coupled Cl_2-based Plasma

Opposite to the low Ar^+ ion milling rate, the pattern transfer in Cl_2-based plasmas has adequate etch rates. In inductively coupled (ICP) high ion density Cl_2/Ar plasmas at sample temperatures of ≤ 80 °C, etch rates of ≥ 50 Å/s are found for magnetic multilayer structures [85]. With increasing ICP source power the relatively low volatile chlorinated etch products are removed more efficiently by ion-assisted desorption. However, the etch rate reaches a maximum when an unbalance occurs between the formation of etch products and an efficient ion-assisted desorption [89].

A disadvantage of Cl_2-based plasmas is the inherently corrosive nature of the chlorinated etch residues on the sidewalls of the etched features. Nevertheless, corrosion of the magnetic material can be prevented by post-etch cleaning with H_2 or SF_6 plasmas or by H_2O rinsing [90]. Another drawback is the hindering of dry etching magnetic materials by the low volatility of the etch products. Therefore, etching $Co_{90}Fe_{10}$ in a Cl_2-based plasma at elevated temperatures is preferable, because the desorption of etch products is enhanced and the surface reactions are thermally activated [91]. Remains the problem that Fe is only etched by physical sputtering in a pure Cl_2 or Cl_2/Ar. To overcome this problem approximately 10 % BCl_3 is added to the gas mixture. The BCl_x or BCl_x^+ plasma species function as a catalyst for the etch process [92].

N_2 is added to the ultimate gas mixture, in order to form a thin passivation layer on the sidewalls of the etched features. Consequently, a high-ion density $Cl_2/BCl_3/N_2$ plasma is used for high-speed dry etching the bottom electrode in an Alcatel MET system [93], similar to that depicted in figure 5.5. The ICP source power is set at 1000 W and the rf chuck is biased at -100 V. The gas flows are set to 64 sccm for Cl_2, and 8 sccm for both BCl_3 and N_2. Finally, the bottom electrode of t he c-AFM sample is etched in 4 minutes at a pressure of 10 μbar and a temperature of 160 °C. The temperature is measured with a Luxtron fluoroptic probe, which is placed in the He-backflow, less than 1 mm from the wafer. Before being exposed to atmosphere, the samples are rinsed in H_2O in a N_2 dry box for 10 minutes, to remove the chlorinated etch residues from the sidewalls. Figure 5.2(c) shows the configuration of the c-AFM sample after etching the bottom electrode.

5.4.3 Noncorrosive CO/NH_3 Plasma

For the formation of the nanoscale MTJ devices that are shown in figure 5.2(f), a noncorrosive CO/NH_3 inductively coupled (ICP) process is used. For this purpose, a new bilayer resist mask of PMMA and HSQ is prepared, as is described in section 5.3.2. Next, using the method discussed in section 5.3.1, the full 5 nm Ta capping layer is structured at -50 °C in a SF_6/O_2 plasma. The resulting mask structure is depicted in figure 5.2(e).

In the search for noncorrosive gas mixtures for dry etching magnetic material, CO seemed to be a promising alternative, because of the formation of volatile carbonyl compounds. However, chemically assisted etching with CO resulted in reduced etch rates and increased redeposition, due to the formation of carbides on the sample surface [94]. Nakatani *et al.*, reported about etching Fe-Ni alloys at a rate of 350 Å/minute in a CO/NH_3 reactive ion plasma. The NH_3 in the gas mixture suppressed the dissociation of CO molecules, through which the formation of carbides is prevented [95]. The etch rate of NiFe and NiFeCo in a CO/NH_3 process was studied by Jung *et al.* [96]. The results revealed that the etch rate increased with ICP source power and substrate temperature. Furthermore, the rate showed an optimum as function of the CO versus NH_3 ratio. If the percentage CO is too high carbonaceous material is redeposited. A Fischer-Tropsch related processes underlies the etching of magnetic materials in CO/NH_3 plasma. In the Fischer-Tropsch processes, the CO and H in the plasma are converted into formamide ($HCONH_2$) in the presence of a Co, Fe or Ni catalyst, through the formation of volatile transition metal formamides instead of volatile carbonyls [97]. Therefore, the etch mechanism in a high density CO/NH_3 plasma still has a strong physical component, only because the sputtered magnetic material reacts with the CO redeposition is prevented.

The difference in the etch rates between the $Co_{90}Fe_{10}$ of the free layer and the AlOx of the barrier is not significant, due to this strong physical component. Accordingly, to determine the etch time of the 5 nm thick $Co_{90}Fe_{10}$, c-AFM multilayer samples that are marked with a resist pen are etched at a pressure of 10 μbar for various periods of time in a CO/NH_3 plasma. We used the Alcatel MET system with an ICP source to etch the free layer of the nanoscale MTJs in a high-ion density CO/NH_3 plasma. The values of the ICP source, the rf chuck power, and the temperature, are adjusted to the highest possible configuration of the system, namely, 1000 W, −200 V, and 200 °C, respectively. The CO : NH_3 ratio is varied to determine the optimale flow rates that appeared to be 15 sccm for CO and 35 sccm for NH_3. The etch depth is measured with AFM after removal of the resist marker. In figure 5.12 the etch depth is plotted as a function of time.

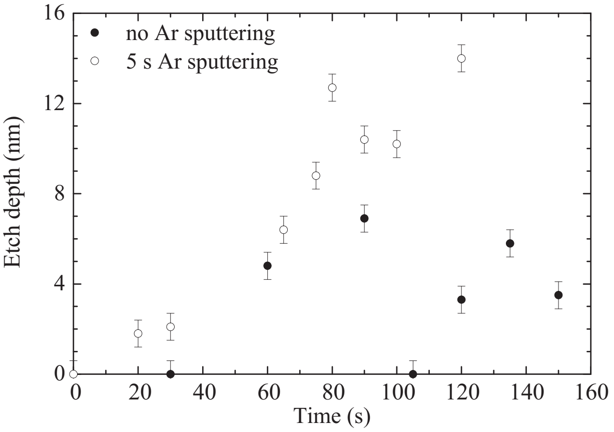

Figure 5.12: Graph of the etch depth as function of time for a c-AFM multilayer stack sample etched in a high-ion density CO/NH_3 plasma, in case the sample is not treated with a Ar plasma (●), and in case the sample is treated with 5 s of Ar plasma sputtering (○)

The data points that are represented with the black circle (●) are randomly scattered and show no trend. This can be explained by the formation of a native oxide layer in the 10 to 15 s that the sample is exposed to air during the transportation of the c-AFM sample from the Alcatel AMS 100 etcher to the the Alcatel MET system. To avoid the oxide problem, the c-AFM multilayer stack is first treated with an Ar plasma for 5 s, before repeating the experiment of the etch depth as a function of time. The flow rate of the Ar gas is set at 50 sccm and the configuration of the Alcatel MET system is the same as for the CO/NH_3 plasma. The results of the measured etch depth as a function of time when the sample is treated with an Ar plasma are plotted as open circles (○) in figure 5.12. Although, the trend is more distinct, still only a rough estimate for the etch time of the $Co_{90}Fe_{10}$ free layer can be given. However, taking sample to sample variation into account, a satisfactory success rate is feasible when three batches are etched in a CO/NH_3 plasma after a 5 s plasma treatment. Therefore, c-AFM samples are etched for 45, 60, and 75 s, respectively. After etching, the bilayer resist is removed by rinsing the sample in an ultrasonic batch for 2 minutes in methylisobutylketon (MIBK). A schematic of the resulting sample is shown in figure 5.2(f).

After annealing the samples at 300°C in a magnetic field along the major axis of the MTJs for 5 minutes, and cooling down to room temperature in a applied field, the samples are characterized by c-AFM.

Chapter 6

Magnetic Properties of Nanometer Scale Elements

In the previous chapter we described the fabrication procedure of large arrays of nanoscale MTJs, that were produced to investigate the magnetic properties. Nanofabrication concerns multiple delicate process steps and is therefore a challenging and time consuming procedure. Therefore, the spectrum of samples remained limited and the magnetic properties could only be investigated for a restricted number of parameters. In this chapter, we present the experiments and results of the investigation of the magnetic properties. To make this investigation more transparent, the introduction offers a step-by-step description of the subjects that will be discussed.

First, the magnetic characterization techniques are discussed that are used to measure the magnetic properties of the nanoscale elements analyzed in this Thesis. Therefore, we describe the Superconducting Quantum Interference Device (SQUID) magnetometer and the Magneto-Optical Kerr Effect (MOKE) magnetometer. Hereafter, we describe the samples under investigation and outline the experimental procedures to measure the magnetic properties. Next, the results of the magnetization reversal of arrays of Co dots as a function of the size and shape will be elaborated upon. Clear deviations of the Stoner-Wohlfarth behavior are observed and will be discussed in term of interdot coupling and edge roughness. Likewise, the magnetic switching behavior of arrays of sub - μm MTJs is discussed. We unambiguously demonstrate that the interdot coupling has a major influence on the magnetic switching behavior of ultra-high areal density arrays of nanoscale magnetic elements. In addition to the switching behavior, we also characterize the interlayer coupling effects of the sub - μm MTJs. Finally, a conclusion will be provided.

6.1 Magnetic Characterization Techniques

Normally, hysteresis loops of the magnetic moment as a function of an applied field are measured for the characterization of magnetic samples. In order to measure hysteresis loops, a variety of magnetometers are available. The two magnetometers used in this thesis are the SQUID magnetometer and the MOKE magnetometer. In the next sections, both magnetometers will be described in more detail. The specific application of the SQUID and MOKE magnetometer will be discussed in section 6.2.2

6.1.1 SQUID Magnetometer

In figure 6.1 a schematic representation is given of an rf-type SQUID magnetometer. With a SQUID magnetometer the magnitude of the magnetic moment can be determined quantitatively, so that the magnitude of the moment can be used as a control parameter for the indication of a successful nanofabrication proces. Therefore, the SQUID is used for measuring the switching of arrays of nanoscale Co dots. In order to perform a SQUID measurement, a magnetic sample is positioned in the center of a second order gradiometer. This gradiometer consists of two pairs of superconducting pick-up rings, which are wound end-to-end in such a manner that no net flux is induced by a magnetic field with a constant gradient [98].

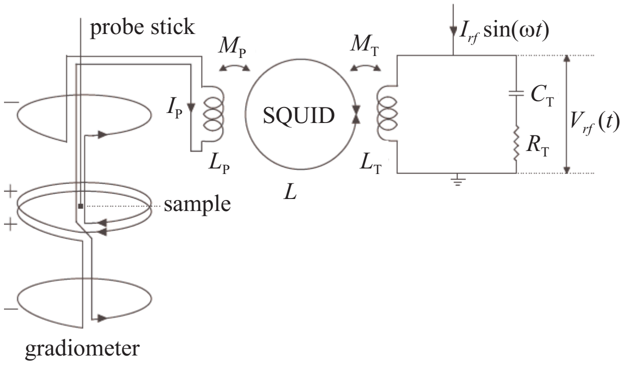

Figure 6.1: Schematic representation an rf-type SQUID magnetometer.

When the magnetic sample is moved through the gradiometer, a supercurrent I_P will flow through the pick-up rings to compensate for the flux originating from the sample, as a consequence of flux-quantization through superconducting rings. Via a coil with inductance L_P, this supercurrent is coupled to another superconducting loop with inductance L in which a single Josephson junction is inserted. This superconducting loop with the Josephson junction is in fact the SQUID [99]. Introducing the mutual inductance $M_P \propto \sqrt{L_P L}$, we can represent the proportionality of the external flux Φ_e through the SQUID and the supercurrent I_P as:

$$\Phi_e = M_P I_P \quad . \tag{6.1}$$

The flux Φ_e induces a circulating supercurrent I that is determined by the Josephson junction and opposes the external flux. Moreover, if we use the relation between the external flux and the phase difference over the Josephson junction, then the total flux Φ through the SQUID is given by [100]:

$$\Phi = \Phi_e - LI = \Phi_e - LI_c \sin\left(\frac{2e\Phi}{\hbar}\right) \quad , \tag{6.2}$$

with e the electron charge, $\hbar$ Planck's constant divided by 2π, and I_c the critical current for which a voltage appears across the Josephson junction. The SQUID is coupled by a mutual inductance M_T to a circuit of inductance L_T, capacitance C_T, and resistance R_T. The circuit is rf excited near the resonance frequency $\omega_0 = 1/\sqrt{L_T C_T}$ by a current

$I_{rf}\sin(\omega t)$. The coupling between the SQUID and circuit results in a voltage $V_{rf}(t)$ over the circuit, which is linearly proportional to the external flux Φ_e generated by the movement of the magnetic sample through the gradiometer [101].

6.1.2 MOKE Magnetometer

The magnetic switching behavior of arrays of sub-μm MTJs is examined with a MOKE magnetometer, because the magnetization can be measured locally with the MOKE technique. The MOKE technique exploits the change in optical polarization of light that is undergoing a reflection from a magnetic surface. Figure 6.2 depicts a home-built MOKE magnetometer that is used in the longitudinal configuration to investigate the switching of ultra-high areal density arrays with nanoscale MTJs of different sizes and aspect ratios.

Light from a 3 mW HeNe laser with a wavelength of $\lambda = 632.8$ nm passes through a lenses system, a polarizer and a photo-elastic modulator (PEM), which is operating at a frequency of 50 kHz. The modulation axis of the PEM is set at 45° relative to the linear polarization of the laser light. As a consequence, the light is modulated into alternating left- and right-handed circularly polarized light.

The laser light is focused on the sample with the lenses system to a spot diameter of about 50 μm, and is reflected from the surface. The complex Fresnel reflection coefficients for right circularly polarized light $\tilde{r}_+$ and left circularly polarized light $\tilde{r}_-$ described as [102]:

$$\tilde{r}_+ = r_+ \exp(i\phi_+) \qquad\qquad \tilde{r}_- = r_- \exp(i\phi_-) \quad , \tag{6.3}$$

with $r_\pm$ the amplitude, and $\phi_\pm$ the phase of the circularly polarized light. Linearly polarized light that is undergoing a reflection from the surface of a magnetic material is characterized by a change in the phase and the amplitude of the light. Linearly polarized light can be represented as a superposition of two circularly polarized components, of equal amplitude and opposite direction. A relative change in the phase of the two components

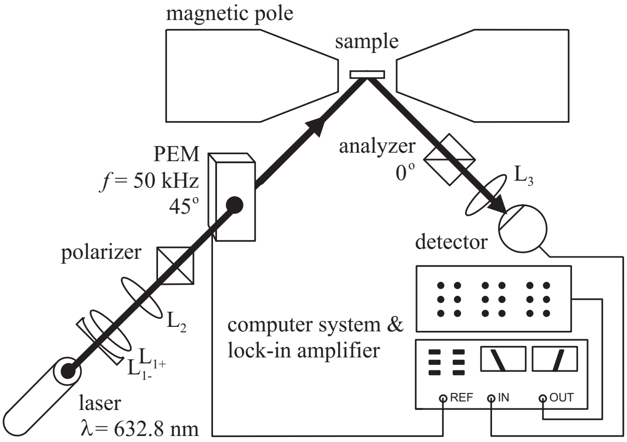

Figure 6.2: Home-built Magneto-Optical Kerr Effect (MOKE) magnetometer.

will leave their resultant linearly polarized, but rotated with respect to the original direction. This so called Kerr rotation can by formulated by:

$$\vartheta = \frac{1}{2}(\phi_+ - \phi_-) \quad . \tag{6.4}$$

Conversely, a relative change in the amplitude of the components will result in an elliptical superposition, since the magnitude of the sum varies and the line of the resultant rotates in time. This elliptical superposition, named Kerr ellipticity, can be defined as:

$$\varepsilon = \frac{r_+ - r_-}{r_+ + r_-} \quad . \tag{6.5}$$

The reflected light is led through an analyzer with the optical axis kept under an angle of 0° in reference to the initial polarization of the laser light. The laser light is detected with a silicon photodiode that is connected to a lock-in amplifier, which is receiving the reference signal from the PEM. A computer system records the output of the lock-in amplifier, which is proportional to the change in polarization of the reflected light from the surface that has to be analyzed. The Kerr rotation, which is typically a few mdeg, will induce a $2f$-modulation of the intensity, while Kerr ellipticity induces an f-modulation, with f the modulation frequency.

The hysteresis loops are measured with the MOKE magnetometer in the longitudinal configuration at room temperature. The maximum attainable field is approximately 400 kA/m and during the field sweep a Hall probe is used to measure the magnitude of the applied field.

6.2 Sample Description and Experimental Procedure

In chapter 1 we described the configuration of the magnetically engineered MTJ multilayer stack for MRAM application that we have studied in this Thesis. The top-down nanostructuring techniques used to fabricate large arrays of sub-μm MTJs for the characterization of the magnetic properties are discussed in chapter 5. In section 6.1 of this chapter, the SQUID and MOKE magnetic characterization techniques are explained. In the following, we give a description of the composition and the layout of the different samples that are investigated. Furthermore, information is provided about how the SQUID and MOKE techniques are utilized to characterize arrays of nanometer scale magnetic elements.

6.2.1 Composition and Layout of the Samples

The configuration of the magnetically engineered MTJ multilayer stack that are studied in this Thesis is depicted in figure 6.3(a). The MTJ multilayer stack that is built up of a buffer layer to promote smooth layer growth, an antiferromagnetic (AF) layer, an artificial antiferromagnet (AAF), and the actual MTJ that is comprised of a sandwich of the fixed layer of the AAF and a free ferromagnetic (FM) layer with an Al_2O_3 in between. The AAF that consists of a two identical FM layers separated by a Ru spacer. The bottom FM layer is pinned to the an adjacent AF layer. We have produced two different types of multilayer stacks, one for the the magnetic characterization and one to characterize the electrical properties. The compositions of the multilayer stacks are described in section 3.1.1.

With a nanofabrication procedure, including electron beam lithography and Ar^+ ion beam milling, large arrays of sub-μm MTJs are produced to investigate the magnetic

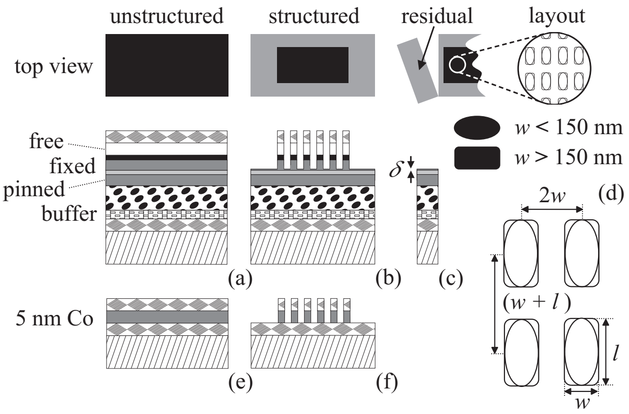

Figure 6.3: Schematic of the composition of the unstructured samples (a) and the layout of the structured samples (b). A residual sample consists of a cut off piece of a structured sample (c). The zoom-in of the area comprising arrays of nanoscale MTJ pillars shows the rounded rectangles and the elliptical shaped elements (d). Unstructured (e) and structured (f) 5 nm thick Co reference samples.

properties. The layout of the samples with large arrays of sub-μm MTJs is presented in figure 6.3(b). Only a part of about 16 mm^2 of the sample area contains on average approximately 10^8 MTJ pillars, which is indicated with a black rectangle in the top view of the sample. The gray part of the sample comprises the residual layers. Figure 6.3(c) shows a residual sample, which is a cut off piece of a structured sample.

The area indicated with a black rectangle contains arrays of nanoscale MTJ pillars with a width w ranging from 50 to 300 nm, and a length to width aspect ratios of 1.5 to 2.5. The zoom-in of figure 6.3(d) indicates the arrangement of the on average 10^8 MTJs. Figure 6.3(d) also shows a more detailed schematic of the MTJs location on a rectangular lattice with a spacing of $2w$ along the minor axis and $(l + w)$ along the major axis. The spacings are defined as the distance between the centers of the MTJs. The MTJs with a width $w > 150$ nm are rounded rectangles and the MTJs width $w < 150$ nm have an elliptical shape, as shown in figure 6.3(d). The elliptical MTJs are patterned with the high-speed electron beam writing strategy, and the rectangular MTJs are patterned in a

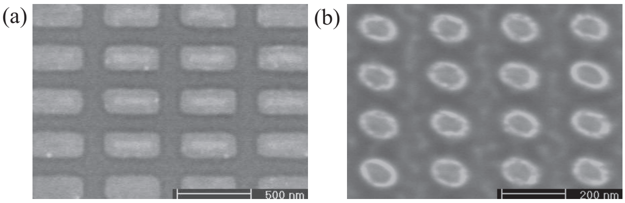

Figure 6.4: SEM images of 160 $\times$ 360 nm^2 rounded rectangles as an example of the rectangular dots (a), and an example of 80 $\times$ 140 nm^2 elliptical shapes.

conventional manner. In addition, figure 6.4 shows scanning electron microscopy (SEM) images as examples of the rectangular and elliptical MTJs, respectively.

We have also studied the switching behavior of arrays with 5 nm thick polycrystalline Co dots, in order to disentangle the geometry effects from the coupling effects on the switching of the free layer of the MTJ. The layout of the Co dot samples is the same as that of the samples with arrays of sub - μm MTJs, as can be seen in figure 6.3(e) and (f).

6.2.2 Application of Magnetometry Measurements

The SQUID magnetometer and the MOKE techniques are used to measure the magnetic properties of the nanoscale elements characterized in this Thesis. The SQUID magnetometer is suitable for a quantitative determination of the magnetic moment of a sample as a function of an applied magnetic field and temperature. In contrast to the SQUID magnetometer, obtaining quantitative information on the magnitude of the magnetization is not possible with the MOKE technique. However, the MOKE technique is particularly useful for measuring the magnetization of a sample locally. This section provides insight into the utilization of the typical characteristics of the SQUID and MOKE technique for measuring the nanoscale magnetic elements.

The demands on stable magnetic switching behavior of sub - μm MTJs require a magnetically engineered multilayer stack. The multilayer stack is a complex magnetic system, due to the different interlayer coupling phenomena. Therefore, understanding of the switching behavior of the unstructured multilayer stack is important. For the application of MTJs as memory cells, it is essential to comprehend the difference beween the effect of the interlayer coupling and the coupling due to the stray fields fringing from the nanoscale magnetic elements. In order to analyze the pure interlayer coupling, SQUID measurements are performed of an unstructured samples, like depicted in figure 6.3(a).

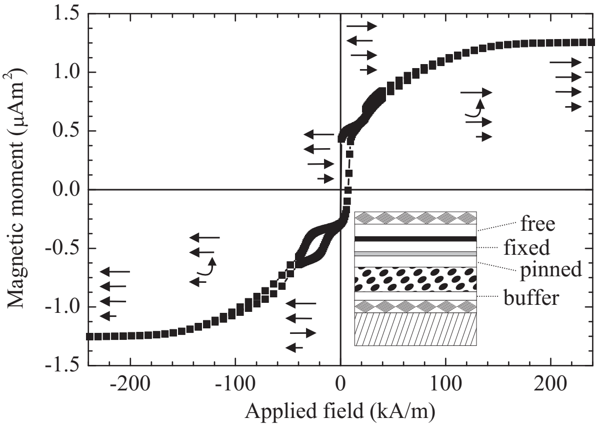

Figure 6.5: A graph of a SQUID measurement of an unstructured MTJ multilayer sample. The arrows indicate the switching of the four magnetic layers that are colored white in the schematic of the sample.

Figure 6.5 shows a graph of a typical SQUID measurement of an unstructured sample.

The hysteresis loop exhibits the characteristics corresponding to a typical magnetically engineered MTJ stack, which are described in literature [103]. The arrows indicate the switching of the four magnetic layers that are colored white in the schematic of the sample. The magnetic moments are saturated at a high positive field. When the applied field is reduced, the magnetic moments of the fixed layer start to rotate at about 160 kA/m. At approximately 20 kA/m the plateau with an antiparallel alignment of the artificial antiferromagnet is reached. The free layer switches around zero field and the switch of the buffer layer is observed at approximately -35 kA/m. Finally, also all the magnetic moments of the pinned layer have rotated before the sample is saturated in the negative direction.

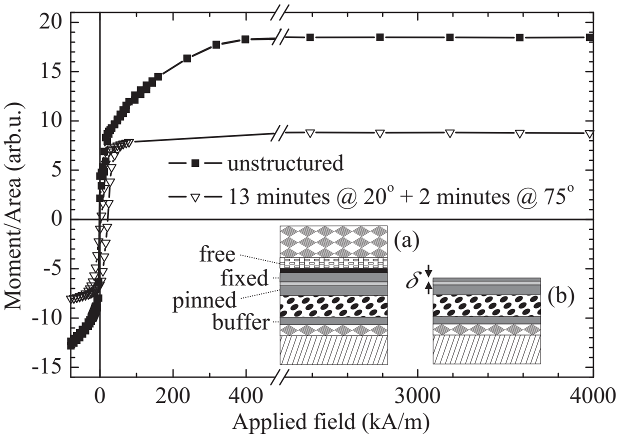

Figure 6.6: SQUID measurements of an unstructured magnetometry MTJ multilayer sample (a) and a residual sample (b) to determine the Ar^+ ion milling depth.

With the SQUID magnetometer the magnetic moment of the entire sample is measured. Accordingly, both the residual layers and the MTJ pillars, which are presented in figure 6.3(b), contribute to the SQUID output signal. However, we are interested in the magnetic switching behavior of the free layer of the sub-μm MTJs. The contribution of the background signal due to the residual layers could not be determined properly, because the Ar^+ ion milling depth could not exactly be resolved with AFM measurements, due to resist remains. Therefore, we measured the magnetic moment of a cut off piece of a structured sample displayed in 6.3(c), in order to judge if the magnetic contribution of the sub-μm MTJ pillars could be extracted from the magnetic contribution of the residual layers.

In order to determine the depth after 15 minutes of Ar^+ ion milling, in figure 6.6 the SQUID measurement of an unstructured sample, which is shown in inset (a), is compared with that of a residual sample that is illustrated in inset (b). The magnetic moments are scaled to the sample areas. SQUID measurements revealed values for the saturation magnetization of the free $Co_{60}Fe_{20}B_{20}$ layer, $M_{\mathrm{CoFeB}} = 1324$ kA/m, and the Co buffer and AAF layers, $M_{\mathrm{Co}} = 1129$ kA/m. The difference in the measured magnetic moment per areas between of the unstructured and the residual sample, indicated that the milling was terminated in the fixed layer. Inset (b) of Figure 6.6 specifies the thickness δ of the remaining fixed layer that is expected to be only a few nanometers.

X-ray photoelectron spectroscopy (XPS) measurements of the Ru-3d$_{5/2}$ spectrum of the residual sample displayed a peak at the binding energy of Ru (280.2 eV), confirming that the Ar^{+} ion milling was terminated in the fixed layer.

Due to the magnetic moment of the residual layers, it is difficult to unravel the magnetic switching behavior of the sub - μm MTJs. Therefore, the MOKE technique is used to locally probe the magnetic properties of the residual layers and the part containing the MTJ pillars. Figure 6.7 shows an example of the measured Kerr rotation versus applied field loop of a sample with MTJs with a surface area of 60×100 nm^2.

The top graph of figure 6.7 shows the measurement with the laser spot focussed on the part containing the MTJ pillars, which is schematically presented as a white circle on the black rectangle. The field is applied along the major axis of the MTJs. As expected, the coercive field $H_c = 9$ kA/m is increased in comparison to the coercive field of the unstructured sample (≤ 1 kA/m).

To distinguish between the magnetic properties of the nanoscale MTJs and of the residual layers, also a hysteresis loop is measured with the laser spot focussed on the residual part of the sample, indicated with a white circle on the gray rectangle. The measurement is plotted in the bottom graph and shows only the exchange biased switch of the buffer layer. By comparing the loop corresponding to the MTJ pillars with the loop of the residual layers, the magnetic properties of the arrays of sub - μm MTJs can be

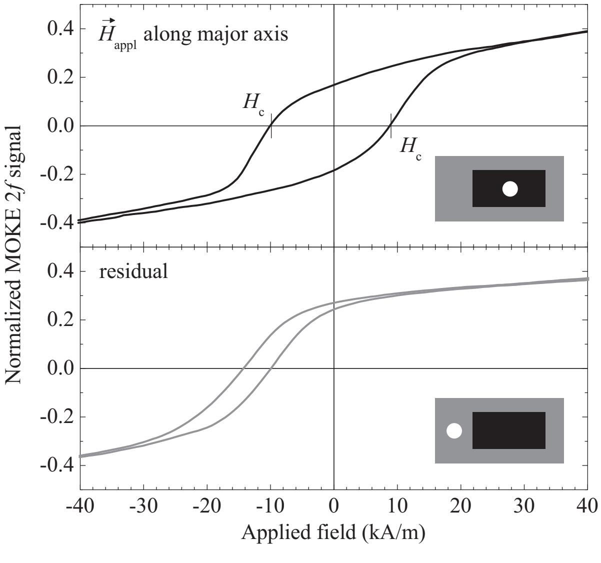

Figure 6.7: MOKE measurements of a sample with a patterned part consisting of an array of MTJs with a surface area of 60×100 nm^2. The top graph shows the measurement with the laser spot focussed on the patterned part, which is schematically presented as a white circle on the black rectangle. The measurement with the laser spot focussed on the residual part of the sample, indicated with a white circle on the gray, is plotted in the bottom graph.

disentangled from the contribution of the signal due to the residual layers.

6.3 Magnetization Reversal of Arrays of Co Dots

After covering the experimental procedures in more detail, and highlighting the problems of characterizing the samples with nanoscale magnetic elements, we present a selection of SQUID measurements that are used to investigate the switching of arrays of 5 nm thick polycrystalline Co dots. The analysis of the switching of the Co dots contributes to a better understanding of the effect of the geometry and interlayer coupling on the switching behavior of the arrays of sub - μm MTJs.

6.3.1 Overview of the SQUID Measurements

The investigated arrays consist on average 10^8 polycrystalline Co dots with a width w ranging from 50 to 300 nm, and a length to width aspect ratios of 1.5 to 2.5. The composition of the samples is depicted in figure 6.3(f). The dots are arranged on a rectangular lattice according to the layout schematically shown in figure 6.3(d).

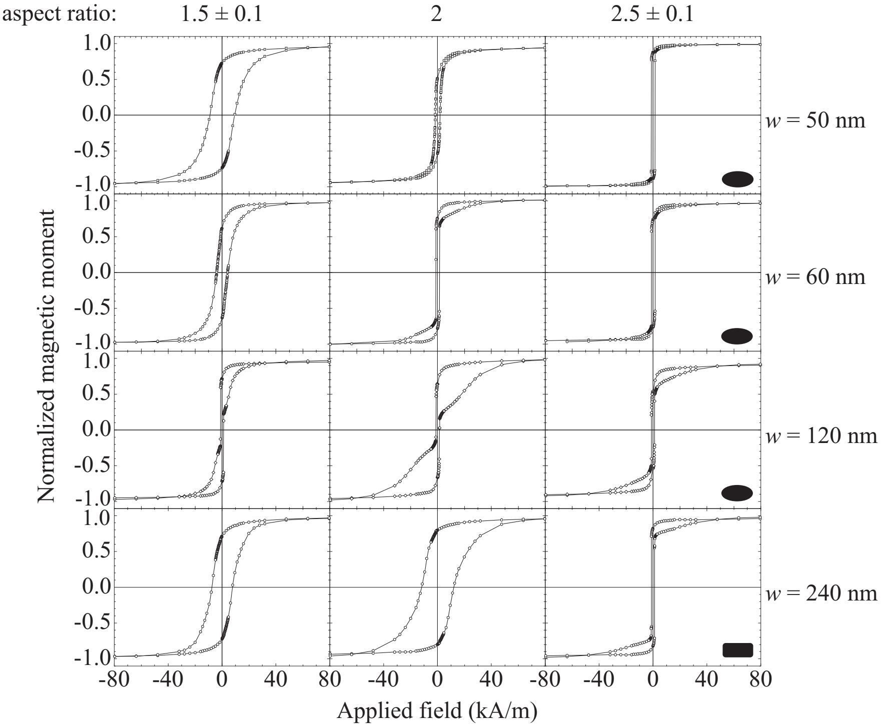

Figure 6.8: Overview of the SQUID measurements of arrays of elliptical and rectangular Co dots of different sizes and length to width aspect ratios.

Figure 6.8 shows an overview of the SQUID measurements performed to examine the magnetization reversal of the nanoscale Co dots as a function of the size and shape. In the overview of figure 6.8 hysteresis loops are shown of arrays of elliptical and rectangular Co dots of different sizes and length to width aspect ratios. All the loops are measured with the field applied in-plane along the major axis of the dots. The various hysteresis loops have different shapes and the overview does not demonstrate a distinct dominant trend. Nevertheless, figure 6.8 displays some interesting aspects that are worthwhile considering in more detail. For example, what is the reason behind the difference in shape of the hysteresis loops. Furthermore, which factors influence the magnetization reversal processes, can we understand the reduction of the switching field, and what is the effect of the geometry of the nanoscale Co dots.

In the following, aspects as the shape of the hysteresis loops, mechanisms that contribute to the magnetization reversal processes, and the geometry effect on the switching behavior will be examined in more detail, in order to get a better understanding of the complex magnetization reversal processes.

6.3.2 Shape of the Hysteresis Loops

For 5 nm thin polycrystalline Co dots the magnetization is assumed not to vary throughout the thickness direction. Furthermore, the Co dots are approximated by a flat ellipsoid and the magnetization is constrained to rotate in plane of the film during reversal. The Stoner-Wohlfarth model that is described in section 2.2, is generally used in literature to describe the magnetization reversal processes of thin nanoscale magnetic elements. The magnetization as function of an applied field along the major axis of the element will exhibit a rectangular hysteresis loop, according to the Stoner-Wohlfarth model.

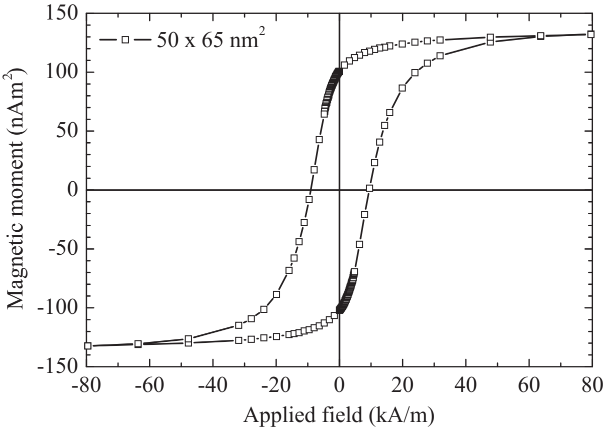

Figure 6.9: Hysteresis loop of array of 50×65 nm^2 Co dots.

The bottom-left, the middle-left, and the bottom-middle hysteresis loops of figure 6.8 have rounded rectangular shape like the hysteresis loop depicted in figure 6.9. The common property of those Co dots is that the length to width aspect ratio is ≤ 2. The loop in figure 6.9 of an array of 50×65 nm^2 elliptical Co dots, shows that the coercive field is increased to approximately 9 kA/m, in comparison to the measured coercive field of an unstructured sample of about 1 kA/m. Although the remanence of the 50×65 nm^2 Co dots is only about 77 %, the rectangular hysteresis loop could be an indication of a Stoner-Wohlfarth resembling switching behavior, presuming that the rounding of the hysteresis loop is caused by a distribution of switching field due to early switching of individual Co dots, the early switching can be a consequence of a higher effective field that the dots experience as a consequence of the additional interdot field, described in section 2.3.2. We relate the early switching to the interdot field, because the conducted OOMMF simulation of the switching of a single dot revealed a remanence of 100 %. The lower remanence of the experimental data indicates that part of the dots of the array already switched the magnetization before zero field.

On the other hand, the rounding of the hysteresis loop could also be an indication for a magnetization reversal according to the Buckling mode. Starting from high applied magnetic field, during reversal in the Buckling mode the magnetic moments relax causing a rounding of the hysteresis loop. Under a reversed field, the relaxation of the moments continues, until the Buckling instability occurs and a sharp switch can be observed. Perhaps due to the distribution of switching field of individual Co dots, figure 6.9 does not show a sharp switch. Therefore, relating the shape of the hysteresis loop to a magnetization reversal corresponding to the Buckling mode is also possible. However, because figure 6.9 displays the collective switching behavior of the array of Co dots, no decisive demonstration could be given for the mode of magnetization reversal.

Figure 6.8 shows that not all the hysteresis loops of the nanoscale Co dots have a shape like the loop depicted in figure 6.9. The shape of the hysteresis loops in figure 6.10 is similar to the shape of the top-left and the top-middle loops of the Co dots that also have an aspect ratio of ≤ 2. Figure 6.10 displays the hysteresis loops of arrays of Co dots width lateral dimensions of 120×160 nm^2 and 160×320 nm^2. Both these hysteresis loops of the 120×160 nm^2 and 160×320 nm^2 Co dots show that the magnetic moments already begin to rotate at about 20 kA/m. At zero field, the 120×160 nm^2 dots have a remanence of 71 %, whereas the 160×320 nm^2 dots have a remanence of 66 %. The outcome for the remanence of OOMMF simulation was 99 % for the 120×160 nm^2 dots and 90 % for

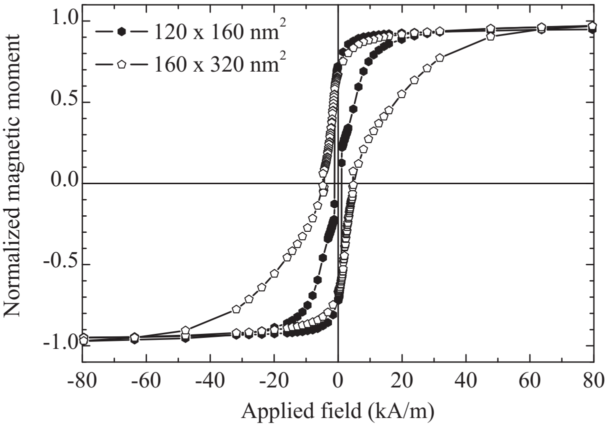

Figure 6.10: Hysteresis loops of array of elliptical Co dots with dimensions of 120×160 nm^2 and 160×320 nm^2.

the 160×320 nm^2. Therefore, we once more state that the early switching of individual Co dots is due to an additional interdot field, and we emphasize the large influence of the interdot field on the magnetic switching behavior of ultra-high areal density arrays.

The hysteresis loops of the 120×160 nm^2 and 160×320 nm^2 Co dots are dented in the middle as is illustrated in figure 6.10. At approximately -1 kA/m part of the array of the 120×160 nm^2 Co dots switches the magnetization, while the magnetic moments of the array of the 160×320 nm^2 dots are assumed to still reverse by rotation. Just before reaching zero magnetization, at about -4.5 kA/m, a few 160×320 nm^2 dots of the array switch the magnetization. After the switch, the dots of both samples proceed to reorientate the magnetic moments along the applied magnetic field until the sample is saturated. The sudden simultaneous switching of part of the array could indicate a Buckling instability inducing the reversal mode schematically depicted in figure 2.6.

Hysteresis loops comparable to the shapes shown in figure 6.10 resulted from an investigation of the switching behavior of individual Co particles [104]. Wernsdorfer *et al.* proposed an interpretation to explain the characteristics of the shape of the hysteresis loop and suggested that the magnetization reversal is occurring by incoherent rotation. Figure 6.11 shows a schematic of the proposed magnetization reversal, which is not consistent with figure 2.6. Therefore, the magnetization reversal is not according to the Buckling mode.

Nevertheless, the shapes of the loops in figure 6.10 can be interpreted as follows. Starting from a saturated state, magnetization reversal begins with the formation of transversely magnetized edge domains which are gradually growing. The edge domains structure at zero field, is based on micromagnetic principles that was introduced by Van den Berg [105]. After reversing the field a domain wall nucleates and divides the Co dot into two equal domains, which is illustrated in figure 6.11(a). Figure 6.11(b) shows that when the field is further reduced the domain wall is pushed to the border of the dot. Finally, the domain wall annihilates and the dot becomes single domain again, as can be seen in figure 6.11(c).

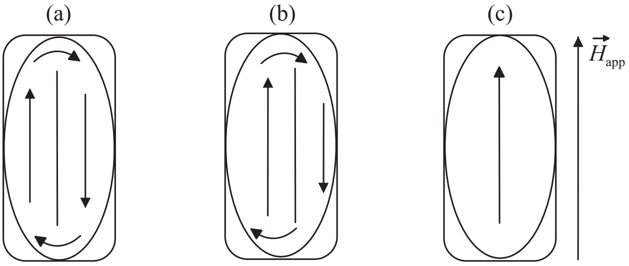

Figure 6.11: Schematic of the magnetization reversal that starts with the nucleation of transversely magnetized edge domains and the formation of a domain wall when the applied field is reversed (a). The magnetization reversal proceeds by pushing the domain wall to the border of the dot (b). The reversal ends with annihilation of the domain wall and saturation of the dot (c).

By analyzing the different hysteresis loop shapes we tried to account for the mode of magnetization reversal of the nanoscale Co dots. By comparing OOMMF remanence data with the experimental data, we were able to unambiguously relate the early switching of the individual Co dots to the interdot field. Nevertheless, due to the contribution of the interdot field, no conclusive reversal mode of the Co dots could be given. To get a better understanding of the reversal, below the factors that contribute to the magnetization reversal processes will be examined.

6.3.3 Contributions to the Magnetization Reversal Process

As discussed in section 6.3.2, most of the hysteresis loops of Co dots with an aspect ratio of 1.5 displayed a rectangular shape, indicating a Stoner-Wohlfarth resembling magnetization reversal or switching by the Buckling reversal mode. Although the Stoner-Wohlfarth model gives an overestimation of the switching fields [46], the model can be used to estimate the values of the coercive fields. Therefore, the thickness of the Co dots is taking as the third axis of the ellipsoid and the demagnetization factors are determined with figure 2.3. Furthermore, the crystalline anisotropy is neglected supposing no average anisotropy for polycrystalline Co. Instead of the bulk value, the measured saturation magnetization of Co is used for calculating the Stoner-Wohlfarth switching fields.

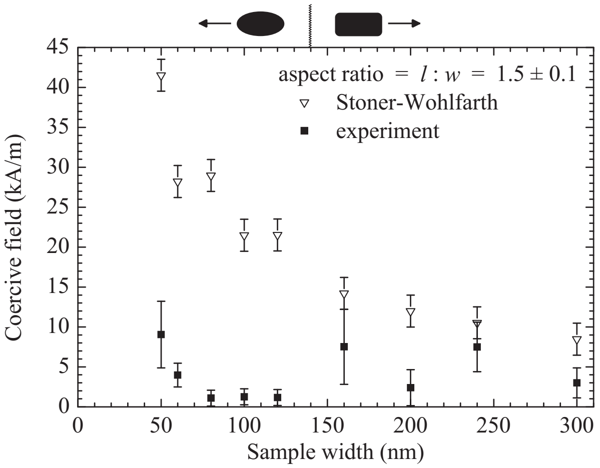

Figure 6.12: Plot of the calculated Stoner-Wohlfarth switching fields and the experimental data of Co dots with a width ranging from 50 to 300 nm, and a length to width aspect ratios of about 1.5.

The calculated Stoner-Wohlfarth switching fields are compared with the experimental results of dots with a width w ranging from 50 to 300 nm, and a length to width aspect ratio of about 1.5 in figure 6.12. The experimental data are lower than the calculated switching fields. This is anticipated, because the Stoner-Wohlfarth model gives an upper bound. However, the measured value of the 50×65 nm^2 Co dots is only 20 % of the calculated Stoner-Wohlfarth switching field. The Buckling instability mode is proved to be the easiest nucleation mode [45]. Therefore, the considerable lowering of the switching field could point out that the magnetization reverses in the Buckling mode. However, it is not clear to what extent the Buckling magnetization reversal mode gives rise to a lowering of the switching field.

To approximate the Buckling reversal mode, Yuan *et al.* developed a modified Buckling model. For a fixed aspect ratio, the model predicts that the single domain coercive field is roughly inversely proportional to the width of the particle. This proportionality was approximately followed for NiFe and Co with a width of 40 to 100 nm and an aspect ratio ranging from 3.75 to 20, and distances between the dots of 50 to 100 nm [106]. However, figure 6.16 shows a poor inverse dependency of the coercive field with the width for the arrays of Co with an aspect ratio of 1.5.

In order to interpret the discrepancy between the results, consider the differences in the arrays of thin nanoscale magnetic dots under investigation. The width of the NiFe and Co dots and the distances between the dots examined by Kirk *et al.* are comparable with those of our experimental data. However, Kirk *et al.* investigated dots with an aspect ratio of > 3.75, whereas the Co dots in figure 6.12 have an aspect ratios of 1.5. Figure 6.8 shows that the loop shapes of the Co dots width an aspect ratios of 1.5 deviates from that of the Co dots having an aspect ratio of 2.5. As described in section 6.3.2, discrepancies in the shape of the hysteresis loops indicate various magnetization reversal modes, leading to different switching fields. Therefore, the lower aspect ratios could be the reason for the weak dependency.

Also a weak inverse dependency of the coercive field with the width, similar to our results was reported by Girgis *et al.* for Co dots of width ranging between 100 and 600 nm, and aspect ratios of 1.5, 2, 3, and 4. An MFM image at zero field showed that, even though a vast majority of the dots were already in the flux closure state, there was still a percentage in the single domain state [107]. Girgis *et al.* concluded that the switching of nanoscale particles is a random process that is governed by sample defects, such as edge roughnesses, interface roughnesses, impurities, etcetera. Concluding from the discussion in section 2.3.2, we will add to this, that also the interdot coupling has a substantial influence on the switching behavior. Experimental results of arrays of nanoscale Ni dots, which were separated less than 50 nm, revealed that approximate flux closure in a cluster of dots induced collective rotation due the interdot coupling [108]. How to take into account the combination of the effects on the magnetization reversal is not obvious. Therefore, in the following we will only qualitatively describe the effects of the afore mentioned contributions to the magnetization reversal processes.

As stated before, magnetization reversal starts with the formation of edge domains. The different edge domain configurations induce a switching field distribution. As a consequence, at zero field part of the dots can already have reversed the magnetization. Jonson *et al.* confirmed this statement experimentally by presenting an MFM image at zero field of elliptical permalloy dots that were all in the single domain state but had different polarities [109].

Edge domains formed to reduce the magnetostatic energy, play an important role in the magnetization reversal [110]. Edge roughness encourages the nucleation of domains, because the exchange coupling at the edge of a dot is diminished. A reduction of the switching field of about 40 % was found by Gadbois *et al.* if edge roughnesses were introduced into the simulations [111]. If edge roughness could promote a Buckling instability, then the discrepancy between the experimental data and the calculated Stoner-Wohlfarth data can partially be explained by the existence of edge roughness.

Beside the significant influence of edge roughnesses, other mechanisms also have a considerable contribution to the lowering of the switching field. In section 2.3.2 interdot fields of arrays of closely spaced Co dots were calculated and insight into the approximate flux closure was given. The calculations and the approximate flux closure demonstrated the significant effect of interdot coupling on the magnetic switching behavior of high areal density arrays with nanoscale elements.

Consider figure 6.13 that shows the hysteresis loops for ellipses of major axis $l = 400$ nm and minor axis $w = 160$ nm, measured by sweeping an in-plane field along the major axis (○) and along the minor axis (●). Although the measured loop with the field applied along the minor axis of the elliptical polycrystalline dots displays a lower remanence than the loop with the field applied along the major axis, the coercive field of both loops more or less coincides. For polycrystalline Co the crystalline anisotropy can be neglected and for ellipses with an aspect ratio of 2.5 the main anisotropy contribution is the shape anisotropy. Therefore, the equal values of the coercive fields is surprising, because with the field applied along the minor axis a more slanting hysteresis loop is expected. Although the OOMMF hysteresis loop computations in figure 2.10 showed that the interdot coupling strongly influences the coercive field, the equal values of the coercive fields could not yet be explained by the interdot coupling. However, we could think about a possible contribution of the interdot coupling to the coercive fields for applied fields along the major axis and along the minor axis, respectively.

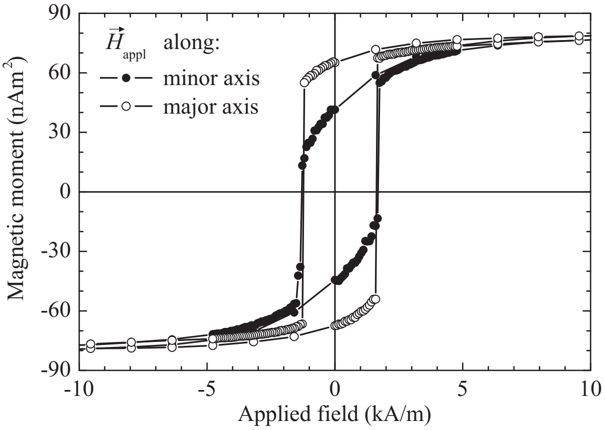

Figure 6.13: Hysteresis loops along the major and minor axis for 160×400 nm^2 dots.

We suggest that the interdot coupling, which induces an approximate flux closure between individual dots of the array, facilitates the magnetization reversal and thereby influences the switching field. As stated before, neighboring Co dots can form clusters of approximate flux closure interdot coupling. Suppose that the clusters act as pseudo-particles that grow in size and gradually rotate the average magnetic moment of the cluster while the applied field is reduced. The rotation of the clusters is energetically more favorable, because the total energy is reduced by flux closure through the neighboring cells [112]. Therefore, the interdot coupling can facilitate the magnetization reversal and counteract the shape anisotropy of the individual dots. Our suggestion is confirmed by the outcome of OOMMF simulations of the switching of a single dot, which revealed a higher remanence than the experimental data. The lower remanence indicates that part of the Co dots of the array reverses the magnetization before zero field.

6.3.4 Geometry Effect on the Switching Behavior

After providing insight into the magnetization reversal modes and the mechanisms that contribute to a lowering of the switching field, the correlation between the results will be analyzed. First, notice that the data points in figure 6.12 for Co dots of $w > 150$ nm with the rectangular shape are rather scattered. This scattering cannot be due to sample to sample variation, because the samples are processed on the same substrate. However, as stated before, variations in size and shape of individual dots can produce a considerable distribution of switching fields.

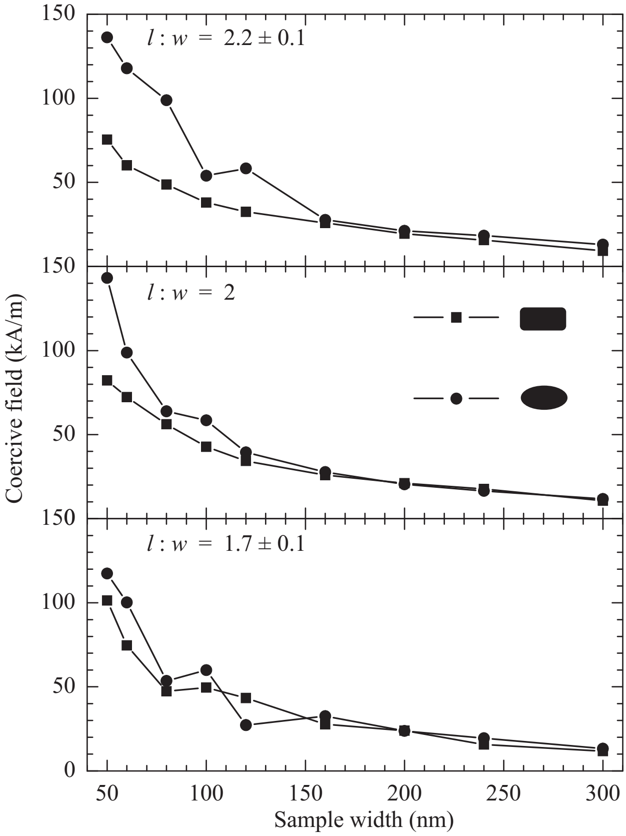

Figure 6.14: Outcome of OOMMF simulation to investigate the geometry effect of the individual Co dots on the switching behavior.

Another striking feature that is observable in figure 6.12 is sort of a step in the data of the coercive field at the transition between elliptical Co dots of width $w < 150$ nm and the rectangular dots of width $w > 150$ nm. The difference in shape might cause this decrease. The shape dependency is investigated with OOMMF simulations [44]. For the simulations of rounded rectangles and ellipses we used Co as material with saturation magnetization $M_s = 1400$ kA/m and exchange stiffness $A = 30$ pJ/m. The ellipses and rounded rectangles are divided into two-dimensional grids of 5×5 nm^2 cells. The outcome of the simulations is plotted in figure 6.14.

First, figure 6.14 shows an artificial fluctuating coercive field caused by the subdivision of ellipses in square cells inducing an unrealistic edge roughness, which is not so pronounced for the rounded rectangles. For a width $w > 150$ nm the shape effect is of minor influence, and the coercive field is smoothly varying with the width. Moreover, there is no step at 150 nm. Nevertheless, opposed to the experimental data, figure 6.14 shows that for $w < 150$ nm the elliptical dots have a higher switching field than the rounded rectangles. This can be explained by the fact that the Buckling instability proceeds easier for the rectangular dots with s-state magnetization configuration than for elliptical dots, because of the higher amplitude of the Buckling wave. Furthermore, the influence of the shape effect decreases with decreasing ratio, and is not significant for an aspect ratio of 1.7 due to a symmetry increase of the dots. All in all, the shape effect cannot explain the decrease of the coercivity.

However, as stated before edge roughness can have an effect on the reduction of the switching field. Bryan *et al.* demonstrated that the edge roughness can be reduced by using a higher electron beam exposure dose [113]. Considering that we used an exposure dose ranging from 400 to 500 μC/cm^2 for the rectangular dots, and only a dose between 60 and 100 μC/cm^2 for the elliptical dots, an edge roughnesses induced decrease of the coercive field is presumable.

Concluding this section, the magnetization reversal of arrays of polycrystalline Co dots was investigated using SQUID measurements. The measurements demonstrated various shaped hysteresis loops and revealed no distinct dominant trend. On the basis of the shape of the hysteresis loops the switching mode was analyzed. Furthermore, we discussed the contribution of edge roughness and interdot coupling to a lowering of the switching field. Finally, we suppose that edge roughnesses induced a decrease of the coercive field for elliptical Co dots in comparison to the rectangular dots. Therefore, in the next section the analysis of the free layer switching of arrays of MTJs, the arrays of MTJ with a width $w > 150$ nm are treated separately from the arrays of MTJs with a width of $w < 150$ nm.

6.4 Free Layer Switching of Sub - μm MTJs

In this section, we discuss the free layer switching of arrays of sub - μm MTJs illustrated in figure 6.3(b). The layout of the samples is the same as that of the samples with arrays of 5 nm thick polycrystalline rectangular and elliptical Co dots of section 6.3. The MOKE technique is used to measure hysteresis loops locally at the residual part and at the part containing the sub - μm MTJ pillars of the sample, as explained in section 6.2.2. By comparing the loop of the patterned part with the loop of the residual part, the magnetic switching of the free layer of sub - μm MTJs is investigated as a function of the size and length to width aspect ratio. As is mentioned in section 6.3 of this chapter, we discuss the magnetic properties of the elliptical MTJs separately from the rectangular MTJs.

The coercive field as a function of the width of the rectangular MTJs is plotted in figure 6.15. For clarity, the error bars are not included in the graph, and are of the order of about 1 kA/m. The coercive field shows a faint decrease as function of the width and, although not so pronounced for the wider MTJs, on average the coercive field increases with increasing aspect ratio. This increase is anticipated, taking into account that the magnetization reversal begins at edge domains that gradually grow and nucleate to form

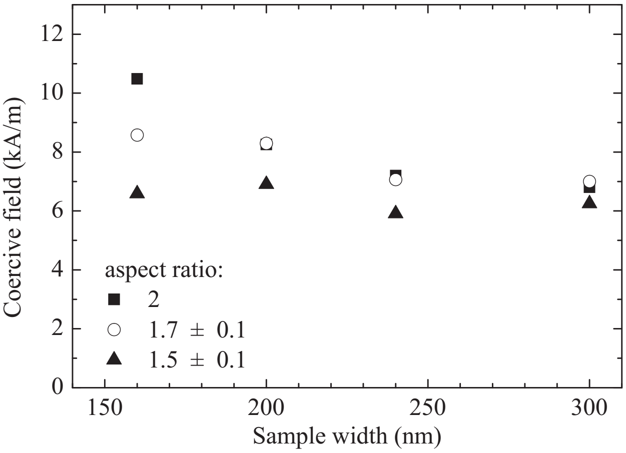

Figure 6.15: Plot of the coercive field as function of the width of the rectangular MTJs for different aspect ratios.

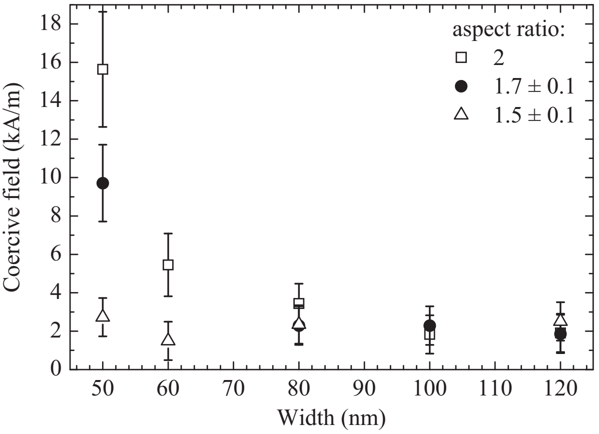

Figure 6.16: Plot of the coercive field as function of the width of the elliptical MTJs for different aspect ratios.

a flux closure within an individual dot.

Figure 6.16, in which the coercive field is plotted as function of the width for elliptical MTJs, also shows an increase of the coercive field with increasing aspect ratio. Furthermore, the coercivity is sharply increasing with decreasing MTJ width. However, the coercive fields are moderate inversely proportional to the width of the MTJs, corresponding to the data of the Co dots in figure 6.12 and the results reported by Girgis *et al.*.

After discussing the size dependency of the free layer switching of sub-μm MTJs, we now describe the magnetic switching as function of the length to width aspect ratio. Therefore, the measured coercive fields of $w = 60$ and 80 nm elliptical MTJs are plotted as function of the aspect ratio in the two top graphs of figure 6.17, and the data of $w = 160$

and 240 nm rectangular MTJs are plotted in the bottom graphs of figure 6.17. Note that the experimental data with an aspect ratio of 1.5, 1.7, and 2, respectively, were already plotted as a function of the width of the MTJs in figure 6.15 and 6.16. The dotted lines in figure 6.17 are lines to guide the eye. The figure shows for the elliptical as well as for the rectangular MTJs, the coercive field first increases as function of increasing ratio, and after reaching a maximum decreases again.

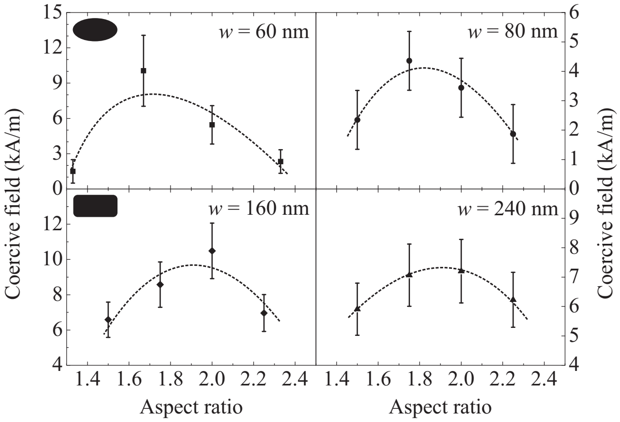

Figure 6.17: Graphs of the coercive field as function of the aspect ratio for w = 60 and 80 nm elliptical MTJs, and for w = 160 and 240 nm rectangular MTJs.

In contrast to the results of the coercive field presented by Kirk *et al.* for ratios between 3.75 and 20, we do observe an effect of the switching field for sub-μm MTJs with a moderate length to width aspect ratio $1.5 \leq \ l \ : \ w \ \leq 2.5$. In MTJs with moderate aspect ratios just above 1 vortices that initiate the magnetization reversal nucleate easier, therefore, the initial increase can be explained. The decrease after reaching the maximum is more difficult to understand. As stated before, the increase of the interdot field with the aspect ratio, shown in figure 2.9, could provide a contribution. However, the ratio increase also induces a higher switching field due to the shape anisotropy.

Probably, the decrease of the coercive field with aspect ratio originates from the competition between the configurational array anisotropy and the shape anisotropy, which for our specific geometry of the array and MTJs produces a decrease. Thereby, confirming that the interdot coupling causes the deviance from the inverse dependency of the coercive field as function of the width, stressing again the importance of the interdot coupling on the magnetic switching behavior is.

In addition to the switching characteristics, the analysis of the hysteresis loops revealed a shift of the loop corresponding to the free layer, which seemed to increase slightly with decreasing width of the sub-μm MTJs. Resistance versus applied field measurements of MTJs ranging from 30 nm to 1 μm with aspect ratios from 1 to 7 that were investigated with a c-AFM by Kubota *et al.*, also showed a shift [114]. The shift is a consequence of the competition between the ferromagnetic Néel coupling through the interface roughness and the stray field coupling from the edges of the MTJs. Assume a uniform magnetized MTJ of width w and length l, that has a fixed Co top layer of the artificial antiferromagnet

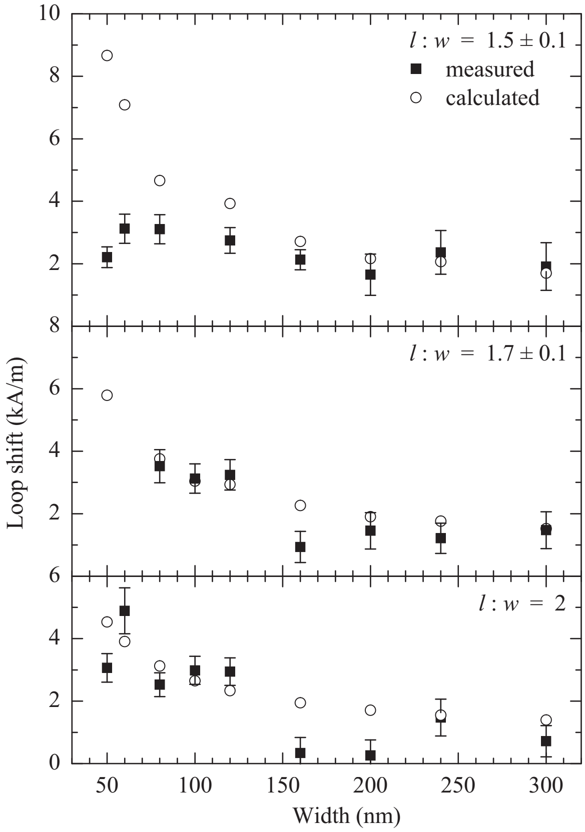

Figure 6.18: Graphs of measured and with equation 6.6 calculated loop shifts as function of the width for aspect ratios of 1.5, 1.7, and 2.

(AAF) of thickness $d_{\text{fix}} = 4$ nm, and a measured magnetization $M_{\text{fix}} = 1129$ kA/m. Then, the stray field coupling strength over the AlO$_x$ barrier of thickness $d_{\text{bar}} = 1.1$ nm can be approximated by [115]:

$$H_{\text{D}} = \frac{2M_{\text{fix}}wld_{\text{fix}}}{(l^2 + 4d_{\text{bar}}^2)\sqrt{l^2 + 4d_{\text{bar}}^2}} \quad . \tag{6.6}$$

With the Néel coupling field $H_{\text{N}} = 766$ A/m derived from the hysteresis loop of an unstructured sample, the net shift of the loop is given by $\Delta H = H_{\text{D}} - H_{\text{N}}$. Figure 6.18 shows the measured loop shift and the loop shift calculated with equation 6.6 as function of the width for aspect ratios of 1.5, 1.7, and 2. Apart from a few data points, the calculated and measured shifts show a fairly good general agreement. The measured shifts of aspect ratios 1.7 and 2 follow the trend of the calculated shifts and increase slightly with decreasing width. The measured data deviate from the calculated data for MTJs with a width $w < 100$ nm and aspect ratio 1.5. Supposedly, this deviation is caused by a nonuniform magnetization in the MTJs, because at remanent state small aspect ratios MTJ easily form vortices and MTJs with a flux closing vortex state do not generate a stray field.

6.5 Conclusion

In conclusion, a SQUID magnetometer was used to investigate the magnetization reversal of dense arrays of polycrystalline nanoscale Co dots. Although the Stoner-Wohlfarth model gives an upper bound for the switching fields of quasi-single domain elements, the results of the polycrystalline Co dots that were studied in this Thesis were much to low compared to the Stoner-Wohlfarth model. Edge roughnesses considerably contribute to the lowering of the switching field. Furthermore, by comparing the experimental value of the remanence with that of OOMMF simulations of the switching of a single Co dot, we demonstrate that the interdot coupling has a major influence on the magnetic switching behavior of ultra-high areal density arrays of nanoscale magnetic elements.

The outcome of the analysis of the magnetization reversal of arrays of Co dots was used to interpret the results of the MOKE experiments of arrays of sub-μm MTJs as function of the size and length to width aspect ratio. The simplified Buckling model predicts an inverse proportionality to the width that was not followed by the experimental data. The simplified Buckling model does not include an arrangement of dots in a lattice. For our specific arrangement of dots in the array, the deviation originates from the competition between the configurational array anisotropy and the shape anisotropy.

In addition, the hysteresis loops showed a loop shift, similarly, Kubota *et al.* found a shift of the resistance versus applied field loop. Using an approximation to calculate the magnetic stray field of sub-μm MTJs, the shift could be calculated using the value of the Neel coupling field strength of an unstructured sample. The calculated values showed a good agreement with the measured results.

Chapter 7

Magnetization Losses in Sub - μm CoFeB Dots

In chapter 5 we discussed several pattern transfer techniques, such as transferring the pattern by means of high ion density Cl_2-based plasmas. A disadvantage of Cl_2-based plasmas is the formation of chlorinated etch residues on the sidewalls of the etched features. Jung *et al.* showed that for etched features with a width of approximately 2 μm, 10 minutes of postetch H_2O rinsing in a N_2 dry box or *in situ* cleaning with a H_2 or SF_6 plasma is effective to prevent corrosion by chlorinated etch residues on the sidewalls [116]. Furthermore, the various postetch procedures showed no significant differences in the long term magnetization. However, it has not been addressed whether postetch treatments are still effective for sub - μm elements.

Besides avoiding corrosion, an additional challenge in patterning dense arrays of elements is mastering mask erosion. During etching, facets form at the side walls of the mask due to physical sputtering of the mask material. The initially formed facets propagate in time and after a while the mask facets will intersect with the original surface of the sample. Eventually, the mask facets propagate laterally, thereby exposing the feature to the plasma, resulting in sloped sidewalls [117].

In the following sections[1], we present investigations on the reduced magnetization of patterned CoFeB dots with lateral dimensions ranging from 0.3 to 6.4 μm, dry etched with a Cl_2-based plasma and a subsequent postetch H_2O rinsing in a N_2 dry box. CoFeB is chosen as the magnetic material, because of the enormous current interest for the high tunneling spin polarization of CoFeB when combined with Al_2O_3 or MgO barriers in MTJs. Superconducting Quantum Interference Device (SQUID) magnetometer measurements and scanning electron microscopy (SEM) studies are performed and qualitatively analyzed in order to distinguish between the reduction of the magnetic moment due to chlorinated etch residues and due to faceting of the mask.

7.1 Dry Etching of CoFeB Dots

To study the reduction of the magnetization of CoFeB dots etched in a high ion density Cl_2-based plasma, we have used samples of the following composition: Si(001)/ SiO_x// 50 Å Ta/ 155 Å $Co_{24}Fe_{56}B_{20}$/ 50 Å Ta. The samples are grown in a sputter system with a base pressure of $< 10^{-8}$ mbar, at a rate of approximately 0.5 Å/s in a $\sim 10^{-2}$ mbar argon gas pressure. A bilayer resist of polymethylmethacrylate (PMMA) and hydrogen silsesquioxane (HSQ) is patterned by electron beam lithography at 100 kV and an exposure dose of 500 μC/cm^2. To map the size dependency of the magnetic properties, the layout of the patterns consisted of square CoFeB dots of thickness $d = 155$ Å and width w ranging from 0.3 to 6.4 μm. The number of dots in each layout, n_w, is chosen such that the total magnetic volume $V = n_w d w^2$ is identical, and equal to that of the unetched reference sample. Following the electron-beam exposure, the HSQ is developed and the PMMA layer is etched in a low pressure O_2 reactive ion plasma.

---

[1] Part of this chapter is published in J. Vac Sci. Technol. B, **24**, 2627, (2006)

After fabricating the mask, a high-ion density $Cl_2/BCl_3/N_2$ plasma is used for high-speed dry etching the CoFeB dots. To remove the chlorinated etch residues from the sidewalls of the etched CoFeB dots, the samples are rinsed in H_2O in a N_2 dry box for 10 minutes, before being exposed to atmosphere. The magnetic properties of the etched samples and the unetched reference sample with magnetic volume V, are measured at room temperature with a SQUID magnetometer.

Figure 7.1 shows the hysteresis loops of the reference sample and the samples with

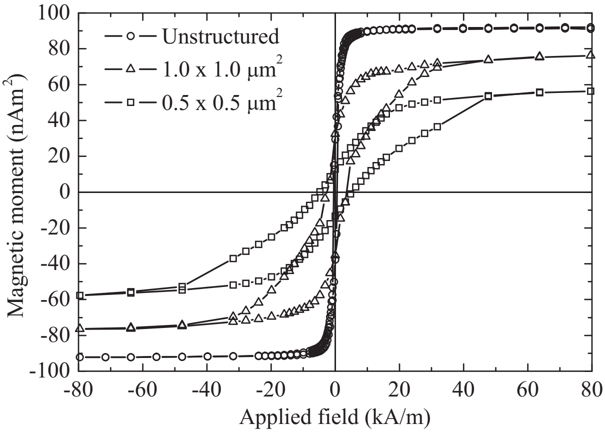

Figure 7.1: Hysteresis loops of a unetched reference sample, and etched samples with dots of width 1 and 0.5 μm. The measurements are performed at room temperature and the direction of the magnetic field is applied parallel to the sides of the CoFeB dots.

dots of nominal width of 1.0 and 0.5 μm. The direction of the magnetic field is applied parallel to the sides of the CoFeB dots. A linear background is subtracted to correct for the diamagnetic substrate response. As expected for CoFeB dots with decreasing width, the magnetization is harder to switch, and the coercive field increases [78]. Most importantly in view of the degradation of the magnetization, figure 7.1 shows that the magnetic moment of the etched samples is significantly reduced in comparison with the reference sample. Furthermore, the sample with the 0.5×0.5 μm^2 dots has an even lower saturation magnetization than that of the sample with the 1.0×1.0 μm^2 dots.

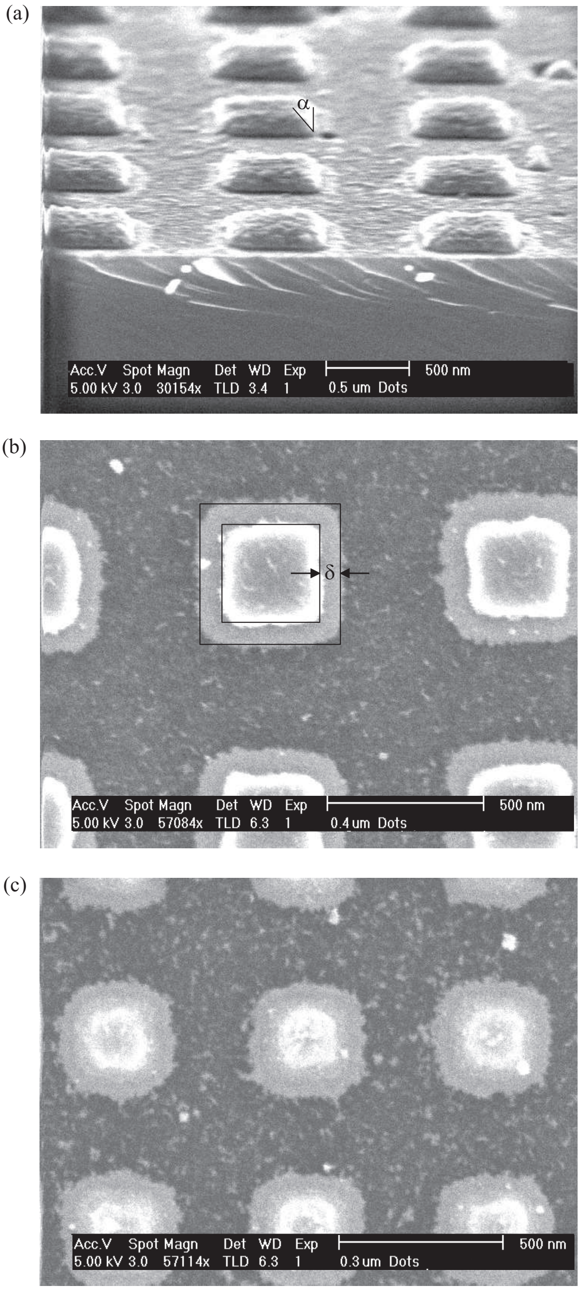
(a)
α
Acc.V Spot Magn Det WD Exp
5.00 kV 3.0 30154x TLD 3.4 1
500 nm
0.5 um Dots
(b)
δ
Acc.V Spot Magn Det WD Exp
5.00 kV 3.0 57084x TLD 6.3 1
500 nm
0.4 um Dots
(c)
Acc.V Spot Magn Det WD Exp
5.00 kV 3.0 57114x TLD 6.3 1
500 nm
0.3 um Dots

Figure 7.2: Scanning electron microscopy pictures of CoFeB dots etched in a $Cl_2/BCl_3/N_2$ plasma at 160 °C. The cross-section of $0.5 \times 0.5\ \mu m^2$ dots illustrates the erosion of the mask with faceting angle α (a). The top views of $0.4 \times 0.4\ \mu m^2$ dots (b) and $0.3 \times 0.3\ \mu m^2$ dots (c) demonstrate the size effect.

7.2 Faceting of the Mask

Scanning electron microscopy (SEM) pictures are examined to study the cause of the reduced magnetization of the sub - μm CoFeB dots. In figure 7.2(a) a SEM picture of the crosssection of the sample with the 0.5×0.5 μm^2 CoFeB dots is shown. The CoFeB dots are difficult to distinguish, because the total thickness of the layers is less than 30 nm. However, the mask on the dots is clearly visible. The crosssection illustrates that etching in a Cl_2-based plasma causes erosion of the mask, resulting in a facet angle α, as is indicated in figure 7.2(a). As stated before, faceting of the mask leads to sloped sidewalls of the CoFeB dots. This is confirmed by the top view SEM pictures of the 0.4×0.4 μm^2 dots and the 0.3×0.3 μm^2 dots in figure 7.2(b) and 7.2(c), respectively. Note that because of the proximity effect caused by the lithography process the width of the CoFeB dots is enlarged in comparison to the nominal width w. Furthermore, the SEM pictures in figure 7.2(b) and 7.2(c) show that the dots are in fact truncated square pyramids. The sidewalls of the pyramids color light gray in the pictures. The top side width $(w - 2\delta)$ is confined by the mask, recognizable from the bright edges due to charging of the resist. The rim width of the confinement δ is determined using the base and top side circumferences, as graphically depicted in figure 7.2(b).

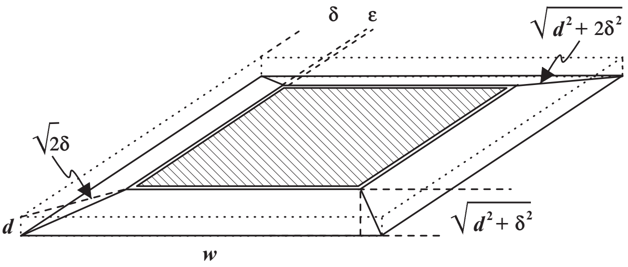

Figure 7.3: Schematic drawing of a CoFeB dot. The dotted lines represent the designed dot, and the solid lines depict the truncated square pyramid with base and top side widths w and $(w - 2\delta)$, respectively. The hatched area represents the top side of the the truncated pyramid that did not corrode due to the chlorinated etch residues with a penetration depth ε.

Figure 7.3 shows a schematic drawing to visualize the shape of a CoFeB dot after etching. The drawing neglects the enlargement of the dot with respect to the nominal width. The dotted lines represent the designed dot with thickness d and width w. The contours of the truncated square pyramid with base and top side widths w and $(w - 2\delta)$, respectively, are depicted by the solid lines. As mentioned before, the thickness d and the total number of dots in each layout n_w are known. Therefore, by measuring the rim width δ the actual geometric volume V_G can be calculated by:

$$V_G = \frac{1}{3} d \left[w^2 + (w - 2\delta)^2 + \sqrt{w^2 (w - 2\delta)^2} \right] n_w \quad . \tag{7.1}$$

Due to the different magnifications of the various SEM pictures, only the rim width of the CoFeB dots with a width ≤ 2 μm could be resolved. There is a large spread in measured values, ranging from about 27 nm to approximately 125 nm. The average rim width

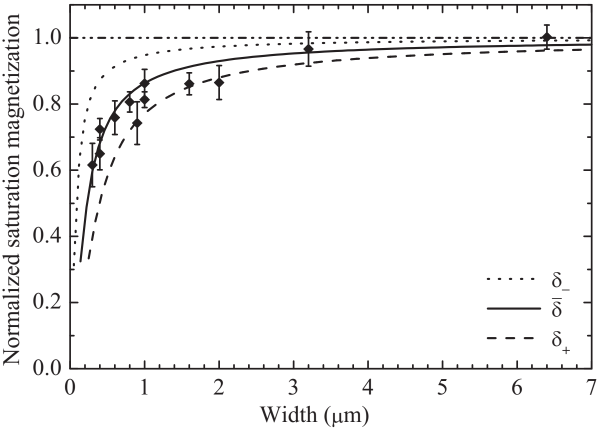

Figure 7.4: Normalized saturation magnetization as a function of the width of the etched CoFeB dots. The dotted line and the dashed line are the results of calculations with $\delta_- = 27$ *nm and* $\delta_+ = 125$ *nm, respectively.The solid line is the result of the calculation with the weighted average rim width.*

yielded $\bar{\delta} = (72 \pm 6)$ nm.

To map the size dependency of the magnetization losses due to the faceting of the mask, we have plotted the normalized saturation magnetization as a function of the nominal width of the etched CoFeB dots in figure 7.4, and compared it to that of the reference sample. In the analysis of the SQUID measurements, the data are corrected for the actual width of the CoFeB dots. As can be seen in figure 7.4, there is a considerable spread in data points due to sample to sample variation, which is confirmed by the SEM pictures. The faceting strongly depends on the exact characteristics of the mask. Variety of the resist profile due to the development process and etching of the PMMA layer in a O_2 plasma determines how a facet exactly propagates in time. Another explanation of the spread in data points is the precise conditions during etching, such as the stability, density and lateral inhomogeneity of the plasma, which can cause differences between dots on various substrates.

However, in spite of the cloud of scattered data points, the plot of the normalized saturation magnetization shows a degradation of the magnetic properties of about 20-40% for the CoFeB dots in the sub - μm regime. To get more insight into the effect of the sloped sidewalls on the magnetization of the etched dots, we used formula 7.1 normalized by the volume of the reference sample to calculate the normalized saturation magnetization. The results of the calculations are plotted as function of the width w for $w \geq 2\delta$ in figure 7.4. If the average rim width from our SEM data is used for the calculation, the solid line resulted. The solid line is in good agreement with the SQUID data, given the fact that no fitting is used. For $w < 2\delta$ the mask is completely annihilated beyond this value resulting in the erasure of the CoFeB dots. This implies that the feasibility of measuring the magnetic properties of etched magnetic elements with a width <0.1 μm in a Cl_2-based plasma using a bilayer resist of PMMA and HSQ is questionable. In order to pattern dense arrays of magnetic memory elements with sub 0.01 μm^2 dimensions, the mask must be hard enough and the sidewalls have to be sufficiently steep. To impede mask erosion, SiO_2 can be used as alternative mask material for shallow etching [118], although for deep etching even harder materials are necessary. For example, a 20 nm thick Ta mask is applied for hardening mask etching MRAM multilayers using a CO/NH_3 gas plasma [80].

7.3 Corrosion by Chlorinated Etch Residues

To illustrate the uncertainty in δ, the upper dotted and lower dashed lines in figure 7.4 are the curves using a rim width of $\delta_- = 27$ nm and $\delta_+ = 125$ nm, respectively. Most of the data points are within those limits, which further corroborates the consistency between the SQUID and SEM data. Nevertheless, note that the values of the SQUID data appear to be systematically lower than the solid line that is calculated using $\bar{\delta}$. In order to distinguish between the reduced magnetization due to the chlorinated etch residues and the faceting of the mask, the effective magnetic volume V_{M} has to be determined using the SQUID data and correlated with the SEM data. We calculated the effective magnetic volume by dividing the saturation magnetization of CoFeB by the experimentally determined magnetic moment of CoFeB. Assuming that the corrosion due to the etch residues is proportional to the surface area, then the ratio of the surface area of the sidewalls to the volume of the dot becomes increasingly important for the sub-μm dots, because the magnetic moment scales with the volume. For all dot sizes the effective magnetic volume is smaller than the geometric volume, indicating that the CoFeB dots slightly corroded due to the etch residues. If we suppose that the difference between V_{G} and V_{M} is the volume that is corroded by the chlorinated etch residues, we can derive a chloride penetration depth ε. Therefore, consider again figure 7.3. The surface area of one side of the pyramid is $\frac{1}{2}\sqrt{d^2+\delta^2}\,[w+(w-2\delta)]$, a pyramid has four sides and each sample has n_w pyramids. Accordingly, we can derive the chloride penetration depth ε using:

$$\varepsilon = \frac{V_{\mathrm{G}} - V_{\mathrm{M}}}{4\sqrt{d^2+\delta^2}(w-\delta)n_w} \quad . \tag{7.2}$$

We have found a penetration depth of the chloride of less than 10 nm. However, this chloride penetration depth must be seen as a rough estimate for several reasons. First of all, the patterning by electron beam lithography causes rounding of the corners due to the proximity effect, which is not taken into account. As a consequence of this rounding, which is clearly visible in figure 7.2(c), the geometric volume V_G is overestimated. On the other hand, we disregarded the Ta layers, thereby overestimating the rim width δ leading to underrating V_G. The samples are measured approximately 40 days after etching and subsequent rinsing. Therefore, as a first approximation, a penetration depth of less than 10 nm implies that 10 minutes of postetch H_2O rinsing in a N_2 dry box is sufficient to prevent significant major corrosion of CoFeB dots. Furthermore, for dots with a width > 1 μm the reduction of the magnetization due to the chlorinated etch residues would be not more than 1 percent. Accordingly, our results are in accordance with the results of Jung *et al.* [116], which showed no significant change in magnetic properties over a period of 6 months.

7.4 Conclusion

In conclusion, a high ion density $Cl_2/BCl_3/N_2$ plasma is used for etching CoFeB dots with a width ranging from 0.3 to 6.4 μm. The magnetic properties are measured with a SQUID magnetometer. The hysteresis loops of the etched CoFeB dots show a reduced magnetization. The SEM picture of the crosssection of 0.5×0.5 μm^2 dots shows faceting of the mask, leading to sloped sidewalls. The actual geometric volume is calculated using the measured rim widths to determine the reduction of the magnetization due to the faceting of the mask. The geometric volume derived from the SEM data is in good agreement with the effective magnetic volume resulting from the SQUID data. The difference between geometric volume and the effective magnetic volume is used to determine a chloride penetration depth of less than 10 nm. Therefore, in accordance with the results of Jung *et al.* [116], 10 minutes of postetch H_2O rinsing in a N_2 dry box is sufficient to prevent considerable corrosion of CoFeB dots.

Chapter 8

Electrical Characterization of Sub - μm MTJs

In this chapter, the electrical characteristics of sub - μm MTJs are discussed. The first experimental results of the *I*-*V* response of 1×1 μm^2 MTJs are presented that were measured as stepping stone for continuing research. The quality of the AlO$_x$ barrier is the key part in the determination of the electrical properties. Therefore, the electrical properties of a nanometer thin AlO$_x$ barrier are investigated by measuring *I*-*V* characteristics. Due to the delicate nanofabrication process of the samples, only 30 % of the measured 32 MTJs showed a response resembling tunneling. Furthermore, we introduce the scanning force microscopy (SFM) technique that can be used to investigate the electrical characteristics of the nanoscale MTJs. However, due to resist remains no reliable contact between tip and sample could be established. As a consequence, we were not able to measure the electrical transport properties of the nanoscale MTJ samples.

8.1 *I*-*V* Characteristics of Ultra Thin AlO$_x$ Barriers

In this section, we present the *I*-*V* characteristics of nanometer thin AlO$_x$ barriers of 1×1 μm^2 square MTJs. Aside from the barrier thickness, we used a multilayer MTJ stack, similar to the sequence of which the electrical properties are extensively investigated [24], with the following composition: Si(001)/ SiO$_x$// 50 Å Ta/ 50 Å Co$_{90}$Fe$_{10}$/ 100 Å FeMn/ 35 Å Co$_{90}$Fe$_{10}$/ 11 Å AlO$_x$/ 150 Å Co$_{90}$Fe$_{10}$/ 50 Å Ta. The *I*-*V* characteristics of the AlO$_x$ barriers are determined by 4-point electrical measurements. The process flow of the sample fabrication is depicted in figure 8.1.

According to the procedure described in section 5.4.2, a high-ion density Cl$_2$-based plasma is used to etch the bottom electrode with 1 mm^2 contact patches and 100 μm wide leads in the multilayer stack as is shown in figure 8.1(a). MTJ pillars with a square surface area of 1 μm^2 are also etched in a Cl$_2$-based plasma using a trilayer resist mask of polymethylmethacrylate (PMMA), propyleneglycol monomethyl ether acetate (PGMA), and hydrogen silsesquioxane (HSQ). Figure 8.1(b) shows a schematic of an etched MTJ pillar, which is not to scale. In order to isolate the top electrode from the bottom electrode, a SiN dielectric material layer is sputter deposited, as illustrated in figure 8.1(c). After solving the trilayer resist mask in acetone a layer of Ta is sputter deposited, as is indicated in figure 8.1(d) and (e), respectively. Finally, orthogonal to the bottom electrode, the top electrode with 1 mm^2 contact patches and 100 μm wide leads is etched as is shown in

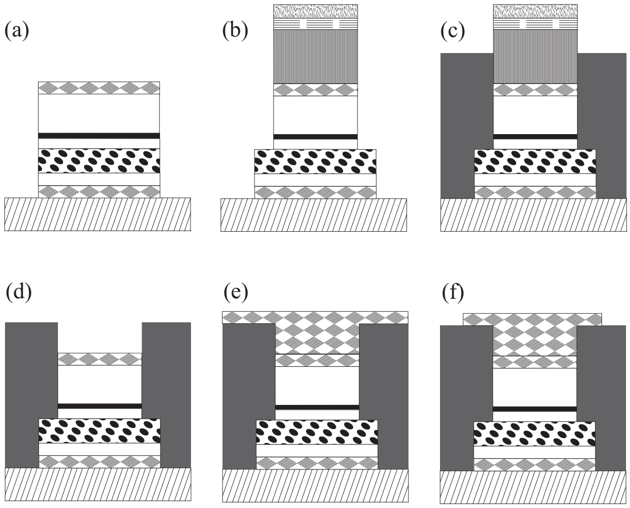

Figure 8.1: The process flow of the 4-point electrical sample fabrication. With a Cl_2-based plasma, a bottom electrode with 1 mm^2 contact patches and 100 μm wide leads is etched in the multilayer stack (a). Using a trilayer resist mask of PMMA, PGMA, and HSQ, square MTJ pillars with a surface area of 1 μm^2 are etched in a Cl_2-based plasma (b). A SiN dielectricum layer is sputter deposited to isolate the top electrode from the bottom electrode (c). The trilayer resist mask is solved in acetone (d), and a layer of Ta is sputter deposited (e). Finally, orthogonal to the bottom electrode, a Ta top electrode is etched, also with 1 mm^2 contact patches and 100 μm wide leads (f).

figure 8.1(f).

The I-V characteristics of the nanometer thin AlO_x barriers are determined by applying a voltage over an MTJ pillar on the cross-point of the bottom and top electrode, while measuring the tunnel current through the barrier. The I-V response of the 1×1 μm^2 MTJs showed in principle three different characteristics. Namely, an ohmic like response, a response resembling breakdown, and a tunneling response. Figure 8.2 shows examples of the different type of I-V characteristics. Approximately 30 % of the measured MTJs showed a response that appeared as tunneling and had a resistance-area product between approximately 20 and 50 $k\Omega\mu m^2$. A typical example is shown in figure 8.3(a), and the numerical derivative of the I-V response, which is defined as conductance, normalized by the value at $V = 0$ V, is plotted in 8.3(b).

In literature most often the experimental I-V response is fitted to the Simmons model, expressed in equation 2.2. However, the normalized conductance as function of the applied voltage displays roughly a parabolic behavior. This type of behavior implies an asymmetrical barrier [119], whereas the Simmons model is derived for a symmetric rectangular barrier. The Brinkman formula 2.3 for trapezoidal barriers is more suitable to fit our experimental data. During fitting the barrier thickness was constrained between 0.8 and 1.5 nm. The fits to the data for various measurements yielded average barrier heights between 1.2 and 2.3 eV, and an asymmetry parameter ranging from 0.3 to 0.8 eV, these barrier parameters and the zero-bias resistance are close to reported observations in literature [120].

The parabolic behavior of the conductance validates one of the criteria for tunneling. The other so-called Rowell criteria for MTJs are an exponential dependence of the conductance on the barrier thickness, and a weak insulating-like temperature dependence [121]. The exponential dependence on the barrier thickness was not investigated, because we did not vary the barrier thickness. Besides that, the 1×1 μm^2 MTJs samples are not appropriate for temperature dependency measurements. Therefore, no conclusive evidence can be presented to indicate that tunneling is the dominant transport mechanism.

Resistance measurements as a function of an applied magnetic field yielded no significant magnetoresistance for the 1 μm^2 MTJs. Roughness at the interfaces of the nanometer thin AlO$_x$ barriers can be the reason for the absence of magnetoresistance, because only

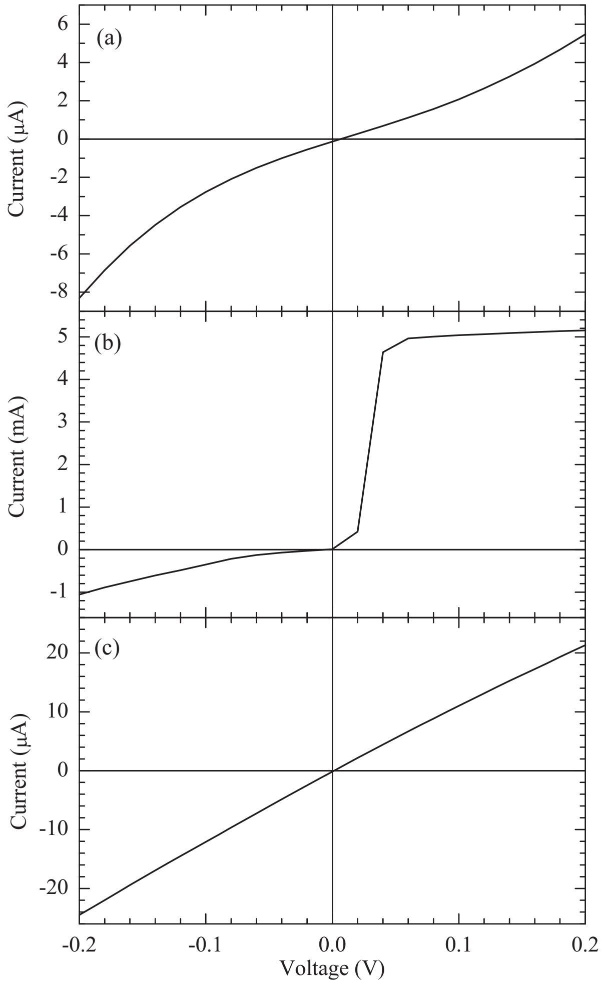

Figure 8.2: Examples of the different I-V characteristics, showing a tunneling response (a), a response resembling breakdown (b), and an ohmic like response (c).

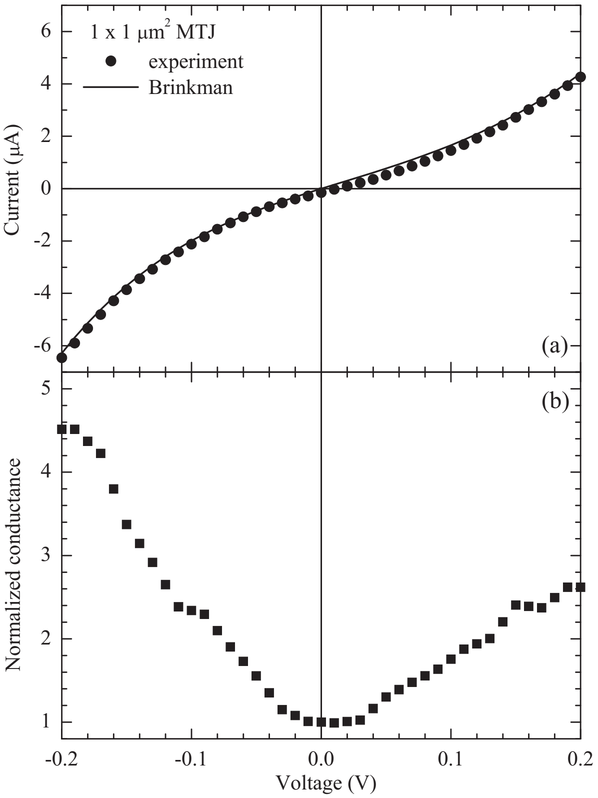

Figure 8.3: Current voltage characteristics of a nanometer thin AlO_x barrier, is fitted with the Brinkman formula (a), and the normalized conductance (b).

30 % of the measured MTJs showed characteristics of tunneling, and 70 % showed either an ohmic like or breakdown response, as is shown in figure 8.2 . As discussed in section 2.3.1, the roughness induces a strong Néel coupling through which an independent switch of the two magnetic layers of the MTJ is hindered, revealing no significant magnetoresistance.

The fabrication process of 4-point electrical samples involves multiple delicate steps causing a high drop out ratio. Therefore, we designed 3-point electrical samples to characterize the electrical properties of the nanoscale MTJs, such that the number of process steps could be reduced. The properties of the 3-point electrical nanoscale MTJs can be measured with a conductive atomic force microscope (c-AFM), which is a special application of scanning force microscopy (SFM) techniques.

8.2 Scanning Force Microscopy

In this section, the basic principles of the scanning force microscopy (SFM) technique are described. More detailed information about SFM can be found in literature [122]. A schematic representation of the experimental setup for scanning force microscopy (SFM) measurements is shown in figure 8.4. A sample is placed on an automated approach stage. The approach stage is placed on an active anti-vibration table, to reduce external vibrations. The lateral position of the sample under the tip can be adjusted by two micrometer screws. The exact location of the sample and the tip is verified with a camera that is displaying the image on a monitor.

After the sample approach, the surface of a sample is raster scanned with a tip that is mounted on a flexible cantilever. Due to the interaction force F between the sample and the tip, the cantilever is deflected a distance Δz. The relation between this deflection and the interaction force is given by Hooke's law:

$$F = c\Delta z \quad , \tag{8.1}$$

where c is the force constant of the cantilever, which depends on the material and dimensions of the cantilever.

The deflection is measured by focussing a laser beam on the cantilever. Changes in the orientation of the cantilever are related with changes in the direction of the reflected laser beam, which is monitored with a position sensitive detector (PSD). The laser intensities on the four quadrants of the PSD determines the output signal of the PSD. In order to keep the interaction force constant, the PSD output signal can be used by the feedback system to control the piezo element that is mounted to the cantilever. For measurement control and image analysis, the SFM setup is connected to a computer system.

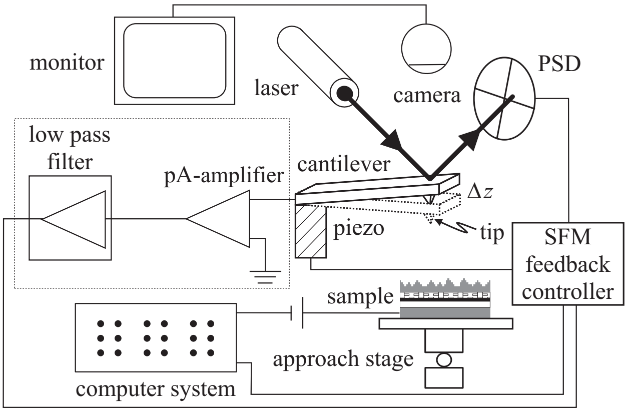

Figure 8.4: Schematic of the experimental setup for scanning force microscopy (SFM). The part enclosed in the dashed frame is the upgrade application module that consists of a pA-amplifier and a low pass filter.

Depending on the distance between the sample and the tip, the interaction can be attractive or repulsive as is shown in figure 8.5. In addition, the different scanning mode regions are indicated in figure 8.5. By providing the setup with a conductive tip and bringing the tip in direct contact with the sample surface, the SFM technique can be utilized for electrical measurements. This type of measurements are called conductive atomic force microscopy (c-AFM).

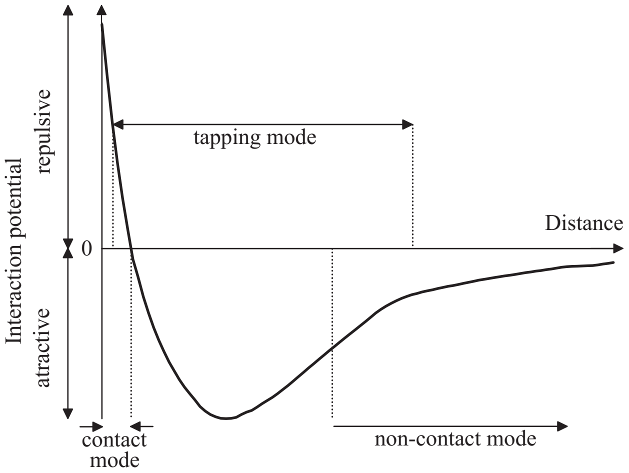

Figure 8.5: Interaction potential diagram as a function of distance between tip and sample, with and without a correction for the capillary force.

8.2.1 Conductive Atomic Force Microscopy

A conductive atomic force microscopy (c-AFM) setup can be used to measure the local electrical transport properties of nanoscale MTJs [123]. The 3-point electrical nanoscale MTJ samples have the following layer sequence: Si(001)/ SiO_x// 50 Å Ta/ 25 Å $Co_{90}Fe_{10}$/ 100 Å IrMn/ 40 Å $Co_{90}Fe_{10}$/ 8 Å Ru/ 40 Å $Co_{90}Fe_{10}$/ 11 Å AlO_x/ 50 Å $Co_{90}Fe_{10}$/ 50 Å Ta. After patterning the bottom electrode, the free $Co_{90}Fe_{10}$ layer of the MTJ stack is etched in a CO/NH_3 plasma using a bilayer resist mask of polymethylmethacrylate (PMMA) and hydrogen silsesquioxane (HSQ). The bilayer resist is dissolved by exposing the samples for 2 days to a methylisobutylketon (MIBK) vapor bath of 118 °C. After that, the samples are rinsed in an ultrasonic bath for 30 minutes in MIBK.

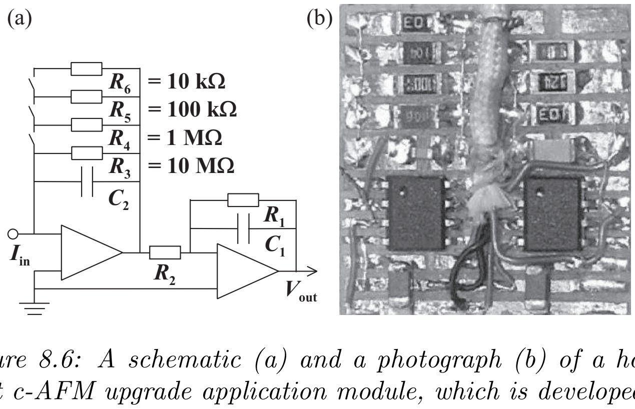

Figure 8.6: A schematic (a) and a photograph (b) of a home-built c-AFM upgrade application module, which is developed for the Solver P47H SFM.

In order to perform a c-AFM measurement, a constant bias voltage is applied to the bottom electrode of the MTJ. The tunnel current through the AlO_x barrier is measured with a conductive tip that has the function of the top electrode of the MTJ. Usable tips for c-AFM are, for example, commercially available doped diamond tips or PtIr coated Si tips. Furthermore, the setup is upgraded with a preamplifier and a low pass filter [124], which is schematically depicted within the dashed frame of figure 8.4. A schematic and a photograph of the home-built upgrade application module that is developed for the Solver P47H SFM[1], is shown in figure 8.6(a) and (b), respectively.

A CDPT-NCHR conductive diamond coated Si tip with a curvature between 200 and 300 nm, a total resistance of < 3 kΩ, and a force constant of approximately 40 N/m is used to calibrate the application module. Various resistances ranging from 10 to 10^7 Ω are measured, the obtained set of curves exhibited a linear response.

The fitting revealed that the Solver P47H c-AFM with the home-built upgrade application module can be applied to measure the electrical properties of nanoscale MTJs. Nevertheless, no reliable electrical transport measurements of nanoscale MTJ samples could be preformed, because of several additional factors that may have influenced our first experiments, such as imaging force, wearing out of the tip, obtaining and maintaining a stable contact between tip and sample, etcetera. Therefore, we employed an alternative c-AFM setup that has already proven its merits.

For the electrical measurements of the local transport properties of the 3-point nanoscale MTJ samples we used a Topometrix EX189902 microscope[2] equipped with a commercial FEMTO upgrade application module. The pA-amplifier of the FEMTO module has an overall amplification of 5 GV/A, and the low pass filter has a bandwidth of 1 kHz. Furthermore, we used a VEECO conductive 20 nm PtIr/ 3 nm Cr coated Si tip with a force constant between 1 and 5 N/m for the electrical measurements.

The nanoscale MTJs have a width w ranging from 50 to 300 nm, and a length to width aspect ratio of 1.5 to 2.5. The MTJs with a width $w > 150$ nm have a rectangular shape and the MTJs of width $w < 150$ nm have an elliptical shape. After locating a nanoscale MTJ, the scan area is reduced to an area of about 1 nm^2 with no irregularities and/or dust particles on the surface of the MTJ. Subsequently, the VEECO tip is brought into contact with the nanoscale MTJs by a manual approach procedure, and a constant bias voltage between -2 and $+2$ V is applied to the bottom electrode of the MTJ. However, no significant change in the output values could be observed.

The 4-point electrical measurements already pointed out the delicacy of the fabrication process, leading to short-circuits or pinholes in the nanometer thin AlO_x barriers. Although identical arguments apply for a failure of the 3-point electrical nanoscale MTJ, in all occasions some output voltage dependency should be observed for an applied bias voltage between -2 and $+2$ V. A reason for the missing bias dependency could be a poor or unstable contact. However, increasing the force during the manual approach procedure mostly induces a tip failure. Another possibility is that the amplifying capability of the FEMTO upgrade application module is not powerful enough. However, the most plausible reason for measuring no significant bias voltage dependency is no electrical contact due to resist remains on the nanoscale MTJ samples that are measured at Bielefeld.

---

[1] Setup is located at the group Physics of Nanostructures, Department of Applied Physics, Eindhoven University of Technology, The Netherlands

[2] Setup is located at the group Thin Films & Nanostructures, Department of Physics, University of Bielefeld, Germany

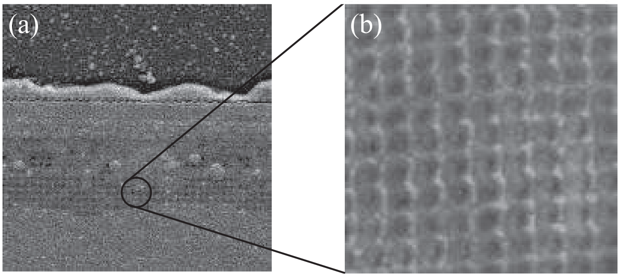

Figure 8.7: An image of the lead of a 3-point nanoscale MTJ samples (a), and a zoom image to confirm that the visible structure is induced by resist remains (b).

This assumption is based on several AFM images of the electrical leads and different nanoscale MTJs samples that displayed a well-defined regular structure. An example of such an image is shown in figure 8.7. Figure 8.7(a) shows the image of the lead of a 3-point nanoscale MTJ sample. The substrate of the sample is dark in the image and the wavy rim of HSQ remains at the edge of the lead is bright due to charging of the HSQ resist. After a thorough MIBK dissolving procedure we expected that no remains of bilayer resist could be encountered.

However, the zoom-in image in figure 8.7(b) shows a well-defined visible structure, which is simply associated with the regular pointillist style of writing a pattern with an electron beam. Furthermore, the size of the features relates to the used spot diameter and the periodicity corresponds to the applied beam step size. Therefore, we cannot equivocate the fact that the nanoscale MTJ samples are still covered with resist remains. As a consequence, no reliable contact between tip and he nanoscale MTJ could be established.

8.3 Conclusions and Outlook

In conclusion, we presented the *I-V* characteristics of nanometer thin AlO_x barriers by applying a voltage over a square MTJ pillar with a surface area of 1 $\mu\mathrm{m}^2$ located at the cross-point of the bottom and top electrode. Although the *I-V* response of the 1 $\mu\mathrm{m}^2$ MTJs showed different characteristics, approximately 30 % of the measured MTJs showed characteristics of tunneling, and 70 % showed either an ohmic like or breakdown response. The conductance showed roughly a parabolic behavior, validating one of the criteria for tunneling. Although the other so-called Rowell criteria are not systematically investigated, the barrier parameters that resulted from fitting the data with the Brinkman formula were close to reported observations in literature. Resistance measurements yielded no significant magnetoresistance for the 1 $\mu\mathrm{m}^2$ MTJs. Roughness at the interfaces induces a strong Néel coupling causing stability decay of the magnetization in the two ferromagnetic layers of the MTJ.

In order to measure the local electrical transport properties of nanoscale MTJs, the Solver P47H scanning force microscopy (SFM) setup is adjusted to perform conductive measurement. The Solver P47H SFM was equipped with a home-built upgrade application module consisting of a pA-amplifier and a low pass filter. However, no reliable electrical transport measurements of nanoscale MTJ samples could be preformed with the Solver P47H c-AFM. Therefore, as an alternative a Topometrix c-AFM setup was employed for the electrical characterization nanoscale MTJs. After the tip was brought into contact with the nanoscale MTJs, and applying a constant bias voltage between -2 and $+2$ V to the bottom electrode of the MTJ, no significant change in the output voltage was observed. From AFM images we concluded that the nanoscale MTJ samples are still covered with resist remains, and as a result no reliable contact between tip and sample could be established.

In future, we will attempt to remove the resist remains by mechanical polishing. In case the attempt will fail, we can remove the resist remains by etching with a focussed ion beam, while monitoring the proces with a scanning electron microscope to protect the nanoscale MTJ for over-etching.

References

[1] S. A. Wolf, D. D. Awschalom, R. A. Buhrman, J. M. Daughton, S. von Molnr, J. M. Roukes, A. Y. Chtcelkanova, and D. M. Treger, *Spintronics: A Spin-Based Electronics Vision for the Future*, Science, **294**, 1488, (2001).

[2] J. D. Livingston, *Driving force: the natural magic of magnets*, Harvard University Press, Cambridge, (1996).

[3] L. Shustek, K. Tashev, M. R. Williams, D. Spicer, J. Clark, and C. Garcia, *Samples from the Collection*, Visible Storage , **Mountain View CA 94043**, Computer History Museum <http://www.computerhistory.org/virtualvisiblestorage>, (2006).

[4] A. Wang and W. D. Woo, *Static Magnetic Storage and Delay Line*, J. Appl. Phys., **21**, 49, (1950).

[5] S. S. P. Parkin, X. Jiang, C. Kaiser, A. Panchula, K. Roche, and M. Samant, *Magnetically Engineered Spintronic Sensors and Memory*, Proceedings of the IEEE, **91**, 661, (2003).

[6] R. P. Hunt, *A Magnetoresistive Readout Transducer*, IEEE Trans. Magn., **7**, 150, (1971).

[7] T. R. McGuire and R. I. Potter, *Anisotropic Magnetoresistance in Ferromagnetic 3d Alloys*, IEEE Trans. Magn., **11**, 1018, (1975).

[8] A. F. Mayadas, J. F. Janak, and A. Gangulee, *Resistivity of Permalloy thin films*, J. Appl. Phys., **45**, 2780, (1974).

[9] M. N. Banisch, J. M. Broto, A. Fert, F. N. V. Dau, F. Petroff, P. Eitenne, G. Creuzet, A. Friederich, and J. Chazelas, *Giant Magnetoresistance of (001)Fe/(001)Cr Magnetic Superlattices*, Phys. Rev. Lett., **61**, 2472, (1988).

[10] G. Binasch, P. Grünberg, F. Saurenbach, and W. Zinn, *Enhanced magnetoresistance in layered magnetic structures with antiferromagnetic interlayer exchange*, Phys. Rev. B, **39**, 4828, (1989).

[11] S. S. P. Parkin, Z. G. Li, and D. J. Smith, *Giant Magnetoresistance in antiferromagnetic Co/Cu multilayers*, Appl. Phys. Lett., **58**, 2710, (1991).

[12] S. S. P. Parkin, K. P. Roche, M. G. Samant, P. M. Rice, R. B. Beyers, R. E. Scheuerlein, E. J. O'Sullivan, S. L. Brown, J. Bucchigano, D. W. Abraham, Y. Lu, M. Rooks, P. L. Trouilloud, R. A. Wanner, and W. J. Gallagher, *Exchange-biased magnetic tunnel junctions and application to nonvolatile magnetic random acces memory*, J. Appl. Phys., **85**, 5828, (1999).

[13] J. Taylor and E. Harris, *Freescale Leads Industry in Commercializing MRAM Technology*, Freescale Semiconductor, Inc., **MR2A16A**, Image Library: Products <http://media.freescale.com>, (2006).

[14] I. Giaever, *Energy Gap in Superconductors Measured by Electron Tunneling*, Phys. Rev. Lett., **5**, 147, (1960).

[15] J. Bardeen, *Tunneling from a Many-Particle Point of View*, Phys. Rev. Lett., **6**, 57, (1961).

[16] P. M. Tedrow and R. Meservey, *Spin-Dependent Tunneling into Ferromagnetic Nickel*, Phys. Rev. Lett., **26**, 192, (1971).

[17] M. Julliere, *Tunneling between ferromagnetic films*, Phys. Lett. A, **54**, 225, (1975).

[18] T. Miyazaki and N. Tezuka, *Giant magnetic tunneling effect in* $Fe/Al_2O_3/Fe$ *junction*, J. Magn. Magn. Mater., **139**, L231, (1995).

[19] J. Moodera, L. Kinder, T. Wong, and R. Meservey, *Large Magnetoresistance at Room Temperature in Ferromagnetic Thin Film Tunnel Junctions*, Phys. Rev. Lett., **74**, 3273, (1995).

[20] W. Oepts, *Spin Dependent Transport in Structured Magnetic Layers*, PhD thesis, Eindhoven University of Technology, The Netherlands, (1999).

[21] S. Tehrani, J. Slaughter, M. Deherrera, B. Engel, N. Rizzo, J. Salter, M. Durlam, R. Dave, J. Janesky, B. Butcher, K. Smith, and G. Grynkewich, *Magnetoresistive Random Access Memory Using Magnetic Tunnel Junctions*, Proceedings of the IEEE, **91**, 703, (2003).

[22] W. J. Gallagher, D. W. Abraham, S. Assefa, S. L. Brown, J. DeBrosse, M. Gaidis, E. Galligan, E. Gow, B. Hughes, J. Hummel, S. Kanakasabapathy, C. Kaiser, M. Lamorey, T. Maffitt, K. Milkove, Y. Lu, J. Nowak, P. Rice, M. Samant, E. O'Sullivan, S. S. P. Parkin, R. Robertazzi, P. Trouilloud, D. Worledge, G. Wright, and S. H. Yang, *Recent Advances in MRAM technology*, Proceedings of the IEEE, **VLSI-TSA-Tech**, 72, (2005).

[23] G. Bertotti, *Hysteresis in Magnetism*, Academic Press, Inc., San Diego, (1998).

[24] P. LeClair, *Fundamental Aspects of Spin Polarized Tunneling*, PhD thesis, Eindhoven University of Technology, The Netherlands, (2002).

[25] S. Gider, B. U. Runge, A. C. Marley, and S. S. P. Parkin, , Science, **281**, 797, (1999).

[26] W. J. Gallagher and S. S. P. Parkin, *Development of the magnetic tunnel junction MRAM at IBM: From first junctions to a 16-Mb MRAM demonstrator chip*, IBM J. Res. & Dev., **50**, 5, (2006).

[27] B. N. Engel, J. Åkerman, B. Butcher, R. W. Dave, M. DeHerrera, M. Durlam, G. Grynkewich, J. Janesky, S. V. Pietambaram, N. D. Rizzo, J. M. Slaughter, K. Smith, J. J. Sun, and S. Tehrani, *A 4-Mb Toggle MRAM Based on a Novel Bit and Switching Method*, IEEE Trans. Magn., **41**, 132, (2005).

[28] W. A. Harrison, *Tunneling from an Independent-Particle Point of View*, Phys. Rev., **123**, 85, (1961).

[29] D. J. Griffiths, *Introduction to Quantum Mechanics*, Prentice Hall International, Inc., Englewood Cliffs, (1994).

[30] J. G. Simmons, *Generalized Formula for the Electric Tunnel Effect between Similar Electrodes Separated by a Thin Insulating Film*, J. Appl. Phys., **34**, 1793, (1963).

[31] W. F. Brinkman, R. C. Dynes, and J. M. Rowell, *Tunneling Conductance of Asymmetrical Barriers*, J. Appl. Phys., **41**, 1915, (1970).

[32] J. C. Slonczewski, *Conductance and exchange coupling of two ferromagnets separated by a tunnel barrier*, Phys. Rev. B, **39**, 6995, (1989).

[33] J. D. Jackson, *Classical Electrodynamics*, John Wiley & Sons, Inc., New York, (1999).

[34] J. A. Osborn, *Demagnetizing Factors of the General Ellipsoid*, Phys. Rev., **67**, 351, (1945).

[35] L. Landau and E. Lifshitz, *On the Theory of the Dispersion of Magnetic Permeability in Ferromagnetic Bodies*, Physik. Z. Sowjetunion, **8**, 153, (1935).

[36] J. W. F. Brown, *The Fundamental Theorem of Fine-Ferromagnetic-Particle Theory*, J. Appl. Phys., **39**, 993, (1968).

[37] A. Hubert and R. Schäfer, *Magnetic Domains - The Analysis of Magnetic Microstructures*, Springer, Berlin, (1998).

[38] R. P. Cowburn and M. E. Welland, *Phase transitions in planar magnetic nanostructures*, Appl. Phys. Lett., **72**, 2041, (1998).

[39] J. W. F. Brown, *Micromagnetics*, John Wiley & Sons, Inc., New York, (1963).

[40] E. C. Stoner and E. P. Wohlfarth, *A Mechanism of Magnetic Hysteresis in Heterogeneous Alloys*, Phil. Trans. Roy. Soc. London, **A240**, 599, (1948).

[41] E. H. Frei, S. Shtrikman, and D. Treves, *Critical Size and Nucleation Field of Ideal Ferromagnetic Particles*, Phys. Rev., **106**, 446, (1957).

[42] A. Aharoni, *Perfect and Imperfect Particles*, IEEE. Trans. Magn., **22**, 478, (1986).

[43] A. Aharoni and S. Shtrikman, *Magnetization Curve of the Infinite Cilinder*, Phys. Rev., **109**, 1522, (1958).

[44] M. J. Donahue and D. G. Porter, OOMMF *Users Guide, version 1.0*, Interagency Report, **NISTIR 6376**, NIST <http://math.nist.gov/oommf>, (1999).

[45] N. A. Usov, C. R. Chang, and Z. H. Wei, *Buckling instability in thin soft elliptical particles*, Phys. Rev. B, **66**, 184431, (2002).

[46] K. J. Kirk, M. R. Scheinfein, J. N. Chapman, S. McVitie, M. F. Gillies, B. R. Ward, and J. G. Tennant, *Role of vortices in magnetization reversal of rectangular NiFe elements*, J. Phys. D., **34**, 160, (2001).

[47] M. Natali, A. Lebib, Y. Chen, I. L. Prejbeanu, and K. Ounadjela, *Configurational anisotropy in square lattices of interacting cobalt dots*, J. Appl. Phys., **91**, 7041, (2002).

[48] J. C. S. Kools, W. Kula, D. Mauri, and T. Lin, *Effect of finite magnetic film thickness on Néel coupling in spin valves*, J. Appl. Phys., **85**, 4466, (1999).

[49] W. H. Meiklejohn and C. P. Bean, *New Magnetic Anisotropy*, Phys. Rev., **102**, 1413, (1956).

[50] H. Ohldag, A. Scholl, F. Nolting, S. Anders, F. U. Hillebrecht, and J. Stöhr, *Spin Reorientaton at the Antiferomagnetic NiO(001) Surface in Response to an Adjacent Ferromagnet*, Phys. Rev. Lett., **86**, 2878, (2001).

[51] D. E. Heim and S. S. P. Parkin, *Magnetoresistive spin valve sensor with improved pinned ferromagnetic layer and magnetic recording system using the sensor*, United States Patent, , US005465185A, (1995).

[52] S. S. P. Parkin, N. More, and K. P. Roche, *Oscillations in Exchange Coupling and Magnetoresistance in Metallic Superlattice Structures: Co/Ru, Co/Cr and Fe/Cr*, Phys. Rev. Lett., **64**, 2304, (1990).

[53] P. Bruno and C. Chappert, *Oscillatory Coupling between Ferromagnetic Layers Separated by a Nonmagnetic Metal Spacer*, Phys. Rev. Lett., **67**, 1602, (1991).

[54] B. C. Min, *Interface engineering of spin-tunel contacts to silicon*, PhD thesis, University of Twente, The Netherlands, (2007).

[55] R. L. Stamps and R. E. Camley, *Magnetization processes and reorientation transition for small magnetic dots*, Phys. Rev. B, **60**, 11694, (1999).

[56] K. Wasa and S. Hayakawa, *Handbook of Sputter Deposition Technology: Principles, Technology and Applications*, Noyes Publications, New Jersey, (1992).

[57] M. Ohring, *The materials Science of Thin Films*, Academic Press, Inc., San Diego, (1992).

[58] K. Knechten, H. J. M. Swagten, B. Koopmans, M. C. M. van de Sanden, and W. J. M. de Jonge, *A Novel Model for Plasma Oxidation of Aluminum*, to be published.

[59] P. LeClair, J. T. Kohlhepp, A. A. Smits, H. J. M. Swagten, B. Koopmans, and W. J. M. de Jonge, *Optical and in situ characterization of plasma oxidized Al for magnetic tunnel junctions*, J. Appl. Phys., **87**, 6070, (2000).

[60] H. G. Tompkins, *A User's Guide to Ellipsometry*, Academic Press, Inc., San Diego, (1993).

[61] D. R. Lide, *CRC Handbook of Chemistry and Physics*, CRC Press, Inc., Boca Raton, (2006).

[62] P. Yeh, *Optical Waves in Layered Media*, John Wiley & Sons, Inc., New York, (1988).

[63] F. L. Pedrotti and L. S. Pedrotti, *Introduction to Optics*, Prentice-Hall International, Inc., Englewood Cliffs, (1993).

[64] R. M. A. Azzam and N. M. Bashara, *Ellipsometry and polarized light*, North-Holland, Oxford, (1979).

[65] A. Smits, *Tunnel Junctions noise and barrier characterization*, PhD thesis, Eindhoven University of Technology, The Netherlands, (2001).

[66] T. Mitsuzuka, K. Matsuda, A. Kamijo, and H. Tsuge, *Interface structures and magnetoresistance in magnetic tunnel junctions*, J. Appl. Phys., **85**, 5807, (1999).

[67] D. Briggs and M. P. Seah, *Practical Surface Analysis by Auger and X-ray Photoelectron Spectroscopy*, John Wiley & Sons, Inc., New York, (1983).

[68] L. C. Feldmann and J. W. Mayer, *Fundamentals of Surface and Thin Film Analysis*, North Holland, Amsterdam, (1986).

[69] P. LeClair, J. T. Kohlhepp, H. J. M. Swagten, and W. J. M. de Jonge, *Interfacial Density of States in Magnetic Tunnel Junctions*, Phys. Rev. Lett., **86**, 1066, (2001).

[70] K. Knechten, P. LeClair, J. T. Kohlhepp, H. J. M. Swagten, B. Koopmans, and W. J. M. de Jonge, *In situ time-resolved optical studies of Al oxidation for magnetic tunnel junctions*, J. Appl. Phys., **90**, 1675, (2001).

[71] K. Knechten, *Plasma Oxidation for magnetic tunnel junctions*, PhD thesis, Eindhoven University of Technology, The Netherlands, (2005).

[72] A. E. T. Kuiper, M. F. Gillies, V. Kottler, G. W. 't Hooft, J. G. M. van Berkum, C. van der Marel, Y. Tamminga, and J. H. M. Snijders, *Plasma oxidation of thin aluminum layers for magnetic spin-tunnel junctions*, J. Appl. Phys., **89**, 1965, (2001).

[73] K. N. Tu, A. M. Gusak, and I. Sobchenko, *Linear rate of grain growth in thin films during deposition*, Phys. Rev. B, **67**, 245408, (2003).

[74] T. Ando, M. Hayashi, S. Iura, K. Yaoita, C. C. Yu, H. Kubota, and T. Miyazaki, *Growth mechanism of thin insulating layer in ferromagnetic tunnel junctions prepared using various oxidation methods*, J. Phys. D., **35**, 2415, (2002).

[75] V. Kottler, M. F. Gillies, and A. E. T. Kuiper, *An in situ x-ray photoelectron spectroscopy study of AlOx spin tunnel barrier formation*, J. Appl. Phys., **89**, 3301, (2001).

[76] C. Y. Chang and S. M. Sze, *ULSI Technology*, McGraw-Hill Companies, Inc., Singapore, (1996).

[77] B. D. Terris and T. Thomson, *Nanofabricated and self-assembled magnetic structures as data storage media*, J. Phys. D, **38**, R199, (2005).

[78] C. L. Dennis, R. P. Borges, L. D. Buda, J. F. Gregg, M. Hehn, E. Jouguelet, K. Ounadjela, I. Petej, I. L. Prejbeanu, and M. J. Thornton, *The defining length scales of mesomagnetism: a review*, J. Phys.: Condens. Matter, **14**, R1175, (2002).

[79] T. H. P. Chang, *Proximity effect in electron-beam lithograhy*, J. Vac. Sci. Technol., **12**, 1271, (1975).

[80] N. Matsui, K. Mashimo, A. Egami, A. Konishi, O. Okada, and T. Tsukada, *Etching characteristics of magnetic materials (Co, Fe, Ni) using CO/NH*$_3$ *gas plasma for hardening mask etching*, Vacuum, **66**, 479, (2002).

[81] R. Hsiao and D. Miller, *Etching of Tantalum in Fluorine-Containing High Density Plasmas*, J. Electrochem. Soc., **143**, 3266, (1996).

[82] M. Sugawara, B. L. Stansfield, S. Handa, K. Fujita, S. Watanabe, and T. Tsukamoto, *Plasma Etching Fundamentals and Applications*, Oxford University Press, Inc., New York, (1998).

[83] A. J. van Roosmalen, J. A. G. Baggerman, and S. J. H. Brader, *Dry Etching for VLSI*, Plenum Press, New York, (1991).

[84] R. Hsiao, *Fabrication of magnetic recording heads and dry etching of head materials*, IBM J. Res. Develop., **43**, 89, (1999).

[85] K. B. Jung, E. S. Lambers, J. R. Childress, S. J. Pearton, M. Jenson, and A. T. Hurst, *High rate dry etching of* $Ni_{0.8}Fe_{0.2}$ *and NiFeCo*, Appl. Phys. Lett., **71**, 1255, (1997).

[86] R. E. Lee, *Microfabrication by ion-beam etching*, J. Vac. Sci. Technol., **16**, 164, (1979).

[87] H. R. Kaufman, J. J. Cuomo, and J. M. E. Harper, *Technology and applications of broad-beam ion sources used in sputtering. Part I. Ion source technology*, J. Vac. Sci. Technol., **21**, 725, (1982).

[88] P. G. Glöersen, *Ion-beam etching*, J. Vac. Sci. Technol., **12**, 28, (1975).

[89] K. B. Jung, H. Cho, Y. B. Hahn, D. C. Hays, E. S. Lambers, Y. D. Park, T. Feng, J. R. Childress, and S. J. Pearton, *Comparison of* Cl_2*/He,* Cl_2*/Ar,and* Cl_2*/Xe Plasma Chemistries for Dry Etching of NiFe and NiFeCo*, J. Electrochem. Soc., **146**, 1465, (1999).

[90] H. Cho, K. P. Lee, K. B. Jung, S. J. Pearton, J. Marburger, F. Sharifi, Y. B. Hahn, and J. R. Childress, *Corrosion-free dry etch patterning of magnetic random access memory stacks: Effects of ultraviolet illumination*, J. Appl. Phys., **87**, 6397, (2000).

[91] F. C. M. J. M. van Delft, *Structuring magnetic thin films by means of plasma etching*, J. Magn. Magn. Mater., **140**, 2203, (1995).

[92] M. S. P. Andriesse, E. van der Drift, and W. G. Sloof, *High speed, dry etching of Fe for integration of magnetic devices in microelectronics*, J. Vac. Sci. Technol. B, **19**, 2901, (2001).

[93] M. S. P. Andriesse, T. Zijlstra, and E. van der Drift, *High speed anisotropic dry etching of CoNbZr for next generation magnetic reconding*, J. Vac. Sci. Technol. B, **18**, 3462, (2000).

[94] M. J. Vasile and C. J. Mogab, *Chemically assisted sputter etching of peramlloy using CO or* Cl_2, J. Vac. Sci. Technol. A, **4**, 1841, (1986).

[95] I. Nakatani, *Ultramicro Fabrications on Fe-Ni Alloys Using Electron-Beam Writing and Reactive-Ion Etching*, IEEE Trans. Magn., **32**, 4448, (1996).

[96] K. B. Jung, J. Hong, H. Cho, S. Onishi, D. Johnson, Y. D. Park, J. R. Childress, and S. J. Pearton, *Parametric Study of NiFe and NiFeCo High Density Plasma Etching Using CO/*NH_3, J. Electrochem. Soc., **146**, 2163, (1999).

[97] A. S. Orland and R. Blumenthal, *Metal etching with organic based plasmas. II. CO/*NH_3 *plasmas*, J. Vac. Sci. Technol. B, **23**, 1597, (2005).

[98] B. B. Schwartz and S. Foner, *Superconductor Applications: SQUIDs and Machines*, Plenum Press, New York, 1977.

[99] M. M. H. Willekens, *Giant MagnetoResistance in Spin Valves*, PhD thesis, Eindhoven University of Technology, 1997.

[100] M. A. Bongers, *Beschrijving van de Quantum Design MPMS-5S SQUID-Magnetometer & Onderzoek naar de magnetische eigenschappen van granulaire Co/Ag multilagen*, Master's thesis, Eindhoven University of Technology, (1995).

[101] A. Barone and G. Paternò, *Physics and Applications of the Josephson Effect*, John Wiley & Sons, Inc., New York, (1982).

[102] N. W. E. McGee, *The Magneto-Optical Kerr Effect: Theory, Measurement and Application*, Master's thesis, Eindhoven University of Technology, (1991).

[103] S. S. P. Parkin and D. Mauri, *Spin Engineeing: Direct detemination of the Rudeman-Kittel-Kasuya-Yosida far-field range function in ruthenium*, Phys. Rev. B, **44**, 7131, (1991).

[104] W. Wernsdorfer, K. Hasselbach, A. Sulpice, A. Benoit, J. E. Wegrowe, L. Thomas, B. Barbara, and D. Mailly, *Dynamical measurement of domain-wall nucleation and annihilation in individual amorphous Co particles*, Phys. Rev. B, **53**, 3341, (1996).

[105] H. A. M. van den Berg, *Domain structures in soft-ferromagnetic thin-film objects*, J. Appl. Phys., **61**, 4194, (1987).

[106] K. J. Kirk, J. N. Chapman, S. McVitie, P. R. Aitchison, and C. D. W. Wilkinson, *Switchng of nanoscale magnetic elements*, Appl. Phys. Lett., **75**, 3683, (1999).

[107] E. Girgis, J. Schelten, J. Shi, J. Janesky, S. Tehrani, and H. Goronkin, *Switching characteristics and magnetization vortices of thin-film cobalt in nanometer-scale patterned arrays*, Appl. Phys. Lett., **76**, 3780, (2000).

[108] L. J. Heyderman, H. H. Solak, C. David, D. Atkinson, R. P. Cowburn, and F. Nolting, *Arrays of nanoscale magnetic dots: Fabrication by x-ray interference lithography and characterization*, Appl. Phys. Lett., **85**, 21, (2004).

[109] J. A. Johnson, M. Grimsditch, V. Metlushko, P. Vavassori, B. Ilic, P. Neuzil, and R. Kumar, *Magneto-optic Kerr effect investigation of cobalt and permalloy nanoscale dot arrays: Shape effects on magnetization reversal*, Appl. Phys. Lett., **77**, 4410, (2000).

[110] Y. Zheng and J. G. Zhu, *Switching field variation in patterned submicron magnetic film elements*, J. Appl. Phys., **81**, 5471, (1997).

[111] J. Gadbois and J. G. Zhu, *The Effect of End and Edge Shape on the Performance of Pseudo-Spin Valve Memories*, IEEE Trans. Magn., **34**, 1066, (1998).

[112] R. E. Dunin-Borkowski, M. R. McCartney, D. J. Smith, and M. R. Scheinfein, *Switching asymmetries in closely coupled magnetic nanostructure arrays*, Appl. Phys. Lett., **75**, 2641, (1999).

[113] M. T. Bryan, D. Atkinson, and R. P. Cowburn, *Experimantal study of the influence of the edge roughness on magnetization switching in Permalloy nanostructures*, Appl. Phys. Lett., **85**, 3510, (2004).

[114] H. Kubota, Y. Ando, T. Miyazaki, G. Reiss, H. Brückl, W. Schepper, J. Wecker, and G. Gieres, *Size dependence of swichting field of magnetic tunnel junctions down to 50 nm scale*, J. Appl. Phys., **94**, 2028, (2003).

[115] H. Kubota, G. Reiss, H. Brückl, W. Schepper, J. Wecker, and G. Gieres, *Magnetoresistance and Dipole Shift of Ultrasmall Magnetic Tunnel Junctions Characterized by Conducting Atomic Force Microscopy*, Jpn. J. Appl. Phys., **41**, L180, (2002).

[116] K. B. Jung, J. Marburger, F. Sharifi, Y. D. Park, E. S. Lambers, and S. J. Pearton, *Long term stability of dry etched magnetoresistive random access memory elements*, J. Vac. Sci. Technol. A, **18**, 268, (2000).

[117] H. I. Smith, *Fabrication Techniques for Surface-Acoustic-Wave and Thin-Film Optical Devices*, Proceedings of the IEEE, **62**, 1361, (1974).

[118] K. B. Jung, H. Cho, Y. B. Hahn, E. S. Lambers, J. A T. Hurst, Y. D. Park, and S. J. Pearton, *Relative merits of Cl_2 and CO/NH_3 plasma chemistries for dry etching of magnetic random access memory device elements*, J. Appl. Phys., **85**, 4788, (1999).

[119] J. M. Rowell, W. L. McMillan, and W. L. Feldmann, *Phonon Emission and Self-Energy Effects in Normal-Metal Tunneling*, Phys. Rev., **180**, 658, (1969).

[120] B. J. Jönsson-Åkerman, R. Escudero, C. Leighton, S. Kim, I. K. Schuller, and D. A. Rabson, *Reliability of normal-state current-voltage characteristics as an indicator of tunnel-junction barrier quality*, Appl. Phys. Lett., **77**, 1870, (2000).

[121] R. D. Parks, *Superconductivity*, Marcel Dekker, Inc.,, New York, (1969).

[122] D. A. Bonnell, *Scanning Probe Microscopy and Spectroscopy: Theory, Techniques and Applications*, Wiley-VCH, Inc., New York, (2001).

[123] V. D. Costa, F. Bardou, C. Béal, Y. Henry, J. P. Bucher, and K. Ounadjela, *Nanometric cartography of tunnel current in metal-oxide junctions*, J. Appl. Phys., **83**, 6703, (1998).

[124] A. Olbrich, B. Ebersberger, and C. Boit, *Conducting atomic force microscopy for nanoscale electrical characterization of thn SiO_2*, Appl. Phys. Lett., **76**, 3780, (2000).

Summary

The rapidly growing field of spintronics has recently attracted much attention. Spintronics is electronics in which the spin degree of freedom has been added to conventional charge-based electronic devices. A magnetic tunnel junction (MTJ) is an example of a spintronic device. MTJs consist of two ferromagnetic layers separated by a thin insulating barrier. The tunnel current that flows through the barrier depends on the relative alignment of the magnetization in the ferromagnetic layers. As a consequence of this dependence, the MTJ exhibits two different resistance values that distinguish a logical '0' and a logical '1', corresponding to anti-parallel and parallel magnetization.

Due to these two distinct states, the MTJs can be used as magnetic memory elements, and serve as bits for information storage in magnetic random access memories (MRAMs). MRAMs can lead to instant-on computers and longer battery lifetimes for mobile devices, which gives MRAMs the potential to replace the current RAM technologies. However, for the current RAM technologies to be replaced by MRAMs, the dimensions of the MTJs have to decrease to sub-100 nm in order to achieve a high enough areal density and to match the semiconductor technology. Therefore, the research in this Thesis aims at fabricating sub-100 nm MTJs and investigating the influence of the reduced dimensions on the modification of magnetic and electronic properties.

The MTJ is incorporated in an engineered multilayer stack to promote stability and reproducibility of the magnetic and electric response of the MTJ. For the structuring of these layers, we have used top-down nanofabrication techniques to produce the sub-100 nm MTJs. For MTJs with a surface area of less than 0.01 μm^2, the Al_2O_3 barrier has an approximate thickness of a nanometer to ensure an appropriate tunnel current. Therefore, we have concentrated on the plasm oxidation of sub-nm thin Al layers to produce Al_2O_3 barriers.

We have shown that over-oxidation of sub-nm thin Al_2O_3 barriers of MTJs can be observed in real-time using *in situ* differential ellipsometry measurements. The change in ellipsometry signal of Al layers grown on CoFe films, is proportional to the amount of oxidized metallic material. As a result, the derivative of this signal is a direct measure of the oxidation rate. Further analysis of this oxidation rate allowed us to determine the onset of the CoFe oxidation. We have found the onset to be proportional to the deposited Al layer thickness. The amount of CoO determined from *in situ* X-ray Photoelectron Spectroscopy data on identical samples is found to be proportional to that obtained from ellipsometry.

In short, this means that the point in time on which over-oxidation starts can be precisely determined. This is a critical necessity in producing exact, well-functioning MTJs.

We have used electron beam (EB) lithography to pattern the sub-100 nm features. With EB lithography features of only a few nanometer in size can be defined, hence EB lithography enables the exploration of the fundamental boundaries of magnetic and electric scaling properties. For the structuring of large-area samples with ultra-dense arrays of sub - 100 nm MTJs the throughput is limited because of the sequential writing process. However, with the developed special high-speed EB writing strategy we could pattern a sample area of 16 mm^2 with ultra-dense arrays of sub - 100 nm elliptical features in 10 minutes. The strategy is employed to define the pattern of hard Ta masks with sub-100 nm features. The Ta masks are etched at -50 °C in a SF_6/O_2 plasma to an etch depth that can be controlled with nanometer precision. Ar^+ ion beam milling is used to transfer the pattern and to produce dense arrays of sub - μm MTJs.

Insight in the magnetic switching behavior of nanoscale MTJs as a function of the size, shape and thickness is vital for MRAM application. Especially, the collective properties of high areal density arrays of MTJs are of interest, because magnetostatic coupling mechanisms between elements can be a limiting factor for applications. In order to understand the effects of geometry and coupling mechanisms, the switching of 5 nm thick polycrystalline nanoscale Co dots is examined using SQUID measurements and the switching of sub - μm MTJs is studied with MOKE measurements. An array consists of approximately 10^8 elements with a width ranging from 50 to 300 nm, and a length to width aspect ratios of 1.5 to 2.5, arranged on a rectangular lattice.

The measured switching fields of the Co dots and MTJs were low compared to predictions using the Stoner-Wohlfarth model. The deviations of the Stoner-Wohlfarth behavior could be explained in term of interdot coupling and edge roughness. Comparison with the outcome of OOMMF simulation of the switching of a single dot revealed that the interdot coupling has a major influence on the magnetic switching behavior of arrays of nanoscale magnetic elements. This implies that for the feasibility of ultra-high areal density arrays of nanoscale MTJs for information storage new strategies are needed. For example, a more complex toggle MTJ multilayer stacks can be used for the nanostructuring of sub - μm MTJs.

Faceting of the etch mask due to physical sputtering of the mask material is a problem during deep etching of ultra-high bit density arrays of sub - μm MTJs for MRAMs. Besides that, chlorinated etch residues can reduce the magnetization of patterning magnetic materials substantially, and therefore constitutes a considerable concern. To get more insight into the magnetization losses, CoFeB dots were etched in a high ion density Cl_2-based plasma with a width ranging from 0.3 to 6.4 μm. The magnetic properties of the CoFeB dots were measured by SQUID magnetometry. The sub-μm CoFeB dots showed significant magnetization reductions, despite H_2O rinsing. Scanning electron microscopy (SEM) studies revealed that etching in a Cl_2-based plasma caused faceting of the masks, leading to sloped sidewalls. SEM pictures were used to determine the geometric volume which was compared to the effective magnetic volume resulting from the magnetometry measurements. The SEM data are in good agreement with the magnetometry data, and a chloride penetration depth of only a few nanometer could be derived, indicating that the postetch rinsing is sufficient to prevent considerable corrosion of the CoFeB dots. This means that the chlorinated etch residues could be removed from the samples, without severely effecting the magnetic properties.

The I-V characteristics of nanometer thin AlO_x barriers are measured by applying a voltage over a 1×1 μm^2 square MTJ pillar located at the cross-point of the bottom and top electrode. The I-V response of the MTJs showed in principle three different characteristics, that is an ohmic like response, a response resembling breakdown, and a tunneling response. Approximately 30 % of the measured 32 MTJs showed a tunneling response and had a resistance-area product between approximately 20 and 50 k$\Omega\mu$m^2. Furthermore, the conductance showed roughly a parabolic behavior implying an asymmetrical barrier. As a consequence, we used the Brinkman formula to fit the experimental data. The fits yielded average barrier heights between 1.2 and 2.3 eV, and an asymmetry parameter ranging from 0.3 to 0.8 eV, which are close to reported observations in literature.

Resistance measurements yielded no significant magnetoresistance for the 1 μm^2 MTJs. Probably, as a consequence of interface roughnesses, a strong Néel coupling originates, through which an independent switching of the two magnetic layers of the MTJ is hindered.

As an alternative electrical characterization technique, the conductive atomic force microscopy (c-AFM) technique can used to measure the local electrical transport properties of nanoscale MTJs. We have explored this c-AFM technique and performed I-V measurements by applying a constant bias voltage to the bottom electrode and measuring the tunnel current through the barrier. However, due to resist remains no significant bias voltage dependency was observed.

Samenvatting

Spintronica is een snelgroeiend onderzoeksgebied en staat hierdoor recentelijk zeer in de belangstelling. Spintronica is elektronica waarbij aan de conventionele, op lading gebaseerde elektronische apparaten, de vrijheidsgraad van de spin is toegevoegd. Wat er dan ontstaat is een spintronisch apparaat, zoals bijvoorbeeld een magnetische tunneljunctie (MTJ). Deze MTJs bestaan uit twee ferromagnetische lagen die van elkaar gescheiden zijn door een dunne, isolerende barrière. De tunnelstroom die door de barrière loopt is afhankelijk van de relatieve richting van de magnetisatie in de ferromagnetische lagen. Als gevolg van deze afhankelijkheid heeft een MTJ twee verschillende weerstanden die onderscheid maken tussen een logische ‘0’ en een logische ‘1’, hetgeen correspondeert met een anti-parallelle en parallelle magnetisatie.

Door deze twee specifieke toestanden kunnen MTJs gebruikt worden als geheugenelementen en daardoor dienen als bits voor informatieopslag in Magnetische Random Access Memories (MRAMs). MRAMs maken het mogelijk instant-on computers te ontwikkelen en kunnen daarnaast de levensduur van batterijen voor mobiele apparaten aanzienlijk verlengen. Deze toepassingsmogelijkheden geven MRAMs de potentie om de huidige RAM technologieën te vervangen. Echter, randvoorwaarde hiervoor is wel dat de dimensies van de huidige MTJs verkleind moeten worden tot sub - 100 nm, zodat een oppervlaktedichtheid bereikt kan worden die hoog genoeg is en om aan te sluiten bij de huidige halfgeleider technologie. Vandaar dat het onderzoek in dit proefschrift gericht is op het fabriceren van sub - 100 nm MTJs en het bestuderen van de gevolgen van de gereduceerde dimensies voor de magnetische en elektrische eigenschappen.

Om de stabiliteit en reproduceerbaarheid van de magnetische en elektrische respons te promoten, zijn de MTJs in gebed in een stapel van magnetisch geëngineerde MTJ multilagen. Voor de structurering van deze lagen hebben we top-down nanofabricatietechnieken gebruikt om nanometer-schaal MTJs te produceren. MTJs met een oppervlakte van minder dan 0.01 μm^2 moeten een dikte van de Al_2O_3 barrière hebben van ongeveer een nanometer, om te zorgen voor een geschikte tunnelstroom. Vandaar dat we ons gericht hebben op de plasma oxidatie van sub - nm dikke Al lagen voor de productie van Al_2O_3 barrières. We hebben laten zien dat over-oxidatie van sub - nm dunne Al_2O_3 barrières van MTJs in real-time geobserveerd kan worden door gebruik te maken van *in situ* differentiële ellipsometrie metingen. De verandering in het ellipsometrie signaal van lagen Al gegroeid op CoFe lagen, is proportioneel met de hoeveelheid geoxideerd metallisch materiaal. Het gevolg hiervan is dat de afgeleide van dit signaal een directe maat is voor de oxidatie snelheid. Een nadere analyse van de oxidatie snelheid bood ons de gelegenheid om de onset van de CoFe oxidatie te bepalen. We hebben gevonden dat de onset proportioneel is met de gedeponeerde dikte van de Al laag. De met *in situ* X-ray Photoelectron Spectroscopy bepaalde hoeveelheid CoO van identieke samples bleek evenredig met de hoeveelheid die verkregen was uit de ellipsometry metingen.

In het kort betekent dit dat het tijdstip waarop de over-oxidation begint precies bepaald kan worden. Dit is een essentieel in het produceren van exacte, goed functionerende MTJs.

We hebben elektronen bundel (EB) lithografie gebruikt om sub - 100 nm structuren te patroneren. Met EB lithografie is het mogelijk om structuren te definiëren van slecht een paar nanometer, vandaar dat EB lithografie het mogelijk maakt om de fundamentele grenzen van het schalen voor de magnetische en elektrische eigenschappen te verkennen. Echter de doorvoer voor de structurering van grootte-oppervlakte samples met ultra hoge oppervlaktedichtheid matrices met sub - 100 nm MTJs is beperkt door het seriële schrijf proces. Maar met de speciaal ontwikkelde hoge-snelheid EB schrijf strategie is het mogelijk om een sample oppervlak van 16 mm^2 in 10 minutes te patroneren met ultra hoge oppervlaktedichtheid matrices die sub - 100 nm elliptische structuren bevatten. De strategie is gebruikt om het patroon van het harde Ta masker te definiëren met sub - 100 nm structuren. De Ta maskers zijn bij -50 °C geëtst in een SF_6/O_2 plasma tot een ets diepte die op nanometer precisie gecontroleerd kan worden. Middels het frezen met een Ar^+ ionen bundel is het patroon overgebracht om zodoende hoge oppervlaktedichtheid matrices met sub - 100 nm MTJ te produceren.

Inzicht in het magnetische switch gedrag van nanometer-schaal MTJs als functie van de grootte, vorm en dikte is van wezenlijk belang voor MRAM toepassingen. De collectieve eigenschappen van hoge dichtheid matrices van MTJs zijn met name interessant, omdat magnetostatische koppelingsmechanismen tussen elementen een beperkende factor kunnen zijn voor toepassingen. Om inzicht te verkrijgen in de effecten van de geometrie en de koppelingsmechanismen, is het switchen van 5 nm dikke polycrystalline Co dotjes bestudeerd door SQUID metingen te gebruiken. Het switchen van de sub - μm MTJs is onderzocht met MOKE metingen. Een matrix bestaat uit ongeveer 10^8 elementen met een breedte tussen de 50 en 300 nm, en een lengte tot breedte verhouding variërend van 1.5 tot 2.5, welke gerangschikt zijn op een rechthoekig rooster.

De gemeten switch velden van de Co dotjes en de MTJs waren laag in vergelijking met de door het Stoner-Wohlfarth model voorspelde waarde. De afwijkingen van het Stoner-Wohlfarth gedrag konden verklaard worden in termen van de interdot koppeling en rand ruwheden. Een vergelijking met de resultaten van OOMMF simulaties van het switchen van een enkele dot toonde aan dat de interdot koppeling een substantiële invloed heeft op het magnetische switch gedrag van matrices met nanoscale magnetische elementen. Voor de haalbaarheid van ultra hoge oppervlaktedichtheid matrices met sub - μm MTJs voor informatieopslag betekent dit dat nieuwe strategieën noodzakelijk zijn.

De verwering van het ets masker als gevolg van het fysisch sputteren van masker materiaal is probleem tijdens het etsen van ultra hoge bit dichtheid matrices van sub - 0.01 μm^2 MTJs voor MRAMs. Daarnaast kan de magnetisatie van het gestructureerde magnetische material aanzienlijk gereduceerd worden door gechloreerde ets resten, hetgeen een behoorlijk probleem kan vormen. Om meer inzicht te krijgen in de afname in magnetisatie zijn CoFeB dotjes met een breedte variërend van 0.3 tot 6.4 μm geëtst in een hoge ionen dichtheid Cl_2-gebaseerd plasma. De magnetische eigenschappen van de CoFeB dotjes zijn gemeten met SQUID magnetometry. De sub-μm CoFeB dotjes vertoonde een significante reductie van de magnetisatie, ondanks het naspoelen met H_2O. Een scanning elektronen microscopy (SEM) studie openbaarde dat het etsen in een Cl_2-gebaseerd plasma verwering van het ets masker veroorzaakte, met hellende zijkanten tot gevolg. SEM afbeeldingen zijn gebruikt om het geometrische volume te bepalen en deze te vergelijken met het effectieve magnetische volume dat uit de magnetometry metingen naar voren kwam. De SEM data waren in goede overeenstemming met de magnetometry data en een chloride indring diepte van slechts een paar nanometer kon worden afgeleid, wat wil zeggen dat het spoelen met H_2O na het etsen voldoende is om aanzienlijke corrosie van de CoFeB dotjes te voorkomen. Dit betekent dat de gechloreerde ets resten van de samples verwijderd konden worden, zonder de magnetische eigenschappen ernstig aan te tasten.

De I-V karakteristieken van nanometer dunne AlO_x barrières zijn gemeten door een spanning aan te brengen over een 1×1 μm^2 vierkant MTJ pilaartje, gelocaliseerd op het kruispunt van de onder- en bovenelektrode. De I-V respons van MTJ vertoonde in principe drie verschillende karakteristieken, namelijk een ohms-gelijkende response, een respons die overeenkwam met het kapot gaan van de MTJ, en een tunneling respons. Circa 30 % van de 32 gemeten MTJs liet een tunneling response zien en had een weerstand-oppervlakte product ongeveer tussen de 20 and 50 k$\Omega\mu$m^2. Verder vertoonde de geleiding ruwweg een parabolisch gedrag, wat een asymmetrische barrière impliceert. Met als gevolg dat we de Brinkman formule gebruikt hebben om de experimentele data te fitten. De fits leverde een gemiddelde barrière hoogte op tussen de 1.2 en 2.3 eV V en een asymmetry parameter van 0.3 tot 0.8 eV, hetgeen sterk overeenkomt met de observaties in de literatuur.

Weerstand metingen leverde geen significante magnetoweerstand op voor de 1 μm^2 vierkante MTJs. Waarschijnlijk ontstaat er als gevolg van interface ruwheden een sterke Néel koppeling, waardoor het onafhankelijk switchen van de twee ferromagnetische lagen gehinderd wordt.

De geleidende atomic force microscopy (c-AFM) techniek kan als alternatieve elektrische karakteriseringstechniek gebruikt worden om lokaal de elektrische transport eigenschappen van de sub-μm MTJs te meten. We hebben de c-AFM technique verkend en hebben I-V metingen uitgevoerd door een constante bias spanning op de onder electrode aan te brengen en de tunnel stroom door de barrière te meten. Echter, doordat de sub-μm MTJ samples nog steeds bedekt zijn met resist resten kon geen significante spanningsafhankelijkheid waargenomen worden.

Nomenclature

Variables

Δ : amount of oxidized material
ϕ : angle
ω : angular frequency
K : anisotropy constant
$\Delta\phi$: asymmetry parameter
ϕ : barrier height
k_B : Boltzmann constant
C : capacitance
A : collisions frequency factor
$\tilde{n}$: complex index of refraction
T_C : Curie temperature
I : current
$\vec{\vec{\mathcal{N}}}$: demagnetizing tensor
$\rho(E)$: density of states
$(\alpha_x,\, \alpha_y,\, \alpha_z)$: direction cosines of the magnetization
e : electron charge
m : electron mass
$\Psi(x)$: electron wave function
I : ellipsometry signal
E : energy
Λ : exchange length
A : exchange stiffness
κ : extinction coefficient
α : facet angle
$f(E)$: Fermi-Dirac distribution function
E_F : Fermi level
β : film phase thickness
Φ : flux
f : frequency
r : Fresnel reflection coefficient
t : Fresnel transmission coefficient
κ : imaginary part of the wave vector
i : index number
n : index of refraction
i : integer
j : integer

L : inductance
l : length
$\vec{H}$: magnetic field
μ : magnetic moment
σ_{S} : magnetic surface charge density
ρ_{V} : magnetic volume charge density
$\vec{M}$: magnetization
$\vec{m}$: magnetization vector of unit length
ξ : monotonically increasing function of the aspect ratio
M : mutual inductance
n : number
n_w : number of dots
N : number of states
τ : onset time of the over oxidation
ε : penetration depth
μ_0 : permeability
$\hbar$: Planck's constant divided by 2π
P : polarization
P : probability
R : process rate
R : resistance
δ : rim width
h : roughness height
λ : roughness wavelength
M_{s} : saturation moment
Φ_{D} : scalar potential of the demagnetizing field
Δx : shifted distance
$a \geq b \geq c$: semi-axes a, b, and c of general ellipsoid
$\downarrow$: spin-down
$\uparrow$: spin-up
T : temperature
d : thickness
Δd : thickness increase
t : time
R : total reflection coefficient
$|M_{12}|$: transition matrix element
J_V : tunnel current density
$\vec{e}_x$: unit vector along the x-axis
$\vec{e}_y$: unit vector along the y-axis
V : voltage
V : volume
$\delta x \delta y \delta z$: volume element
λ : wavelength
$\vec{k}$: wave vector
w : width
ϕ : work function
x : x-direction
y : y-direction
z : z-direction

Acronyms

AMR : anisotropic magnetoresistance
AF : antiferromagnetic
AAF : artificial antiferromagnet
AFM : atomic force microscope
BBS : beam step size
CMOS : complementary metal-oxide-semiconductor
DOS : density of states
EB : electron beam
ES : ellipsometry signal
EB : exchange bias
FM : ferromagnetic
GMR : giant magnetoresistance
HSQ : hydrogen silsesquioxane
ICP : inductively coupled plasma
IPA : isopropyl alcohol
MOKE : Magneto-Optical Kerr Effect
MR : magnetoresistance
MRAM : magnetic random access memory
MTJ : magnetic tunnel junction
OOMMF : Object-Oriented MicroMagnetic Framework
PGMA : propyleneglycol monomethyl ether acetate
PMMA : polymethylmethacrylate
RKKY : Ruderman, Kittel, Kasuya, and Yosida
SEM : scanning electron microscopy
SQUID : Superconducting Quantum Interference Device
TMR : tunnel magnetoresistance
WKB : Wentzel, Kramers, and Brillouin
XPS : x-ray photoelectron spectroscopy

Elements

Al : Aluminium
Ar : Argon
B : Boron
C : Carbon
Cl : Chlorine
Cr : Chromium
Co : Cobalt
Cu : Copper
F : Fluorine
Ge : Germanium
He : Helium
H : Hydrogen
Fe : Iron
Ir : Iridium
Pb : Lead
Mg : Magnesium
Mn : Manganese
Ni : Nickel
N : Nitrogen
O : Oxygen
Ru : Ruthenium
Si : Silicon
S : Sulfur
Ta : Tantalum
Ti : Titanium
W : Tungsten

List of Publications & Presentations

Publications

C. G. C. H. M. Fabrie, K. Knechten, J. T. Kohlhepp, H. J. M. Swagten, B. Koopmans, and W. J. M. de Jonge, *Real-time monitoring of plasma oxidation dynamics of subnanometer* Al_2O_3 *barriers for magnetic tunnel junctions*, Appl. Phys. Lett., **88**, 031909, (2006).

C. G. C. H. M. Fabrie, J. T. Kohlhepp, H. J. M. Swagten, B. Koopmans, and W. J. M. de Jonge, *Conversion from Al to* Al_2O_3 *of subnanometer barriers for magnetic tunnel junctions monitored in real time*, J. Appl. Phys., **99**, 08T303, (2006).

C. G. C. H. M. Fabrie, J. T. Kohlhepp, H. J. M. Swagten, B. Koopmans, M. S. P. Andriesse, and E. van der Drift, *Magnetization losses in submicrometer CoFeB dots etched in a high ion density* Cl_2*-based plasma*, J. Vac Sci. Technol. B, **24**, 2627, (2006).

Presentations

C. G. C. H. M. Fabrie, J. T. Kohlhepp, H. J. M. Swagten, B. Koopmans, M. S. P. Andriesse, A. J. van Run, and E. van der Drift, *Patterning Ultra-High Bit Densities by Large-Area Electron Beam Lithography*, NanoNed MicroNed Symposium II, Eindhoven, Netherlands, (16 Nov - 17 Nov 2006).

C. G. C. H. M. Fabrie, J. T. Kohlhepp, H. J. M. Swagten, B. Koopmans, M. S. P. Andriesse, A. J. van Run, and E. van der Drift, *Hard Mask Fabrication for Patterning Ultra-High Bit Densities by Large-Area Electron Beam Lithography*, 10th Joint MMM/Intermag Conference, Baltimore, Maryland, United States, (7 Jan - 11 Jan 2007).

Dankwoord

Mijn promotieonderzoek en het daaruit voortvloeiende proefschrift is mede tot stand gekomen door de hulp die ik van vele mensen heb mogen ontvangen. Zonder iemand te kort te willen doen, wil ik een aantal van deze mensen met naam bedanken.

Allereerst wil ik mijn promotoren Henk Swagten en Bert Koopmans bedanken voor de dagelijkse begeleiding. Zij hebben mij de mogelijkheid geboden de richting van mijn onderzoek binnen de gestelde doelen voor een groot deel zelf te bepalen. Tegelijkertijd hebben zij met hun kritische opmerkingen voor voldoende bijsturing gezorgd waardoor ik alert bleef om de gekozen richtingen tot een goed einde te brengen. Cruciaal voor het werk beschreven in dit proefschrift is de bijdrage geweest van mijn copromotor Emile van der Drift. Hij heeft mij wegwijs gemaakt op het gebied van de nanofabricatie technieken en gezorgd voor de beschikbaarheid van de cleanroom faciliteiten van het Kavli Institute of Nanoscience in Delft.

Naast Emile wil ik ook Mischa Andriesse bedanken voor de hulp die hij geboden heeft bij de nanostructurering van de magnetische multilagen. Verder ben ik Anja van Langen en Arnold van Run dankbaar voor hun bijdrage bij de ontwikkeling van de speciaal ontwikkelde hoge-snelheid elektronen bundel schrijf strategie. Ook Roel Mattern wil ik bedanken voor het dienen als vraagbaak voor chemische problemen en Marc Zuiddam voor de vers gezette koffie tijdens de pauzes. Daarnaast wil ik Gilles Gobreau, Marco van der Krogt en Bifeng Rong niet onvernoemd laten.

De nauwe samenwerking met het Kavli Institute of Nanoscience is mede mogelijk gemaakt dankzij de financiële steun van NanoNed, een nanotechnologie programma van het Nederlandse Ministerie van Economische Zaken. Binnen het NanoNed kader heb ik ook gebruik kunnen maken van de cleanroom faciliteiten van het MESA$^+$ Institute for Nanotechnology in Enschede.

I would like to express my gratitude to Byoung-Chul Min, who advised and assisted my with the Ar$^+$ ion milling of arrays of sub-μm MTJs. Also, I gladly like to thank Byoung-Chul's wife, Kyung-Eun for the nice Korean food she cooked when I visited the NanoElectronics group of the University of Twente. Daarnaast wil ik Johnny Sanderink bedanken voor de verkennende experimenten met de gefocusseerde ionen bundel en het frezen van de referentie samples met een Ar$^+$ ionen bundel. Furthermore, for the warm reception I wish to thank, Tamalika Banerjee, Mercy Mathews, Rajesh Ramaneti, Ivan Vera Marún, Martin Siekman, Thijs Bolhuis, and the other members of the NanoElectronics group.

Ook andere samenwerkingsverbanden hebben bijgedragen tot een beter inzicht in de gevolgen en mogelijkheden van de nanostructurering van de magnetische multilagen. Binnen deze context wil ik Hans Boeve van Philips Research bedanken voor zijn hulp bij het bepalen van de geschikte materialen voor de stapel van magnetisch geëngineerde MTJ

multilagen. Besides that, I would like to express my appreciation to Daniele Pullini of Fiat Research Centre for exploring alternative methods to pattern MTJ multilayer stack with a focussed ion beam. Furthermore, I wish to acknowledge Daniel Ebke for arranging the possibility and Günter Reiss for giving the opportunity to use the c-AFM setup at the group Thin Films & Nanostructures Department of the University of Bielefeld. Also, I want to thank Felix Keseberg and Khalid Bhutta for helping me with the measurements.

Dichter bij huis wil ik Jos van Amelsvoort, Jos Bremmers en Nando Harmsen van het Cryogeen Bedrijf bedanken voor het leveren van de nodige liters Helium voor de SQUID. Ook wil ik de mensen van de faculteitswerkplaats bedanken voor het maken van verschillende onderdelen om opstellingen geschikt te maken voor het meten van mijn sub-μm MTJs. Tevens wil ik Fred van Nijmweegen, André Duif, Klaas Kopinga, Martine van Vlokhoven, Gerard Harkema, Jef Noijen, Evert Ridderhof en Bart Erich danken voor de mentale ondersteuning tijdens de wekelijkse donderdagmiddag bijeenkomsten.

In de groep Physics of Nanostructures heb ik vlak na de verhuizing van de optische laboratoria hulp gehad van Eric van Genuchten bij het opnieuw opbouwen van de MOKE opstelling. Verder heeft Ivo Erkens voor de optimalisatie van de artificiële antiferromagneet met de MOKE opstelling een dubbele wig onderzocht. Beide stagiaires wil ik danken voor hun werkzaamheden. Buiten mijn stagiaires hebben voormalige en huidige collega's en studenten van de groep Physics of Nanostructures mij op verschillende manieren geholpen en bijgedragen op aan een prettig werkklimaat. Met name de diverse Poker-Nights hebben geleid tot een leuke gezellige onderlinge band tussen studenten, promovendi en postdocs.

Een aantal personen van de groep Physics of Nanostructures wil ik in het bijzonder noemen. Ten eerste wil ik Karin Jansen bedanken voor de snelle afhandeling van mijn vele reisdeclaraties en het regelen van allerlei bureaucratische zaken. Tevens wil ik Jeroen Francke en Gerrie Baselmans bedanken voor de helpende hand bij problemen met opstellingen en het soepele verloop van experimenten.

Karel Knechten wil ik graag bedanken voor het uitvoeren van de *in situ* differentiële ellipsometrie metingen. Oleg Kurnosikov wil ik danken voor zijn hulp bij het aanpassen van de AFM, zodat de opstelling gebruikt kon worden voor elektrische metingen. Jürgen Kohlhepp ben ik dankbaar omdat hij mij geleerd heeft hoe ik de XPS-opstelling moet bedienen. Wim de Jonge wil ik dank zeggen voor zijn bereidheid om zitting te nemen in mijn promotiecommissie.

Naast mijn promotoren en copromotor wil ik ook de andere leden van mijn kerncommissie, Ronnie Jansen, Jo De Boeck en Richard van de Sanden, bedanken voor de opmerkingen en commentaren ten aanzien van mijn proefschrift.

Natuurlijk wil ik ook familie en vrienden bedanken voor de steun en ontspannende momenten die we samen beleefd hebben. In het bijzonder wil ik Marieke Schenkels danken voor het opvangen van mijn hond Lara, wanneer ik weer eens op een conferentie, NanoNed meeting of anderszins voor mijn werk weg moest. Mijn ouders ben ik dankbaar voor hun onvoorwaardelijke steun en geloof in mijn kunnen.

Als laatste wil ik Sandra van de Ven, mijn LieveLief bedanken voor het doorworstelen van al mijn artikelen en het gehele proefschrift, ook al was het Chinees voor je. Na het herschrijven, was het abstract over de Al_2O_3 barrières meer dan boeiend om te lezen, maar had het niet veel meer met fysica te maken. Echter, na het recht strijken van de fysische onvolkomenheden is het artikel uiteindelijk gepubliceerd in Applied Physics Letters. Sandra, tijdens mijn promotie heb je met raad en daad, maar ook dag en nacht voor me klaar gestaan. Ik ben trots dat ik jou mijn vriendin mag noemen!

Curriculum Vitae

Corine Geertruida Christina Hermienne Maria Fabrie

23 March 1970	Born in Eindhoven, The Netherlands
1982 - 1989	Pre-University Education Dr. Knippenbergcollege, Helmond The Netherlands
1996 - 2003	Applied Physics Eindhoven University of Technology The Netherlands External traineeship at Philips Research in the group Polymers & Organic Chemistry of dr. H. Hofstraat: *Build-in Potential of Polymer Light Emitting Diodes.* Masters thesis in the group Physics of Nanostructures of prof.dr.ir W. J. M. de Jonge and prof.dr. B. Koopmans: *Spin Injection and Dynamics in Hybrid Ferromagnet-Semiconductor Quantum Well Structures*
2003 - 2007	PhD candidate in the group Physics of Nanostructures of prof.dr.ir W. J. M. de Jonge and prof.dr. B. Koopmans Department of Applied Physics Eindhoven University of Technology The Netherlands *Towards Nanoscale Magnetic Memory Elements*